

0-315-09172-X



National Library of Canada

Bibliothèque nationale du Canada

CANADIAN THESES ON MICROFICHE

THÈSES CANADIENNES SUR MICROFICHE

115

57089

NAME OF AUTHOR/NOM DE L'AUTEUR Carl William Turner

TITLE OF THESIS/TITRE DE LA THÈSE "The Magnetic Properties of the Rare Earth Titanium Oxides RTiO₃; R=Tb,Dy,Ho,Er, Tm, Yb and Lu"

UNIVERSITY/UNIVERSITÉ McMaster

DEGREE FOR WHICH THESIS WAS PRESENTED/ GRADE POUR LEQUEL CETTE THÈSE FUT PRÉSENTÉE Ph.D.

YEAR THIS DEGREE CONFERRED/ANNÉE D'OBTENTION DE CE DEGRÉ 1982

NAME OF SUPERVISOR/NOM DU DIRECTEUR DE THÈSE Dr. J.E. Greedan

Permission is hereby granted to the NATIONAL LIBRARY OF CANADA to microfilm this thesis and to lend or sell copies of the film.

L'autorisation est, par la présente, accordée à la BIBLIOTHÈQUE NATIONALE DU CANADA de microfilmer cette thèse et de prêter ou de vendre des exemplaires du film.

The author reserves other publication rights, and neither the thesis nor extensive extracts from it may be printed or otherwise reproduced without the author's written permission.

L'auteur se réserve les autres droits de publication; ni la thèse ni de longs extraits de celle-ci ne doivent être imprimés ou autrement reproduits sans l'autorisation écrite de l'auteur.

DATED/DATE June 29, 1982 SIGNED/SIGNÉ Carl W. Turner

PERMANENT ADDRESS/RÉSIDENCE FIXÉE

THE MAGNETIC PROPERTIES
OF THE
RARE EARTH TITANIUM OXIDES
 $RTiO_3$; R = Tb, Dy, Ho, Er, Tm, Yb, Lu

By



CARL WILLIAM TURNER, B.Sc.

A Thesis

Submitted to the School of Graduate Studies
in Partial Fulfilment of the Requirements
for the Degree
Doctor of Philosophy

McMaster University

March 1982

THE MAGNETIC PROPERTIES OF RTiO_3

DOCTOR OF PHILOSOPHY (1982)
(Chemical Physics)

McMASTER UNIVERSITY
Hamilton, Ontario

TITLE: The Magnetic Properties of the Rare Earth Titanium
Oxides $RTiO_3$; R = Tb, Dy, Ho, Er, Tm, Yb and Lu

AUTHOR: Carl William Turner, B.Sc. (McMaster University)

SUPERVISORS: Professor J.E. Greedan and Professor M.F. Collins

NUMBER OF PAGES: xii, 198

ABSTRACT

The magnetic properties of the heavy rare earth titanium oxides RTiO_3 , $R = \text{Tb, Dy, Ho, Er, Tm, Yb}$ and Lu , have been investigated. The RTiO_3 develop a spontaneous magnetization below critical temperatures ranging from 28 K to 64 K. Both the rare earth and titanium moments order at the same temperature. The field dependence of the magnetization at 4.2 K indicates that the magnetocrystalline anisotropy is very large. The paramagnetic susceptibility of the materials formed with $R = \text{Tb-Tm}$ is analyzed with molecular field theory to obtain the molecular field coupling constants $\lambda_{\text{Ti-Ti}}$, $\lambda_{\text{R-Ti}}$ and $\lambda_{\text{R-R}}$.

The magnetic structures are determined for RTiO_3 , $R = \text{Tb-Tm}$ with the technique of neutron diffraction. The erbium and thulium moments form a ferromagnetic array along the orthorhombic c axis and the terbium, dysprosium and holmium moments have both ferromagnetic and antiferromagnetic components in the ab plane, giving rise to a canted structure. The titanium moments are in a ferromagnetic array which is directed antiparallel to the ferromagnetic component of the rare earth moment. The preferred direction of the rare earth magnetization with respect to the orthorhombic c axis is discussed in terms of the interaction between the $4f$ electrons on the rare earth and the crystalline environment. Calculations are presented which support this hypothesis.

ACKNOWLEDGEMENTS

I would like to thank my supervisors, Dr. J.E. Greedan and Dr. M.F. Collins, for their guidance and encouragement throughout the course of this work. I appreciate the helpful discussions with my supervisory committee, Dr. J.E. Greedan, Dr. M.F. Collins and Dr. J.A. Morrison.

The technical assistance provided by Mr. J. Garrett, Mr. H.F. Gibbs, Mr. A. Quaglia, Mr. J. Couper and Mr. G. Hewitson is gratefully acknowledged. I would also like to thank Dr. D.A. Goodings and Dr. C.V. Stager for many helpful discussions and for the interest that they showed towards the research project.

Finally, I would like to thank my wife, Rhonda, for her patience and encouragement throughout the entire course of this project.

TABLE OF CONTENTS

<u>CHAPTER</u>		<u>PAGE</u>
1	INTRODUCTION	1
	1.1 Why study the magnetic properties of RTiO_3 ?	1
	1.2 Origin of the magnetization in RTiO_3	4
	1.3 Coupling of the magnetic moments	13
	1.4 Consequences of the ferromagnetic titanium exchange	22
	1.5 Molecular field theory	24
	1.6 Spin configurations of ionic structures	33
	1.7 An overview of neutron scattering	42
	1.8 The crystal field	51
2	SAMPLE PREPARATION AND CHARACTERIZATION	57
	2.1 Sample preparation	57
	2.2 Sample analysis	60
3	EXPERIMENTAL PROCEDURES	67
	3.1 Introduction	67
	3.2 Bulk magnetic measurements	67
	3.3 Neutron diffraction measurements	69
	3.4 Alignment of the single crystals	70
4	EXPERIMENTAL RESULTS AND DISCUSSION	73
	4.1 Bulk magnetic data	73
	4.2 Magnetic structures	89

<u>CHAPTER</u>		<u>PAGE</u>
	4.3 Magnetic structures - calculations	122
	4.4 Temperature dependence of the magnetization	137
	4.5. Bulk magnetic data - single crystals	145
5	CONCLUSIONS	159
REFERENCES		163
APPENDIX A	NUCLEAR SCATTERING DATA AND SCATTERING INTENSITIES	169
APPENDIX B	MAGNETIC SCATTERING DATA AND SCATTERING INTENSITIES	178
APPENDIX C	REDUCED MAGNETIZATION - REDUCED TEMPERATURE DATA	188
APPENDIX D	MAGNETIZATION - TEMPERATURE DATA	193
	SUSCEPTIBILITY - TEMPERATURE DATA	

LIST OF FIGURES

<u>FIGURE NO.</u>		<u>PAGE</u>
1-1	The cubic perovskite and the O-orthorhombic perovskite structure	2
1-2	Superexchange in the $M^{++}O^2-M^{++}$ system	21
1-3	Temperature dependence of the reduced magnetization for ferromagnets with $S = 1/2, 7/2$ and ∞	30
1-4	Rare earth and titanium positions in the orthorhombic unit cell	35
1-5	Transformation properties of axial vectors	39
2-1	Unit cell volumes for $RTiO_3$, $R = Tb-Lu$	64
3-1	Single crystal of $ErTiO_3$	72
4-1	Magnetization cubed versus temperature for $RTiO_3$, $R = Tb-Lu$	74
4-2	Critical temperature, de Gennes factor and magnetic moment for $RTiO_3$, $R = Tb-Lu$	75
4-3	Temperature dependence of the inverse susceptibility for $RTiO_3$, $R = Gd-Tm$	78
4-4	Field dependence of the isothermal (4.2K) magnetization for $RTiO_3$, $R = Tb-Tm$ and fields ranging from 0 + 15 kilogauss	85
4-5	Field dependence of the isothermal (4.2K) magnetization for $RTiO_3$, $R = Dy, Ho$ and Er and fields ranging from 0 + 60 kilogauss	86
4-6	Angular dependence of the neutron scattering intensity for $TbTiO_3$ at 100K	95
4-7	Angular dependence of the neutron scattering intensity for $TbTiO_3$ at 10K	98
4-8	Terbium and titanium moment directions in the magnetic unit cell	104

<u>FIGURE NO.</u>		<u>PAGE</u>
4-9	Angular dependence of the neutron scattering intensity for TmTiO_3 at 10 K	107
4-10	Transformation properties of the principle axes of a second rank tensor in the point group D_{2h}	118
4-11	Transformation properties of the principle axes of a second rank tensor in the space group Pbnm	120
4-12	Reduced magnetization versus reduced temperature for ErTiO_3	140
4-13	Reduced magnetization versus reduced temperature for TbTiO_3	141
4-14	Temperature dependence of the sublattice magnetization in $\text{Gd}_3\text{Fe}_5\text{O}_{12}$	144
4-15	Anisotropy of the magnetization in the ab and bc planes of HoTiO_3	146
4-16	Field dependence of the isothermal (4.2 K) magnetization of HoTiO_3 along the crystallographic axes and fields ranging from 0 + 15 kilogauss	147
4-17	Field dependence of the isothermal magnetization of HoTiO_3 at selected temperatures below T_c	149
4-18	Anisotropy of the magnetization in the bc plane of ErTiO_3	151
4-19	Field dependence of the isothermal magnetization of ErTiO_3 at selected temperatures below T_c	152
4-20	Temperature dependence of the inverse susceptibility of HoTiO_3 along the crystallographic axes	155
4-21	Temperature dependence of the inverse susceptibility of ErTiO_3 along the b and c axes	156

<u>FIGURE NO.</u>		<u>PAGE</u>
A-1	Angular dependence of the neutron scattering intensity for DyTiO ₃ at 100 K	169
A-2	Angular dependence of the neutron scattering intensity for HoTiO ₃ at 298 K	171
A-3	Angular dependence of the neutron scattering intensity for ErTiO ₃ at 298 K	173
A-4	Angular dependence of the neutron scattering intensity for TmTiO ₃ at 100 K	175
A-5	Angular dependence of the neutron scattering intensity for YbTiO ₃ at 100 K	177
B-1	Angular dependence of the neutron scattering intensity for DyTiO ₃ at 10 K	178
B-2	Angular dependence of the neutron scattering intensity for HoTiO ₃ at 4.2 K	181
B-3	Angular dependence of the neutron scattering intensity for ErTiO ₃ at 4.2 K	184
B-4	Angular dependence of the neutron scattering intensity for YbTiO ₃ at 10 K	187
C-1	Reduced magnetization versus reduced temperature for TmTiO ₃	188
C-2	Reduced magnetization versus reduced temperature for DyTiO ₃	189
C-3	Reduced magnetization versus reduced temperature for HoTiO ₃	191

LIST OF TABLES

<u>TABLE NO.</u>		<u>PAGE</u>
1-1	Character table for the point group D_{2h} and space group Pbnm ($k = 0$)	38
1-2	Transformation properties in the space group Pbnm	41
2-1	Observed and calculated d-spacings for $DyTiO_3$ determined by powder X-ray diffraction (CuK_{α} radiation)	62
2-2	Unit cell parameters for $RTiO_3$, $R = Tb-Lu$	63
2-3	Results of thermogravimetric and neutron activation analyses	66
4-1	Curve fitting parameters derived from the high temperature susceptibilities of $RTiO_3$, $R = Gd-Tm$	82
4-2	Critical temperatures determined from the temperature dependence of the spontaneous magnetization (T_c) and the paramagnetic susceptibility (T_p)	84
4-3	Positional parameters for $RTiO_3$, $R = Tb-Yb$	92
4-4	Comparison of observed and calculated nuclear scattering intensities for $TbTiO_3$. $R^2 = 5.9\%$	94
4-5	Comparison of observed and calculated magnetic scattering intensities for $TbTiO_3$. $R^2 = 5.2\%$	101
4-6	Results of the magnetic structure refinements for $RTiO_3$. $R = Tb-Tm$	105
4-7	Comparison of observed and calculated magnetic intensities for $TmTiO_3$. $R^2 = 4.2\%$	108
4-8	Comparison of the rare earth magnetic moments (in Bohr magnetons) found in RMO_3 , $M = Cr, Fe, Al$ and Ti with their free ion values	113

<u>TABLE NO.</u>		<u>PAGE</u>
4-9	Rare earth moment directions in RMO_3 , $\text{M} = \text{Cr, Fe, Al and Ti}$	115
4-10	Compatibility tables for the groups O_h , D_{4h} , D_{2h} and C_s	126
4-11	Energies and permanent magnetic moments of the ground states of R^{3+} in RTiO_3 for R^{3+} in C_s symmetry	131
4-12	Coefficients of the wavefunctions for the ground state of R^{3+} in RTiO_3	133 C
4-13	Energies and permanent magnetic moment of the ground states of R^{3+} in RTiO_3 for R^{3+} in D_{4h} symmetry	135
4-14	Critical temperatures for RTiO_3 , $\text{R} = \text{Tb-Tm}$, from spontaneous magnetization (a) and neutron diffraction (b)	138
A-1	Comparison of observed and calculated nuclear intensities for DyTiO_3 . $\text{R}'' = 7.9\%$	170
A-2	Comparison of observed and calculated nuclear intensities for HoTiO_3 . $\text{R}'' = 8.1\%$	172
A-3	Comparison of observed and calculated nuclear intensities for ErTiO_3 . $\text{R}'' = 5.3\%$	174
A-4	Comparison of observed and calculated nuclear intensities for TmTiO_3 . $\text{R}'' = 4.9\%$	176
B-1	Comparison of observed and calculated magnetic intensities for DyTiO_3 . $\text{R}'' = 7.7\%$	179
B-2	Comparison of observed and calculated magnetic intensities for HoTiO_3 . $\text{R}'' = 4.3\%$	182
B-3	Comparison of observed and calculated magnetic intensities for ErTiO_3 . $\text{R}'' = 4.1\%$	185

<u>TABLE NO.</u>		<u>PAGE</u>
D-1	Magnetization-temperature data for RTiO_3 R = Tb-Lu.	193
D-2	Inverse susceptibility (mole/cm^3)-temperature (K) data for RTiO_3 , R = Tb-Tm.	194
D-3	Inverse susceptibility-temperature data along the b and c axes of ErTiO_3	196
D-4	Inverse susceptibility-temperature data along the crystallographic axes of HoTiO_3	197

CHAPTER I
INTRODUCTION

1-1 WHY STUDY THE MAGNETIC PROPERTIES OF RTiO_3 ?

The magnetic properties of materials which crystallize in various modifications of the cubic perovskite structure have been studied extensively and are well documented in the literature (Goodenough and Longo, 1970). Materials which have the formula RMO_3 , where R is a trivalent rare earth ion and M is a trivalent transition metal ion or aluminum ion, generally crystallize in the O-orthorhombic distortion of cubic perovskite. The ideal perovskite structure consists of a simple cubic lattice of M^{3+} cations with R^{3+} cations at the body centre positions and an octahedron of oxygen anions centred on each M^{3+} . The O-orthorhombic distortion is formed by a cooperative buckling of the corner-shared octahedra of oxygens, such that $a < b$ and $c/a > \sqrt{2}$, where a, b and c are the lattice parameters of the orthorhombic unit cell. Both of these structures are shown in figure 1-1.

Although the magnetic properties of the compounds RMO_3 , $\text{M} = \text{Fe}, \text{Cr}, \text{Mn}, \text{V}$ and Al , have been thoroughly investigated (Goodenough and Longo, 1970), comparatively little interest has been shown towards the materials formed with $\text{M} = \text{Ti}$. Recent work has revealed that YTiO_3 is a ferromagnet with a critical tempera-

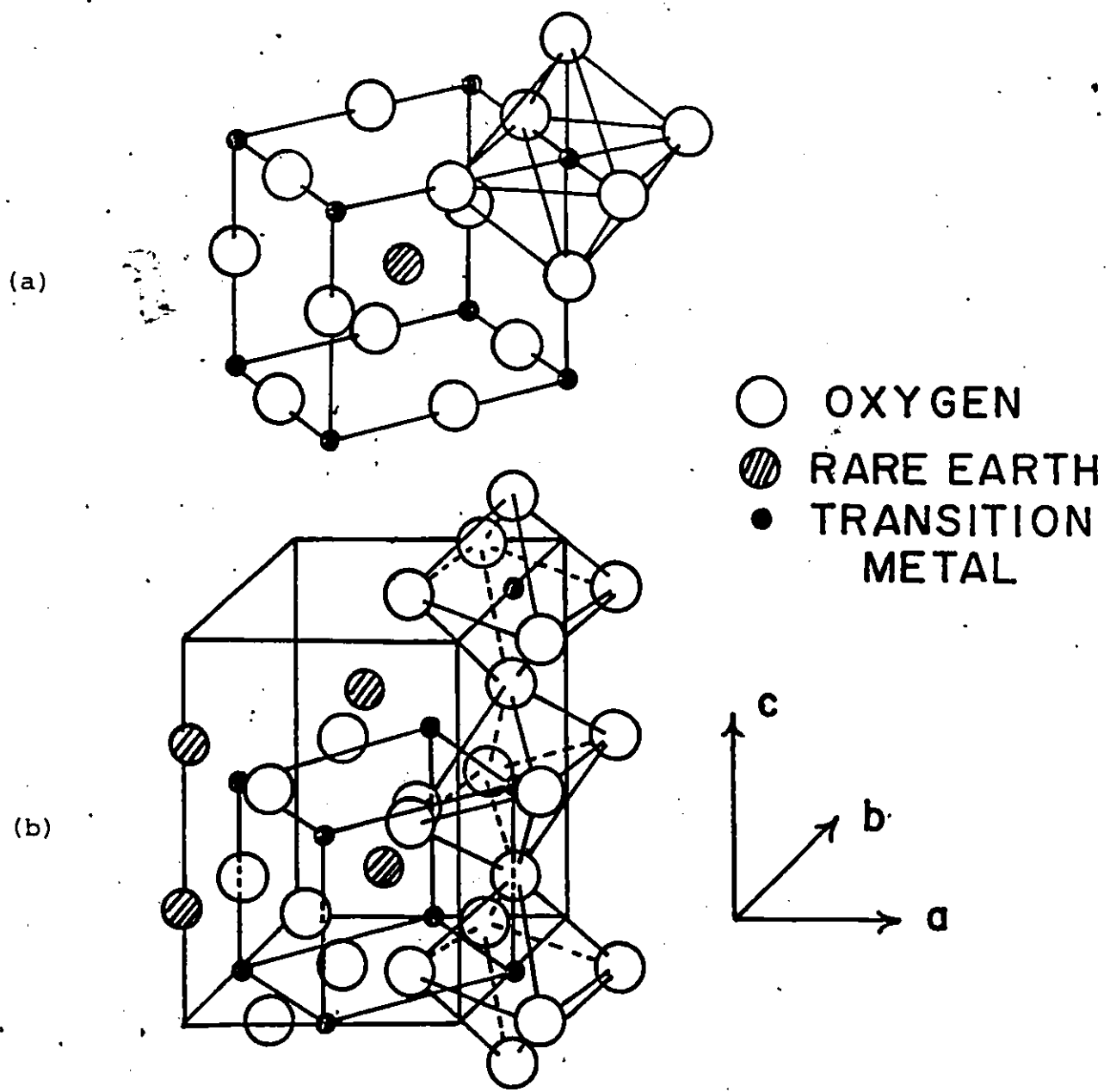


Fig. 1-1 (a) The ideal cubic perovskite structure
(b) The O-orthorhombic modification of the perovskite structure showing the pseudo-cubic unit cell.

ture of 29K, and that the ferromagnetism arises from a single d electron localized on the titanium site (Greedan and MacLean, 1978, MacLean, 1980, Johnson, 1975). In addition, GdTiO_3 has been reported to be a ferrimagnet in which magnetic moments on both the gadolinium and titanium sublattices couple at a temperature of 34K (Greedan and MacLean, 1978). This behaviour is truly remarkable since there seem to be no other structures in which the trivalent titanium ion has a local magnetic moment. The ferromagnetic coupling of the titanium magnetic moments is in marked contrast to the antiferromagnetic coupling of the transition metal moments reported in the isostructural materials RMO_3 , $M = \text{Fe, Cr, Mn and V}$. The existence of a magnetic moment on titanium along with ferromagnetic coupling of the titanium moments reported for the above heavy rare earth titanium oxides make this a unique and exciting series of compounds whose magnetic properties are well worth investigating.

Much of the theory that is pertinent to this investigation will be discussed in the following sections of the introduction. The preparation and characterization of the materials will be discussed in chapter 2. A description of the equipment used to collect the magnetic data, along with the techniques used to align the single crystals, is presented in chapter 3. Chapter 4 includes the presentation and interpretation of the magnetic data. Bulk magnetic data collected for polycrystalline samples are discussed in section 1 of chapter 4. These include critical temperatures and molecular field

coupling constants. In section 2, the magnetic structures are described and compared with the isostructural RMO_3 , $\text{M} = \text{Fe}, \text{Cr}$ and Al . The direction of the magnetization of the rare earth sublattice can be explained by the interaction between the rare earth ion and the crystal field. Calculations which support this are discussed in section 3. The temperature dependence of the magnetization of RTiO_3 is presented in section 4 and comparisons are made with the rare earth iron garnets. In section 5, bulk magnetic data collected for samples in the form of single crystals are presented and compared with the polycrystalline data.

1-2 ORIGIN OF THE MAGNETIZATION IN RTiO_3

There are two magnetic moments per formula unit in the heavy rare earth titanium oxides RTiO_3 , $\text{R} = \text{Gd}, \text{Tb}, \text{Dy}, \text{Ho}, \text{Er}, \text{Tm}$ and Yb . One magnetic moment is localized on the titanium site (MacLean, 1980) and arises from the single 3d electron of Ti^{III} . The second, and larger, magnetic moment is produced by the unpaired 4f electrons on the trivalent rare earth ion. In YTiO_3 and LuTiO_3 , the only species with a magnetic moment is the titanium ion, since both Lu^{III} and Y^{III} have no unpaired electrons, hence they are diamagnetic. Magnetic moments which originate from unpaired electrons are called atomic magnetic moments. Atoms (or ions) can also have a nuclear magnetic moment whose magnitude is governed by the nuclear structure.

The nuclear magnetic moment is several orders of magnitude smaller than the atomic magnetic moment. As it has no bearing on the bulk magnetic properties, as far as this investigation is concerned, it will not be discussed any further.

The energy levels of atomic states are affected by the application of an external magnetic field. The effect is small enough to be treated by perturbation theory. The Hamiltonian for the system can be written as

$$H = H_0 + HH^{(1)} + H^2H^{(2)} + \dots, \quad (1-1)$$

where H_0 is the unperturbed part and the perturbation is developed as a power series in the magnetic field, H . The energy of the j th state can be written as a power series in H to give

$$E_j = E_j^{(0)} + HE_j^{(1)} + H^2E_j^{(2)} \quad (1-2)$$

It can be shown by perturbation theory that (Van Vleck, 1932)

$$E_j^{(1)} = \langle \psi_j | H^{(1)} | \psi_j \rangle$$

and

$$E_j^{(2)} = \sum_{k \neq j} \frac{|\langle \psi_k | H^{(1)} | \psi_j \rangle|^2}{E_j^0 - E_k^0} + \langle \psi_j | H^{(2)} | \psi_j \rangle. \quad (1-3)$$

ψ_j and ψ_k are eigenfunctions of H_0 with eigenvalues E_j^0 and E_k^0 respectively. In the presence of a magnetic field, the kinetic energy of the i^{th} electron is expressed as (Ashcroft and Mermin, 1976)

$$T_i = \frac{1}{2m_i} \left(\bar{P}_i + \frac{e\bar{A}_i}{c} \right)^2, \quad (1-4)$$

where the vector potential \bar{A}_i is defined as

$$\bar{A}_i = -\frac{1}{2} \bar{r}_i \times \bar{H}. \quad (1-5)$$

The total electronic kinetic energy becomes

$$\begin{aligned} T &= \sum_i \frac{1}{2m_i} \left(\bar{P}_i + \frac{e\bar{A}_i}{c} \right)^2 \\ &= \frac{1}{2m} \sum_i \left(P_i^2 + \frac{e\bar{P}_i \cdot \bar{r}_i \times \bar{H}}{c} + \frac{e^2 H^2}{4c^2} (x_i^2 + y_i^2) \right) \\ &= T_0 - \mu_B \bar{L} \cdot \bar{H} + \frac{e^2 H^2}{8mc^2} \sum_i (x_i^2 + y_i^2), \end{aligned} \quad (1-6)$$

where μ_B is the Bohr magneton, $\mu_B = \frac{e\hbar}{2mc}$, and $\hbar\bar{L} = \sum_i \bar{r}_i \times \bar{P}_i$ is the total orbital angular momentum. The interaction energy of the field with each electronic spin is given by

$$H_S = -2\mu_B \bar{S} \cdot \bar{H} \quad (\bar{S} = \sum_i s_i). \quad (1-7)$$

The combination of this term with the kinetic energy gives the field dependent terms of the Hamiltonian:

$$H_H = -\mu_B (\bar{L} + 2\bar{S}) \cdot \bar{H} + \frac{e^2 H^2}{8mc^2} \sum_i (x_i^2 + y_i^2). \quad (1-8)$$

Comparing this expression with the power series expansion of the Hamiltonian, we make the following identifications;

$$H^{(1)} = -\mu_B (\bar{L} + 2\bar{S}) \quad (1-9)$$

= $-\bar{\mu}$, where $\bar{\mu}$ is the magnetic moment operator,

and

$$H^{(2)} = \frac{e^2}{8mc^2} \sum_i (x_i^2 + y_i^2) \quad (1-10)$$

The magnetic moment in the direction of the field for the j th state with energy E_j is defined as (Morrish, 1965)

$$\begin{aligned} \mu_j &= - \left(\frac{\partial E_j}{\partial H} \right) \\ &= (- E_j^{(1)} - 2HE_j^{(2)}) \end{aligned} \quad (1-11)$$

Substitution for $E_j^{(1)}$ and $E_j^{(2)}$ leads to

$$\begin{aligned} \mu_j &= - \langle \psi_j | H^{(1)} | \psi_j \rangle - \left\{ \sum_{k \neq j} \frac{|\langle \psi_k | H^{(1)} | \psi_j \rangle|^2}{E_j^0 - E_k^0} \right. \\ &\quad \left. + \langle \psi_j | H^{(2)} | \psi_j \rangle \right\} \\ &= \mu_B \langle \psi_j | \bar{L} + 2\bar{S} | \psi_j \rangle - 2H\mu_B^2 \sum_{k \neq j} \frac{|\langle \psi_k | \bar{L} + 2\bar{S} | \psi_j \rangle|^2}{E_j^0 - E_k^0} \\ &= \frac{e^2 H}{4mc^2} \langle \psi_j | \sum_i (x_i^2 + y_i^2) | \psi_j \rangle \end{aligned} \quad (1-12)$$

The magnetic moment has contributions from a permanent moment plus an induced moment which vanishes in zero applied field.

The wavefunctions ψ_j are eigenstates of the unperturbed Hamiltonian H_0 . The major contributions to the unperturbed

Hamiltonian are

$$H_0 = T_0 + H_{e-n} + H_{e-e} + H_{s-o} + H_{CF} \quad (1-13)$$

where T_0 = kinetic energy of electrons in zero applied field

H_{e-n} = attraction between electrons and nucleus

H_{e-e} = electron-electron repulsion

H_{s-o} = spin orbit coupling

H_{CF} = crystal field interaction.

H_{e-n} , H_{e-e} and H_{CF} originate from the Coulomb interaction, while H_{s-o} is a relativistic effect. The relative magnitude of the terms comprising H_0 , as well as the symmetry of the local atomic environment (through H_{CF}) determines the form of the wavefunctions ψ_j and the atomic magnetic moment.

Experiments have shown that the magnetic moment of Ti^{III} in $YTiO_3$ is $0.84 \mu_B$ per formula unit - close to its spin-only value of $1 \mu_B$ (Garrett, Greedan and MacLean, 1981). Recall from section 1-1 that this is the only structure where a local magnetic moment has been observed on the titanium (III) ion. Although there is some uncertainty with respect to the origin of the moment, the experimental evidence is conclusive. Hence, the assumption will be made that Ti^{III} has a moment of similar magnitude in the other heavy rare earth titanium oxides. Attempts to calculate the moment in the ground state of Ti^{III} in $YTiO_3$ are currently in progress, (Goral, unpublished). The zero field Hamiltonian for the 4f electrons on the rare earth ion can

be written as

$$H_0 = T_0 + H_{e-n} + H_{e-e} + H_{s-o} + H_{CF}, \quad (1-14)$$

where the last four terms appear in descending order of magnitude. The effect of electron-electron repulsion is to group the many-electron 4f wavefunctions into terms of different energy. Each term is labelled by its total orbital and spin angular momentum, defined as $\bar{L} = \sum_i \bar{l}_i$ and $\bar{S} = \sum_i \bar{s}_i$ respectively. This is referred to as Russell-Saunders coupling. L and S are good quantum numbers and the many electron wavefunctions are written $|L M_L S M_S\rangle$ where $M_L = L, L-1, \dots, -L$ and $M_S = S, S-1, \dots, -S$. The term which maximizes S and L, without violating the Pauli exclusion principle, has the lowest energy. The spin-orbit coupling operator has the form (Levine, 1974)

$$H_{s-o} = \sum_i \xi_i(r_i) \bar{l}_i \cdot \bar{s}_i$$

where

$$\xi_i(r_i) = \frac{1}{2m} \frac{1}{c^2} \frac{1}{r_i} \frac{dV(r_i)}{dr_i}. \quad (1-15)$$

H_{s-o} commutes with the total angular momentum $\bar{J} = \bar{L} + \bar{S}$ but not with \bar{L} or \bar{S} separately. Therefore, H_{s-o} is diagonal in \bar{J} but not in \bar{L} or \bar{S} . If we assume Russell-Saunders coupling and ignore any off-diagonal elements in \bar{L} or \bar{S} , the Hamiltonian for spin orbit coupling can be expressed as (Silver, 1976)

$$\begin{aligned}
 H_{S-0} &= \lambda \bar{L} \cdot \bar{S} \\
 &= \frac{\lambda}{2} (J(J+1) - L(L+1) - S(S+1)) .
 \end{aligned}
 \tag{1-16}$$

For the heavy rare earths, the 4f shell is more than half-filled so $\lambda < 0$. Therefore the ground state has $J = L+S$ and is $(2J+1)$ -fold degenerate in the absence of H_{CF} . The states which are labelled by the quantum numbers S , L , J and M_J compose a multiplet. The expectation value of the magnetic moment operator $\bar{\mu}$ in the multiplet $|LSJM_J\rangle$ is equal to

$$\bar{\mu} = -\mu_B \langle LSJM_J | \bar{L} + 2\bar{S} | LSJM_J \rangle .$$

Using the Wigner-Eckart theorem (Silver, 1976), we can express this as

$$\bar{\mu} = -\mu_B g_J \langle LSJM_J | \bar{J} | LSJM_J \rangle , \tag{1-17}$$

where

$$g_J = 1 + \frac{J(J+1) + L(L+1) - S(S+1)}{2J(J+1)} . \tag{1-18}$$

This form of the magnetic moment operator ignores elements which are off-diagonal in J and assumes that the multiplets are well separated in energy. When the rare earth ion is placed in a crystalline environment, the interaction between the 4f electrons and the crystal field can remove some, or all, of the degeneracy of the free ion multiplets. A theorem due to Kramers states that the crystal field can lift all of the degeneracy of the electronic wavefunctions of an ion with an even num-

ber of electrons, but must leave an odd-electron system with at least two-fold degenerate wavefunctions (Kramers, 1930). The expectation value of $H^{(1)}$ to first order is zero for non-degenerate states and so, when the crystal field has removed all of the degeneracy of the electronic wavefunctions, the permanent magnetic moment is zero (see equation 1-12). If a field is applied, such as when the magnetic susceptibility is measured, the induced magnetic moment is finite due to the second and third terms in equation (1-12). In the crystalline environment, both J and M_J cease to be good quantum numbers. However, the crystal field splittings are generally small compared with the separation between the multiplets so that mixing of the wavefunctions from different multiplets can be ignored to a good approximation.

The magnetic susceptibility per unit volume is defined as (Ashcroft and Mermin, 1976)

$$\kappa = \frac{\partial M}{\partial H},$$

where

$$M(H, T) = \frac{1}{V} \frac{\sum_j \mu_j(H) \exp(-E_j/kT)}{\sum_j \exp(-E_j/kT)}. \quad (1-19)$$

The magnetic moment of the j th state is given by equation (1-12):

$$\mu_j = \mu_B \langle \psi_j | \bar{L} + 2\bar{S} | \psi_j \rangle - 2\mu_B^2 H \sum_{k \neq j} \frac{|\langle \psi_k | \bar{L} + 2\bar{S} | \psi_j \rangle|^2}{E_j^0 - E_k^0} \\ - \frac{e^2 H^2}{4mc^2} \langle \psi_j | \sum_i (\bar{x}_i^2 + \bar{y}_i^2) | \psi_j \rangle .$$

If an ion has no unpaired electrons then L and S are zero. Thus the only contribution to the susceptibility comes from $\frac{-e^2 H^2}{4mc^2} \langle \psi_j | \sum_i (\bar{x}_i^2 + \bar{y}_i^2) | \psi_j \rangle$. The result is a small negative susceptibility which is temperature independent and is referred to as diamagnetism. If the ion has unpaired electrons, then L and/or S are non-zero and the first two terms in equation (1-12) make contributions to the susceptibility which are larger than the diamagnetic term. The expression for the susceptibility of an ion in a crystal field, ignoring the diamagnetic contribution, is shown in section 4-5. Its derivation is outlined in Mabbs and Machin (1973) and involves a statistical mechanical average over the available crystal field levels in which are kept only those terms that are independent of the applied field. The susceptibility is positive with both temperature-dependent and temperature-independent terms and is called paramagnetism.

So far, there has been no mention of any interactions between magnetic moments on different sites in the lattice and the Hamiltonian has been written for a single ion. When such interactions occur, there is a critical temperature, T_c , below which cooperative ordering of the moments is observed. This

spontaneous magnetization produces a susceptibility which normally can be several orders of magnitude larger than that observed for paramagnets. If the moments couple parallel to one another, the phenomenon is called ferromagnetism while, if they order antiparallel, it is called antiferromagnetism. When there are two different magnetic species present in the material, there is a third possibility known as ferrimagnetism. Here, moments of different magnitude are aligned antiparallel such that there is a net magnetic moment. Other more complicated arrays of magnetic moments are known, such as spiral, helical, conical or triangular. It is not the intent here to present an exhaustive discussion of these various phenomena, but merely to indicate that they all result from a spontaneous coupling of the magnetic moments at a finite temperature.

1-3 COUPLING OF THE MAGNETIC MOMENTS

Phenomenological Theory

In order for a material to develop a spontaneous magnetization at a finite temperature, some mechanism must exist for coupling the magnetic moments. Current theories ascribe this to a correlation of the spins on the neighbouring sites due to a combination of the Coulomb interaction and the Pauli exclusion principle. Group theory can be used to determine the ways in which the spins combine.

The spin associated with a magnetic ion can be repre-

represented by three orthogonal components S_x , S_y and S_z . These three components form a basis for the $D^{(\ell=1)}$ irreducible representation of the full rotational group (Silver, 1976). This means that suitable linear combinations of the components S_x , S_y and S_z will transform as the spherical harmonics $Y_\ell^m(\theta, \phi)$ for $\ell = 1$. The coupled spins from two different magnetic ions form a basis for the representation $D^{(1)} \otimes D^{(1)}$. This representation can be decomposed with standard techniques of group theory, to the irreducible representations $D^{(2)} + D^{(1)} + D^{(0)}$. It follows that linear combinations of the products $S_{1\alpha} S_{2\beta}$, where 1 and 2 refer to different spins and α, β refer to the components x, y and z, must transform as the spherical harmonics $Y_\ell^m(\theta, \phi)$, for $\ell = 2, 1$ and 0.

The spherical harmonic Y_0^0 is a scalar, so that its basis function must be formed from the scalar product $\bar{S}_1 \cdot \bar{S}_2$. This is identified as the Heisenberg term and is isotropic and symmetric. The energy of the coupled spins is expressed as

$$H = -J_{12} \bar{S}_1 \cdot \bar{S}_2, \quad (1-20)$$

where J_{12} is a scalar. The Heisenberg term couples the spins parallel or antiparallel, depending on whether J_{12} is positive or negative. The cross product of two spins is a vector whose components transform as the spherical harmonics $Y_1^{\pm 1}$ and Y_1^0 . This coupling is referred to as the Dzyaloshinsky-Moriya interaction (Dzyaloshinsky, 1958; Moriya, 1960, 1963) and is both

anisotropic and antisymmetric. Its contribution to the energy of the coupled spins is written as

$$H = \bar{D}_{12} \cdot \bar{S}_1 \times \bar{S}_2 \quad (1-21)$$

where \bar{D}_{12} is an axial vector. The dipolar coupling between two spins can be written in a way which transforms as the spherical harmonics Y_ℓ^m for $\ell = 2$. This interaction is symmetric and anisotropic and usually appears in the form

$$H = \bar{S}_1 \cdot \bar{T}_{12} \cdot \bar{S}_2 \quad (1-22)$$

Group theory has been used to show that there are three ways to couple the two spins originating from different magnetic ions. These can be identified as an isotropic symmetric, anisotropic symmetric and anisotropic antisymmetric coupling. However, group theory does not give any insight into the origin or magnitude of these terms.

Origin of the Coupling of Spins

One way of coupling two spins is by a direct magnetic dipole-dipole interaction. However, this mechanism underestimates the critical temperature of some well known ferromagnets by several orders of magnitude. With the advent of quantum mechanics, Heisenberg was able to show that the coupling between two spins originates from the exchange interaction, which is simply the Coulomb interaction combined with the Pauli exclusion principle (Heisenberg, 1926). The following derivation

can be found in many textbooks on quantum mechanics (Levine, 1974).

Consider two electrons moving in the potential field of two nuclei. The Hamiltonian for this system has the form

$$(H_0 + H')\psi = E\psi$$

where

$$H_0 = -\frac{1}{2m} (\nabla_1^2 + \nabla_2^2) - \frac{e^2}{r_{1a}} - \frac{e^2}{r_{2b}},$$

$$H' = \frac{e^2}{r_{ab}} - \frac{e^2}{r_{1b}} - \frac{e^2}{r_{2a}} + \frac{e^2}{r_{12}}. \quad (1-23)$$

The subscripts a and b refer to the nuclei, and subscripts 1 and 2 refer to the electrons. In the absence of H' , the energies of electrons 1 and 2 are identical. Since the electrons are indistinguishable, the spatial part of their wavefunctions can be written as

$$\psi_{\text{symmetric}} = (\psi_a(1)\psi_b(2) + \psi_a(2)\psi_b(1)),$$

and

$$\psi_{\text{antisymmetric}} = (\psi_a(1)\psi_b(2) - \psi_a(2)\psi_b(1)). \quad (1-24)$$

H' lifts the degeneracy of this system so that

$$E_{\text{symmetric}} = 2E_0 + \frac{K+J}{1+S_0^2},$$

and

$$E_{\text{antisymmetric}} = 2E_0 + \frac{K-J}{1-S_0^2}. \quad (1-25)$$

$2E_0$ is the energy of the system in the absence of H' ,

$$K = \iint \psi_a^*(1) \psi_b^*(2) H' \psi_a(1) \psi_b(2) d\tau_1 d\tau_2 ,$$

$$J = \iint \psi_a^*(1) \psi_b^*(2) H' \psi_a(2) \psi_b(1) d\tau_1 d\tau_2 ,$$

and

$$S_0 = \int \psi_a^*(1) \psi_b(1) d\tau_1 = \int \psi_a^*(2) \psi_b(2) d\tau_2 . \quad (1-26)$$

K , J and S_0 are referred to as the Coulomb, exchange and overlap integrals respectively. The Pauli exclusion principle demands that the wavefunction for any system of electrons be antisymmetric. Since the wavefunctions for a system of two electrons can always be written as the product of functions of the spatial and spin coordinates, $\psi_{\text{symmetric}}$ and $\psi_{\text{antisymmetric}}$ must be combined with antisymmetric ($S=0$; singlet) and symmetric ($S=1$; triplet) spin functions respectively. Thus

$${}^1\Psi = \psi_{\text{symmetric}}(\alpha(1)\beta(2) - \beta(1)\alpha(2)) ,$$

and

$${}^3\Psi = \psi_{\text{antisymmetric}} \begin{pmatrix} \alpha(1)\alpha(2) \\ \alpha(1)\beta(2) + \alpha(2)\beta(1) \\ \beta(1)\beta(2) \end{pmatrix} , \quad (1-27)$$

where α and β refer to the two spin states of a single electron. If the energy $2E_0$ and the overlap integral S_0 are ignored, the energies of the singlet and triplet states can be expressed as

$$E_{\text{singlet}} = K + J \quad (S = 0) ,$$

and

$$E_{\text{triplet}} = K - J \quad (S = 1) . \quad (1-28)$$

The energies of the singlet and triplet states differ by an amount which is determined by the exchange integral, J . Although J originates from the Coulomb interaction -

$$H' = \frac{e^2}{r_{ab}} - \frac{e^2}{r_{2a}} - \frac{e^2}{r_{1b}} + \frac{e^2}{r_{12}} ,$$

this can be interpreted as an effective coupling of the electron spins. For $\bar{S} = \bar{S}_1 + \bar{S}_2$,

$$S^2 = S_1^2 + S_2^2 + 2\bar{S}_1 \cdot \bar{S}_2 .$$

For the singlet state, $S = 0$ and $\bar{S}_1 \cdot \bar{S}_2 = -3/4$.

The triplet state has $S = 1$, so $\bar{S}_1 \cdot \bar{S}_2 = 1/4$.

If the interaction between the two spins is written

$$H' = K - \frac{1}{2} J - 2J \bar{S}_1 \cdot \bar{S}_2 , \quad (\text{Van Vleck, 1932}) \quad (1-29)$$

the energy of the system is $E = K+J$ when $\bar{S}_1 \cdot \bar{S}_2 = -3/4$ ($S=0$) and $E = K-J$ when $\bar{S}_1 \cdot \bar{S}_2 = 1/4$ ($S=1$). If we ignore the terms that are independent of the spins,

$$H' = -2J_{12} \bar{S}_1 \cdot \bar{S}_2 , \quad (1-30)$$

which is the Heisenberg spin Hamiltonian. When $J_{12} > 0$, the triplet state ($\uparrow\uparrow$) is the ground state and when $J_{12} < 0$, the

singlet state ($\uparrow\downarrow$) is lowest in energy.

The exchange integral J is given by

$$\begin{aligned}
 J &= \iint \psi_a^*(1) \psi_b^*(2) H' \psi_a(2) \psi_b(1) d\tau_1 d\tau_2 \\
 &= \frac{e^2}{r_{ab}} \overbrace{S_0^2} - 2S_0 \int \psi_a^*(1) \frac{e^2}{r_{b1}} \psi_b(1) d\tau_1 \\
 &+ \iint \psi_a^*(1) \psi_b^*(2) \frac{e^2}{r_{12}} \psi_b(1) \psi_b(2) d\tau_1 d\tau_2 . \quad (1-30)
 \end{aligned}$$

If the electrons are in orthogonal orbitals, the terms in S_0 are zero, so $J > 0$. In this case, the triplet ($S=1$) state is the ground state. This is the physical origin of Hund's rule which says that the state which maximizes the spin of an atom will be the ground state. When the orbitals are not orthogonal, the sign of J depends on the relative size of the various terms in the above expression.

The interaction between spins on adjacent sites is called direct exchange. Often, the magnetic ions are separated by a diamagnetic anion or ligand such that a direct interaction is not possible. Exchange which is mediated in some way by an intervening diamagnetic species is referred to as superexchange. The first theory of superexchange, introduced by Kramers (1934) involved electron transfer from filled orbitals on the anion to partially filled orbitals on the adjacent cations, hence creating an excited ionic state. This is illustrated in figure 1-2 for the anion O^{2-} and the cation M^{++} . An

electron is transferred from the p_z orbital of O^{2-} to the d_z^2 orbital on M^{++} , thus forming the species $M^+O^-M^{++}$ in an excited state. The remaining p_z electron on O^{2-} can exchange couple with the d_z^2 electron on the adjacent M^{++} . Since the p_z and d_z^2 orbitals are not orthogonal, the sign of J depends on the relative strengths of the various terms which go into the expression for J . In figure 1-2, case c) corresponds to $J > 0$ and d) corresponds to $J < 0$. The wavefunction which describes the system is a mixture of the ground state before electron transfer plus the excited ionic state. Configuration mixing will stabilize either the singlet or triplet ground state, depending on the sign of J . This picture of superexchange has subsequently been modified to treat superexchange as the result of direct overlap of cation d orbitals which have been expanded by interaction with the intervening anion. In this sense, there is no fundamental difference between direct exchange and superexchange (Anderson, 1963).

It is very difficult to predict the sign of the exchange interaction as there are many one-electron transfers which must be considered. Goodenough (1955, 1958) and Kanamori (1959) have had some success at predicting the sign of J for 180° and 90° exchange for d electrons in cubic symmetry. The Ti-O-Ti bond angles in $RTiO_3$ are intermediate between these two limiting cases (MacLean, Ng and Greedan, 1979), and so any predictions of the sign of J would be dubious. The

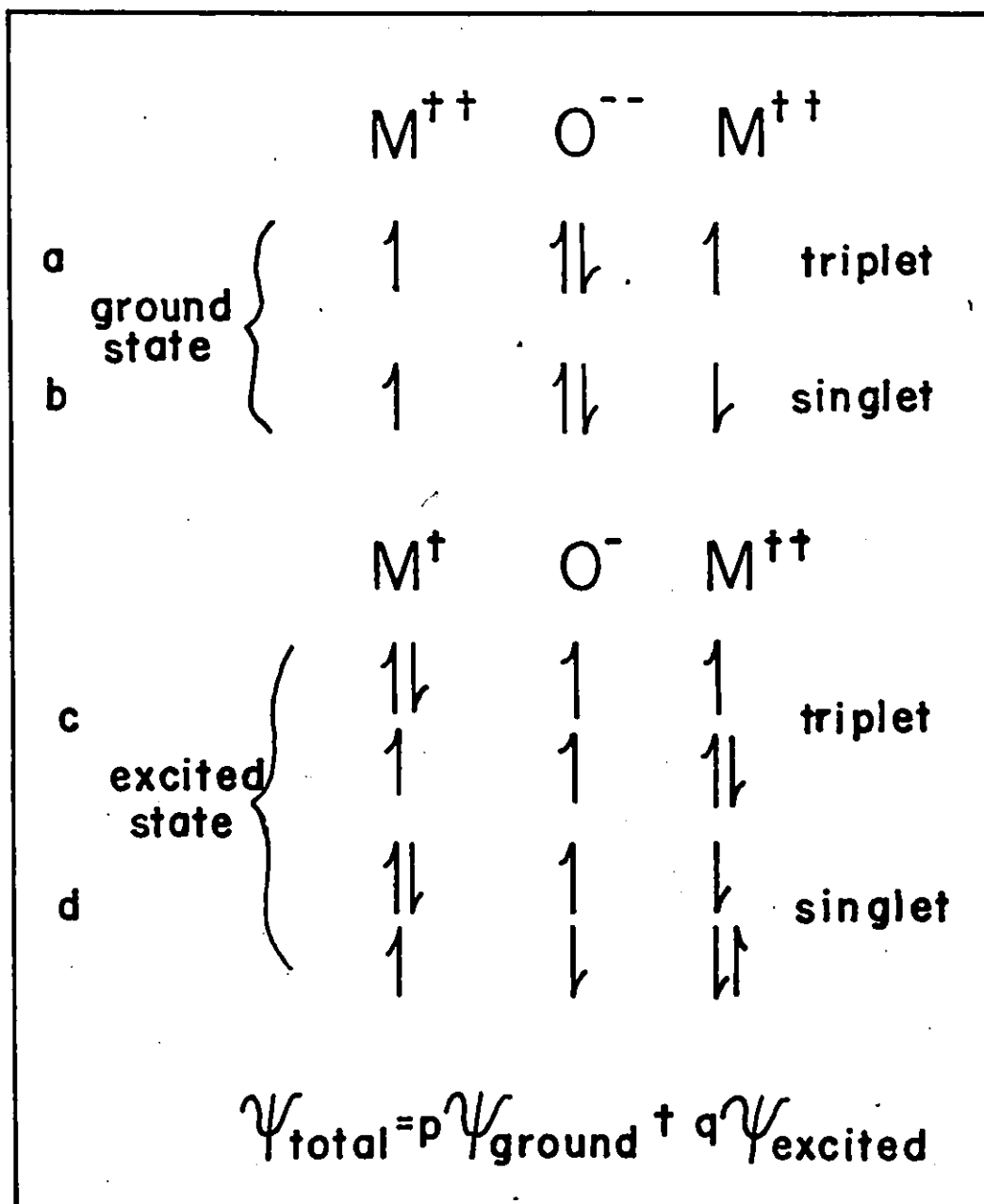


Fig. 1-2 Superexchange in the $M^{++}O^{--}M^{++}$ system.

closest Ti-Ti contact in RTiO_3 is about 4 \AA , with the result that direct exchange is not likely to be important. The rare earth 4f wavefunctions are too localized to participate in direct exchange, although R-Ti superexchange can occur by the transfer of an electron to the unoccupied 5d orbitals of the rare earth ion.

The exchange Hamiltonian derived by Heisenberg describes only one way that spins on neighbouring sites can couple. The phenomenological theory predicted vector and dipolar couplings as well. By taking account of spin-orbit coupling in the mechanism of superexchange, Moriya obtained terms of the form $\bar{D}_{12} \cdot \bar{S}_1 \times \bar{S}_2$ and $\bar{S}_1 \cdot \bar{T}_{12} \times \bar{S}_2$ (Moriya, 1960, 1963). As the latter term does not originate from dipole-dipole coupling, it is referred to as pseudodipolar coupling. Moriya's calculation treated λ/Δ as a perturbation, where λ is the spin orbit coupling and Δ represents the crystal field, and so it is most applicable for the discussion of exchange involving 3d electrons. White and White (1968) considered exchange coupling between single f and d electrons. They also found terms in the exchange splitting which correspond to anisotropic symmetric and antisymmetric coupling.

1.4 THE CONSEQUENCES OF FERROMAGNETIC TITANIUM EXCHANGE

A survey of the magnetic properties of the materials RMO_3 , $M = \text{Fe, Cr and Al}$, reveals the following two features:

- a) antiferromagnetic ordering of the transition metal moments at temperatures of order 100K.
- b) antiferromagnetic ordering of the rare earth moments at temperatures close to 4K.

In the orthoaluminates, where the only magnetic species is the rare earth ion, magnetic ordering occurs only for DyAlO_3 and TbAlO_3 at approximately 4K. This indicates that R-R exchange in these systems is very small. Figure 1-1 shows that the rare earth ion can couple with eight nearest neighbour transition metal ions which are all crystallographically equivalent. When the transition metal moments are coupled antiferromagnetically, the isotropic R-M coupling vanishes by symmetry and the rare earth and transition metal moments order at different temperatures. The fact that the critical temperatures for ordering of the rare earth moments in RFeO_3 and RCrO_3 are increased only marginally from their values in RAlO_3 indicates that the magnitude of the R-M anisotropic coupling is also small. In RTiO_3 , the titanium moments couple ferromagnetically, so that the isotropic R-Ti coupling does not cancel. As a result, both the gadolinium and titanium moments in GdTlO_3 order at the same critical temperature of 34K (Greedan and MacLean, 1978). This is one order of magnitude larger than the critical temperature at which ordering of the rare earth moments in RMO_3 , $M = \text{Fe, Cr and Al}$ is observed. The fact that the gadolinium moments are ordered at such a high temperature is a

direct consequence of the non-vanishing isotropic R-Ti coupling. The critical temperature for GdTiO_3 is greater than that for YTiO_3 , which suggests that the R-Ti exchange coupling could be making a significant contribution compared with the Ti-Ti coupling.

1-5 MOLECULAR FIELD THEORY

The Hamiltonian for a system of identical non-interacting magnetic atoms with angular momentum J and magnetic moment μ_J , in the presence of a magnetic field H_0 along the z axis is given by

$$H = - \mu_{J_z} H_0 ,$$

with eigenvalues

$$E = -g\mu_B m H_0 , \quad m = J, \dots, -J . \quad (1-31)$$

Application of the standard techniques of statistical mechanics yields the magnetization of the system:

$$M = N \langle \mu_{J_z} \rangle ,$$

where

$$\langle \mu_{J_z} \rangle = \frac{\sum_{m=-J}^{+J} g\mu_B m e^{\frac{g\mu_B m H_0}{kT}}}{\sum_{m=-J}^{+J} e^{\frac{g\mu_B m H_0}{kT}}} , \quad (1-32)$$

and N is the number of magnetic atoms per unit volume. The expression can be reduced to the form (Smart, 1966)

$$M = Ng\mu_B J B_J(x) , \quad (1-33)$$

where $B_J(x)$ is called the Brillouin function, and

$$B_J(x) = \frac{2J+1}{2J} \coth\left(\frac{2J+1}{2J} x\right) - \frac{1}{2J} \coth \frac{x}{2J}$$

with

$$x = \frac{g\mu_B J H_0}{kT} \quad (1-34)$$

In the limit that $T \rightarrow 0$ or $H \rightarrow \infty$ ($x \gg 1$), the Brillouin function tends to unity. This corresponds to all of the magnetic moments being aligned parallel with the field, so the system has reached saturation. The high temperature, low field expansion of the Brillouin function is given by

$$B_J(x) = \frac{J+1}{3J} x \quad , \quad x \ll 1 \quad (1-35)$$

Under these conditions, the magnetization is equal to

$$M = \frac{Ng^2 \mu_B^2 J(J+1)}{3kT} H_0 \quad (1-36)$$

and the magnetic susceptibility becomes

$$\chi = \frac{M}{H_0} = \frac{Ng^2 \mu_B^2 J(J+1)}{3kT} = \frac{C}{T} \quad (1-37)$$

where

$$C = \frac{Ng^2 \mu_B^2 J(J+1)}{3k} \quad (1-38)$$

This is known as Curie's Law and it describes the paramagnetic susceptibility of a system of non-interacting magnetic moments for which J and m are good quantum numbers.

Systems that develop a spontaneous magnetization at a finite temperature must have interactions between the constituent magnetic moments as has already been discussed. The

earliest attempt to account for these interactions was made by Weiss (1907). He represented the interactions between a single magnetic atom and the rest of the crystal with an effective field. The effective field is assumed to be proportional to the average magnetic moment of the crystal and is written

$$H_e = \lambda M , \quad (1-39)$$

where λ is the molecular field coupling constant. The total field acting on a magnetic ion has contributions from both the external and the molecular field such that

$$H = H_0 + \lambda M . \quad (1-42)$$

It has already been shown that the paramagnetic susceptibility has the form

$$\chi = \frac{M}{H} = \frac{C}{T} . \quad (1-41)$$

This can be rearranged to give the magnetization:

$$M = \frac{C}{T} H , \quad (1-42)$$

where C/T is the susceptibility of a non-interacting system. When there are interactions between the constituent moments, the magnetization above the critical temperature can be expressed as

$$M = \frac{C}{T_0} H = \frac{C}{T} (H_0 + \lambda M) , \quad (1-43)$$

and

$$\chi = \frac{M}{H_0} = \frac{C}{T-\theta}, \quad \theta = \lambda C. \quad (1-44)$$

This is known as the Curie-Weiss law for ferromagnets and the Weiss constant, θ , is proportional to the molecular field coupling constant, λ . For antiferromagnets, $\lambda < 0$ and

$$\chi = \frac{C}{T+\theta}. \quad (1-45)$$

The interaction between two spins can be written in terms of the Heisenberg spin Hamiltonian

$$H_{ij} = -2J_{ij} \bar{S}_i \cdot \bar{S}_j. \quad (1-46)$$

In the spirit of the molecular field theory, the energy of interaction between the i^{th} spin and all of the remaining spins in the crystal is written as

$$H_i = -2\bar{S}_i \cdot \sum_j J_{ij} \bar{S}_{ij}. \quad (1-47)$$

This can be replaced by an interaction between a single spin and an effective field \bar{H}_i so that

$$H_i = -g\mu_B \bar{S}_i \cdot \bar{H}_i. \quad (1-48)$$

From these two equations we obtain an expression for the effective field \bar{H}_i :

$$\bar{H}_i = \frac{2}{g\mu_B} \sum_j J_{ij} \bar{S}_j. \quad (1-49)$$

If each spin is replaced by its average value $\langle \bar{S}_j \rangle$, the effective field becomes

$$\bar{H}_e = \frac{2(\sum_j J_j)}{Ng^2 \mu_B^2} \bar{M}, \quad (1-50)$$

where $\bar{M} = Ng\mu_B \langle \bar{S}_j \rangle$. The subscript i has been dropped since the effective field is the same for each magnetic atom. The subscript j refers to first, second, etc. neighbours. If only isotropic coupling is considered, \bar{H}_e and \bar{M} will be parallel. Therefore, we can drop the vector notation to write

$$\bar{H}_e = \frac{2(\sum_j J_j)}{Ng^2 \mu_B^2} M = \lambda M, \quad (1-51)$$

where

$$\lambda = \frac{2(\sum_j J_j)}{Ng^2 \mu_B^2}. \quad (1-51)$$

If the total field, $H = H_0 + \lambda M$, is substituted into the argument of the Brillouin function, the high temperature expansion of equation (1-33) becomes

$$M = \frac{Ng^2 \mu_B^2 S(S+1)}{3kT} (H_0 + \lambda M). \quad (1-52)$$

Writing the susceptibility $\chi = \frac{M}{H_0} = \frac{C}{T-\theta}$, we obtain an expression for θ :

$$\theta = \frac{2(\sum_j J_j) S(S+1)}{3k}. \quad (1-53)$$

In general, the magnetization is given by:

$$M = Ng\mu_B S B_S(x) \quad , \quad x = \frac{g\mu_B S}{kT} (H_0 + \lambda M) .$$

Since M appears in the argument of the Brillouin function, this equation must be solved by numerical or graphical techniques. The result is that, for zero applied field, there is a non-vanishing spontaneous magnetization below a critical temperature T_c , given by:

$$T_c = \frac{2(\sum_j J_j)S(S+1)}{3k} = \theta. \quad (1-54)$$

Therefore, molecular field theory predicts a spontaneous magnetization below a finite critical temperature. The magnitude of the critical temperature depends on the strength of the interactions between neighbouring spins. Figure 1-3 shows the reduced spontaneous magnetization $\sigma = M(T)/M(0)$ against the reduced temperature $\tau = T/T_c$ according to molecular field theory for spins $\frac{1}{2}$, $\frac{7}{2}$ and ∞ , taken from Smart (1966). Molecular field theory can be generalized to include ferromagnetic and antiferromagnetic interactions as well as lattices with more than one magnetic ion. The molecular field equations for the ferrimagnets, $RTiO_3$, are written down in detail in section 4-5 and the equation for the susceptibility above T_c , as a function of the molecular field coupling constants, is found in section 4-2.

For temperature approaching absolute zero,

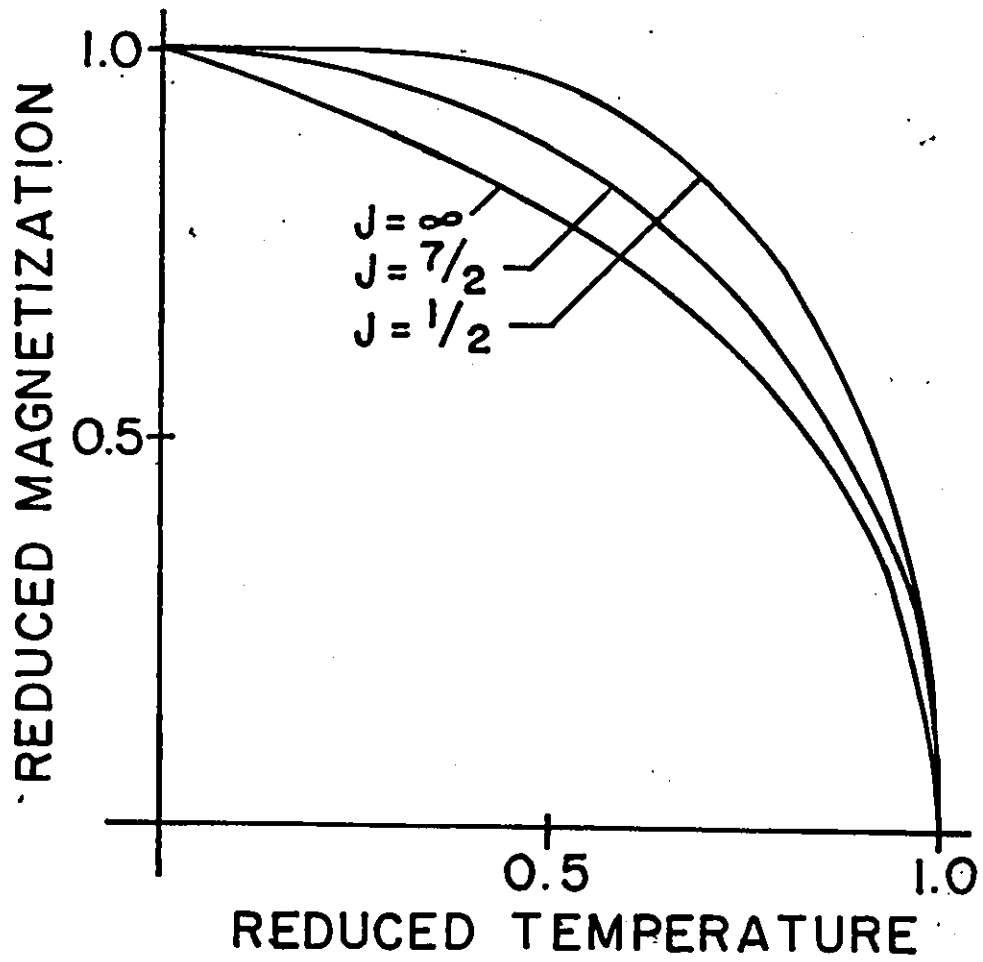


Fig. 1-3 Temperature dependence of the reduced magnetization for ferromagnets with $S = 1/2$, $7/2$ and ∞

$$\sigma = 1 - \frac{1}{S} \exp\left(-\frac{3}{S+1} \frac{T_c}{T}\right),$$

$$\lim_{T \rightarrow 0} \sigma = 1,$$

and

$$\lim_{T \rightarrow 0} \frac{d\sigma}{dT} = 0. \quad (1-55)$$

Thus, molecular field theory satisfies the third law of thermodynamics. Near the critical temperature,

$$\sigma \propto (T_c - T)^{1/2},$$

with the consequence that σ^2 should vanish linearly with temperature as $(T_c - T) \rightarrow 0$. Also, the heat capacity shows a discontinuity at $T = T_c$ which is characteristic of second order phase transitions.

Molecular field theory has had some qualitative success. It predicts a spontaneous magnetization at a finite critical temperature and it links the magnitude of T_c with the coupling constant λ . It satisfies the third law of thermodynamics near $T = 0$ and predicts a discontinuity in the heat capacity at the critical temperature. However, the quantitative predictions of the theory near $T = 0$ and $T = T_c$ are not borne out by experiment (Smart, 1966; Carlin, 1977). Experiments with ferromagnets have shown that the decrease of σ with increasing temperature just above absolute zero follows a $T^{3/2}$ law as predicted by spin wave theory (Smart, 1966). The susceptibility of ferromagnets shows deviations from the Curie-Weiss law near T_c which are not predicted by molecular field theory. Also, the

ratio T_c/θ is usually observed to be less than 1 for ferromagnets (Smart, 1966) whereas mean field theory predicts $T_c = \theta$.

Molecular field theory fails to predict the correct temperature dependence for σ near absolute zero because the effective field is proportional to the average magnetization. Therefore, it takes more energy to flip one spin than is required by spin wave theory where each spin flip is shared by many atoms. The interactions in mean field theory are effectively infinite in range, so no account is taken of the effects of short range order, which become important near T_c . Also, molecular field theory is independent of the dimensionality of the system. This has serious implications because the importance of short range order depends on the dimensionality of the spins and of the lattice (Carlin, 1977). With these shortcomings, molecular field theory is not reliable near $T = 0$ or $T = T_c$. However, it does work well for temperatures not too close to T_c or absolute zero. It will be used to analyze the paramagnetic susceptibility of the ferrimagnets, $RTiO_3$, in sections 4-1 and 4-5, for data collected between room temperature and temperature approximately 20K above T_c . In section 4-4, the temperature dependence of the reduced magnetization of $RTiO_3$, as determined by neutron diffraction, will be compared with the results of molecular field theory for data taken in the range $.20 \leq \tau \leq .98$. There are theories which go beyond

the simple assumptions of molecular field theory (Morrish, 1965; Smart, 1966), which try to take account of short range order or offer a better evaluation of the partition function. But these theories do not offer any significant improvement over mean field theory for the temperature range of interest and insofar as the analysis of the data in sections 4-1, 4-4 and 4-5 is concerned, the results of mean field theory are adequate.

1-6 SPIN CONFIGURATIONS OF IONIC STRUCTURES

Many ionic compounds of the general formula RMO_3 are known to undergo magnetic ordering (Goodenough and Longo, 1970). Although most of these materials have the same crystallographic structure, they differ in their magnetic structures. How many magnetic structures are possible for a given crystal structure-type, and what factors determine which magnetic structure will be the most stable one? Bertaut has developed a systematic way of approaching these questions using a technique known as representation analysis (Bertaut, 1963, 1967). The basic ideas of this method will be outlined below.

The theory applies to materials which have a well-defined crystal structure and which have magnetic cell parameters that are integral multiples of the chemical cell parameters. The following analysis is restricted to the case where the magnetic and chemical unit cells are the same size. The question is, what are the allowed spin configurations in this

crystal structure? The Hamiltonian must be invariant under spin reversal and symmetry operations of the crystallographic group. For the bilinear Hamiltonian

$$H = -2 \sum_{i,j} J_{ij} \bar{S}_i \cdot \bar{S}_j, \quad (1-56)$$

the allowed spin configurations are those which form basis functions for the irreducible representations of the space group. The product of any irreducible representation with itself will contain the symmetric representation, thus ensuring that the Hamiltonian will be invariant under all symmetry operations of the group.

The materials RMO_3 belong to the space group $\text{Pbnm} - (D_{2h}^{16})$. The M atoms are on the sites:

$$(4b) \quad \frac{1}{2} \ 0 \ 0 ; \frac{1}{2} \ 0 \ \frac{1}{2} ; 0 \ \frac{1}{2} \ \frac{1}{2} ; 0 \ \frac{1}{2} \ 0$$

which are centres of inversion. They are labelled 1, 2, 3 and 4 in figure 1-4. The R atoms occupy the sites:

$$(4c) \quad x, y, \frac{1}{4}; \bar{x}, \bar{y}, \frac{3}{4}; \frac{1}{2} + x, \frac{1}{2} - y, \frac{3}{4}; \frac{1}{2} - x, \frac{1}{2} + y, \frac{1}{4}.$$

The general position is 8-fold:

$$(8d) \quad \pm (x, y, z; \frac{1}{2} - x, \frac{1}{2} + y, \frac{1}{2} - z; \bar{x}, \bar{y}, \frac{1}{2} + z; \frac{1}{2} + x, \frac{1}{2} - y, \bar{z})$$

where 4a, 4b, 4c and 8d are the symbols used by the International Tables for Crystallography, Volume I, to label the different sites.

The generators of the group are the independent sym-

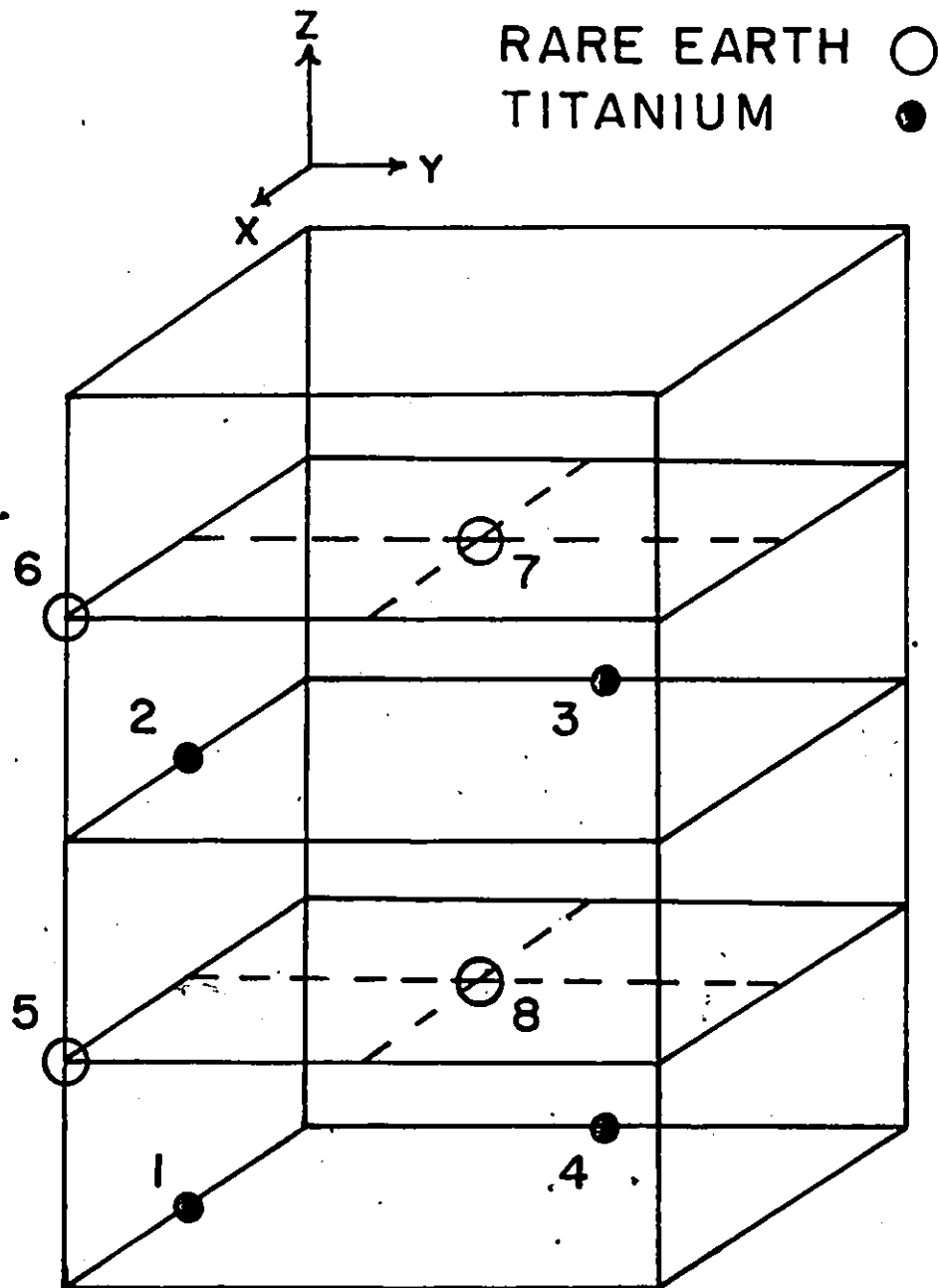


Fig. 1-4 Rare earth and titanium positions in the orthorhombic unit cell.

metry elements which will generate all of the equivalent points of the general position from a given point (x,y,z) . The choice of generators is not unique and could be the set b , n and m which specify the space group Pbnm. For the purpose of labeling to which irreducible representation the spin configurations belong, the following generators will be used:

$$2_1x \text{ at } (x, \frac{1}{4}, 0)$$

$$2_1y \text{ at } (x, y, \frac{1}{4})$$

$$\bar{1}$$

The first two are 2-fold screw axes and the third is the inversion operator. Since the spin configurations must form basis functions for the irreducible representations of the crystallographic space group, the appropriate linear combination of spins can be chosen by inspection of the character table. The translational symmetry of the spins is described by a propagation vector \bar{k} . For example, if $\bar{k} = \frac{1}{2} \bar{b}_3$, where \bar{b}_i is defined by $\bar{b}_i \cdot \bar{a}_j = \delta_{ij}$ for \bar{a}_j a lattice parameter, the phase factor $e^{2\pi i \bar{k} \cdot \bar{r}}$ would change sign for a translation of $\bar{r} = \bar{c}$ ($e^{2\pi i \frac{1}{2} \bar{b}_3 \cdot \bar{c}} = e^{\pi i} = -1$) corresponding to a spin reversal. This would result in a doubling of the magnetic unit cell along the c direction. Here, the magnetic and chemical unit cells are the same, and so $\bar{k} = 0$. The vector $\bar{k} = 0$ has the full symmetry of the point group; therefore, the character table for D_{2h} can be used to choose the basis vectors.

The character table for the point group D_{2h} (also $Pbnm$, $\bar{K} = 0$) is shown in table 1-1. The linear combinations of spins which transform like the irreducible representations of the point (space) group are

$$\begin{aligned} F &= \bar{S}_1 + \bar{S}_2 + \bar{S}_3 + \bar{S}_4 \\ G &= \bar{S}_1 - \bar{S}_2 + \bar{S}_3 - \bar{S}_4 \\ C &= \bar{S}_1 + \bar{S}_2 - \bar{S}_3 - \bar{S}_4 \\ A &= \bar{S}_1 - \bar{S}_2 - \bar{S}_3 + \bar{S}_4 \end{aligned} \quad (1-57)$$

The next step is to determine the transformation properties of these basis functions under the operations 2_{1x} , 2_{1y} and $\bar{1}$. It is easier to deal with the basis functions component by component. Starting with the transition metal spins located on the sites (4b), we can determine the transformation properties of the x, y and z components of the basis functions F, G, C and A under the three symmetry operations. The spins are axial vectors which transform according to (Arfken, 1970)

$$S'_i = |A| \sum_{j=1}^3 A_{ij} S_j \quad (1-58)$$

where A is an orthogonal matrix representing the symmetry operation and $|A|$ is its determinant. The transformation properties of axial vectors are summarized in figure 1-5. For example, if G_x represents the spin configuration $S_{1x} - S_{2x} + S_{3x} - S_{4x}$ for spins located on sites 1, 2, 3 and 4, then:

Table 1-1

Character table for the point group D_{2h} and the space group Pbnm ($\bar{k} = 0$).

	E	2_{1x}	2_{1y}	2_{1z}	$\bar{1}$	$2_{1x}\bar{1}$	$2_{1y}\bar{1}$	$2_{1z}\bar{1}$
Γ_1	1	1	1	1	1	1	1	1
Γ_2	1	1	-1	-1	1	1	-1	-1
Γ_3	1	-1	1	-1	1	-1	1	-1
Γ_4	1	-1	-1	1	1	-1	-1	1
Γ_5	1	1	1	1	-1	-1	-1	-1
Γ_6	1	1	-1	-1	-1	-1	1	1
Γ_7	1	-1	1	-1	-1	1	-1	1
Γ_8	1	-1	-1	1	-1	1	1	-1

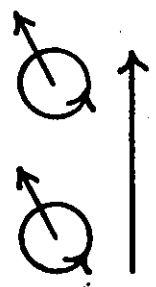
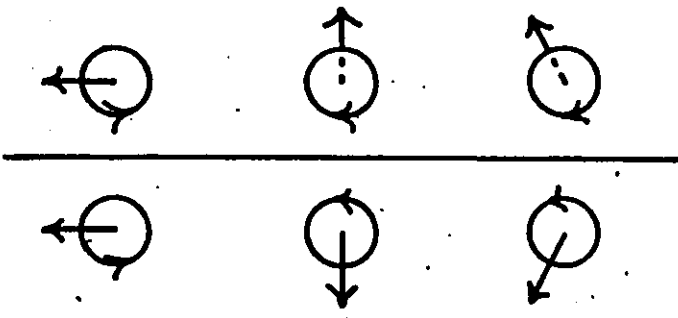
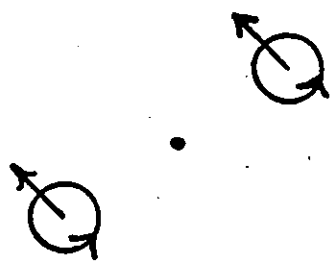
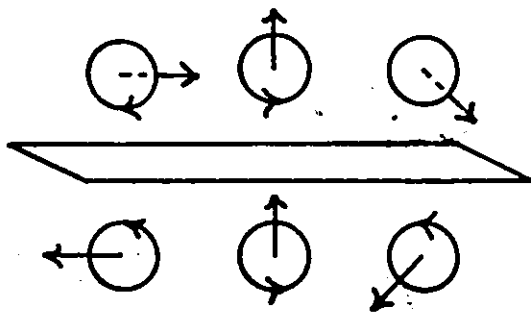
TRANSLATION-t	ROTATION-2	INVERSION- \bar{I}	REFLECTION-m
			

Fig. 1-5 Transformation properties of axial vectors (Donnay et al, 1958).

$$\begin{aligned}
 2_{1x} G_x &= 2_{1x} (S_{1x} - S_{2x} + S_{3x} - S_{4x}) = - G_x \\
 2_{1y} G_x &= 2_{1y} (S_{1x} - S_{2x} + S_{3x} - S_{4x}) = - G_x \\
 \bar{1} G_x &= \bar{1} (S_{1x} - S_{2x} + S_{3x} - S_{4x}) = G_x
 \end{aligned} \tag{1-59}$$

Therefore, G_x transforms as the irreducible representation labelled Γ_4 (---) for spins on the sites (4b). The same procedure can be applied to the spins on the rare earth sites (4c). In this case, G_x transforms as Γ_5 (+-), which means that for spins on these sites, the linear combination G_x changes sign under $\bar{1}$ but is invariant under 2_{1x} and 2_{1y} . The results for all the spin configurations on sites (4b) and (4c) are summarized in table 1-2.

The bilinear Hamiltonian must be invariant under symmetry operations of the group. Therefore, this Hamiltonian will only couple spin configurations which belong to the same irreducible representation, since the product of an irreducible representation with itself contains the symmetric representation. In the heavy rare earth titanium oxides, if the rare earth and titanium spins are coupled, then their spin configurations must belong to identical representations. This result plays an important role in the interpretation of the magnetic properties of these materials.

Table 1-2

Transformation properties in space group Pbnm

Representation	Transition Metal			Rare Earth		
Γ_1 (++++)	A_x	G_y	C_z			C_z
Γ_2 (+-+)	F_x	C_y	G_z	F_x	C_y	
Γ_3 (-++)	C_x	F_y	A_z	C_x	F_y	
Γ_4 (---+)	G_x	A_y	F_z			F_z
Γ_5 (++-)				G_x	A_y	
Γ_6 (+--)						A_z
Γ_7 (-+-)						G_z
Γ_8 (---)				A_x	G_y	

1-7 AN OVERVIEW OF NEUTRON SCATTERING

The theory of neutron scattering is well described in the literature (Bacon 1975, Gurevich and Tarasov 1968, Marshall and Lovesey 1971, Squires, 1978) and will not be reproduced here. Only those aspects of neutron scattering which are pertinent to the present investigation will be discussed.

A beam of neutrons which is directed towards a sample will be scattered by the nuclei in the sample. The incident neutrons can be described by a plane wave,

$$\psi_i = e^{ikz}, \quad (1-60)$$

where $k = 2\pi/\lambda$ is the wave number. For thermal neutrons, $\lambda \approx 1 \text{ \AA}$ which is much larger than the nuclear radius, so the scattering from a single nucleus is spherically symmetric. The scattered wave can be written as

$$\psi_s = -\frac{b}{r} e^{ikr}, \quad (1-61)$$

where r is the distance from the scattering centre and b is the scattering length. The total scattering cross section is defined as

$$\begin{aligned} \sigma &= \frac{\text{outgoing current of neutrons}}{\text{incident flux of neutrons}} \\ &= \frac{4\pi r^2 v \left| -\frac{b}{r} e^{ikr} \right|^2}{v \left| e^{ikz} \right|^2} \\ &= 4\pi b^2, \end{aligned} \quad (1-62)$$

provided that the outgoing current does not include unscattered neutrons from the incident beam.

The scattering length, b , is different for each isotope of an element. For those isotopes that have a nuclear spin I , there are different scattering lengths, b_+ and b_- , depending on whether the neutron spin is parallel or antiparallel to the nuclear spin. Consequently, when the neutrons are incident on a sample which is composed of a single element, the scattering lengths will change in a random fashion from site to site, provided that the isotopes are distributed randomly throughout the material. The wave scattered from an assembly of nuclei is written as

$$\psi_s = \sum_{\rho} -\frac{b_{\rho}}{r} e^{ikr} e^{i\bar{\rho} \cdot \Delta\bar{k}}, \quad (1-63)$$

where ρ is a vector from the origin to the ρ th nucleus and $|\bar{r}| \gg |\bar{\rho}|$, where \bar{r} is the distance to the scattering centre. The scattering vector $\Delta\bar{k}$ is equal to $\bar{k}_s - \bar{k}_i$ where \bar{k}_s and \bar{k}_i are the wave vectors of the scattered and incident neutrons respectively. The expression $e^{i\bar{\rho} \cdot \Delta\bar{k}}$ represents the phase difference between neutrons scattered from different points in the sample. If \bar{b} is the average scattering length of the element, then the scattering length at any site is

$$b_{\rho} = \bar{b} + (b_{\rho} - \bar{b}) \quad (1-64)$$

and the scattered wave becomes

$$\psi_s = \frac{e^{ikr}}{r} \sum_{\rho} (\bar{b} + (b_{\rho} - \bar{b})) e^{i\bar{\rho} \cdot \Delta \bar{k}} \quad (1-65)$$

The scattering intensity is proportional to $|\psi_s|^2$, thus we can write

$$I \propto \left| \frac{e^{ikr}}{r} \sum_{\rho} (\bar{b} + (b_{\rho} - \bar{b})) e^{i\bar{\rho} \cdot \Delta \bar{k}} \right|^2 \quad (1-66)$$

At unit distance from the sample,

$$\begin{aligned} I &\propto \left| \sum_{\rho} (\bar{b} + (b_{\rho} - \bar{b})) e^{i\bar{\rho} \cdot \Delta \bar{k}} \right|^2 \\ &= \sum_{\rho} \sum_{\rho'} (\bar{b}^2 + \bar{b}(b_{\rho} - \bar{b}) + \bar{b}(b_{\rho'} - \bar{b}) \\ &\quad + (b_{\rho} - \bar{b})(b_{\rho'} - \bar{b})) e^{i(\bar{\rho} - \bar{\rho}') \cdot \Delta \bar{k}} \\ &= \sum_{\rho} \sum_{\rho'} (\bar{b}^2 + (b_{\rho} - \bar{b})(b_{\rho'} - \bar{b})) e^{i(\bar{\rho} - \bar{\rho}') \cdot \Delta \bar{k}}, \end{aligned} \quad (1-67)$$

since the cross terms average to zero. The scattering intensity is the sum of two terms which represent coherent and incoherent scattering respectively. The coherent term is given by

$$\begin{aligned} I_{\text{coh}} &\propto \sum_{\rho} \sum_{\rho'} \bar{b}^2 e^{i(\bar{\rho} - \bar{\rho}') \cdot \Delta \bar{k}} \\ &= \left| \sum_{\rho} \bar{b} e^{i\bar{\rho} \cdot \Delta \bar{k}} \right|^2 \end{aligned} \quad (1.68)$$

The amplitude of the coherently scattered wave is summed over all the sites and the coherent scattering intensity is proportional to the total amplitude squared. The incoherent term is given by

$$\begin{aligned} I_{\text{incoh}} &\propto \sum_{\rho} \sum_{\rho'} (b_{\rho} - \bar{b})(b_{\rho'} - \bar{b}) e^{i(\bar{\rho} - \bar{\rho}') \cdot \Delta \bar{k}} \\ &= \sum_{\rho} (\bar{b} - b_{\rho})(\bar{b} - b_{\rho}) N \delta_{\bar{\rho}, \bar{\rho}'} \\ &= N(\bar{b}^2 - \bar{b}^2) \end{aligned} \quad (1-69)$$

The total incoherent scattering intensity is the sum of the incoherent scattering intensity from each site in the sample.

The position vector $\bar{\rho}$, defined as the vector from the origin to the ρ^{th} nucleus, can be replaced by

$$\bar{\rho} = \bar{\rho}_{m,n,p} + \bar{\rho}_j, \quad (1-70)$$

where $\bar{\rho}_{m,n,p}$ is a lattice vector defined as $\bar{\rho}_{m,n,p} = m\bar{a} + n\bar{b} + p\bar{c}$, from the origin to the unit cell m,n,p and m,n,p are integers,

and $\bar{\rho}_j$ is the position vector of the j^{th} nucleus in the unit cell.

Substitution of (1-70) into (1-68) leads to

$$\begin{aligned} I_{\text{coh}} &\propto \left| \sum_{m,n,p} \sum_{\rho_j} \bar{b}_j e^{i(\bar{\rho}_{m,n,p} + \bar{\rho}_j) \cdot \Delta \bar{k}} \right|^2 \\ &= \left| \sum_{m,n,p} e^{i(\bar{\rho}_{m,n,p} \cdot \Delta \bar{k})} \sum_{\rho_j} \bar{b}_j e^{i\bar{\rho}_j \cdot \Delta \bar{k}} \right|^2 \\ &= \left| N \delta(\bar{G} - \Delta \bar{k}) \sum_{\rho_j} \bar{b}_j e^{i\bar{\rho}_j \cdot \Delta \bar{k}} \right|^2, \end{aligned} \quad (1-71)$$

where $\bar{G} = h\bar{a}^* + k\bar{b}^* + l\bar{c}^*$ is a reciprocal lattice vector, and \bar{a}^* , \bar{b}^* , \bar{c}^* are reciprocal lattice parameters defined as (Ashcroft and Mermin, 1976)

$$\begin{aligned} \bar{a}^* &= \frac{2\pi(\bar{b} \times \bar{c})}{\bar{a} \cdot \bar{b} \times \bar{c}}, \\ \bar{b}^* &= \frac{2\pi(\bar{c} \times \bar{a})}{\bar{a} \cdot \bar{b} \times \bar{c}}, \\ \bar{c}^* &= \frac{2\pi(\bar{a} \times \bar{b})}{\bar{a} \cdot \bar{b} \times \bar{c}}. \end{aligned} \quad (1-72)$$

The coherent scattering will be zero unless $\Delta\bar{k}$ equals a reciprocal lattice vector. This is equivalent to Bragg's law:

$\lambda = 2d\sin\theta$, where d is parallel to the scattering vector $\Delta\bar{k}$.

The Bragg diffraction intensity for nuclear scattering is

$$I_{\text{coh}} \propto \left| N \sum_j \bar{b}_j \exp 2\pi i (hx_j + ky_j + lz_j) \right|^2 \quad (1-73)$$

and

$$\bar{\rho}_j = x_j \bar{a} + y_j \bar{b} + z_j \bar{c}, \quad (1-74)$$

where x_j, y_j, z_j are the fractional Cartesian coordinates of the j^{th} nucleus in the unit cell. So far, the nuclei have been treated as if they were static. In reality, the nuclei vibrate about their equilibrium positions so that they are not really point scatterers. This introduces a term e^{-2W} into the expression for the coherent scattering intensity, where W is called the Debye-Waller factor. Thus, the expression for the coherent nuclear scattering intensity is

$$I_{\text{coh}} \propto \left| N \sum_j \bar{b}_j \exp 2\pi i (hx_j + ky_j + lz_j) \right|^2 e^{-2W}. \quad (1-75)$$

The factor $\sum_j \bar{b}_j \exp 2\pi i (hx_j + ky_j + lz_j)$ is called the structure factor, F_{hkl} , as it provides structural information about the material under investigation.

The neutron has a magnetic moment of 1.91 nuclear magnetons. Therefore, when the atoms in a compound have unpaired electrons, there is an additional interaction between the magnetic moment of the neutron and the atomic magnetic moment.

This additional magnetic scattering enables neutron diffraction experiments to provide definitive proof of the existence of magnetic ordering and, under favourable conditions, to determine the magnetic structure. The magnetic scattering length can be defined as

$$P = gJ \left(\frac{e^2 \gamma}{2mc^2} \right) f \quad (1-76)$$

where:

- g = Landé factor
- J = angular momentum of the unpaired electrons
- γ = 1.91 nuclear magnetons
- f = form factor.

The form factor f arises from the interference between waves scattered from different regions of the unpaired electron density on the same atom. This factor did not occur in the expression for the nuclear scattering length because the neutron wavelength is large compared with the nuclear diameter. It could be argued that the Debye-Waller factor is the nuclear analog of the form factor. The differential cross section for magnetic scattering is defined as

$$d\sigma = q^2 p^2, \quad (1-77)$$

where

$$\bar{q} = \hat{\epsilon} (\hat{\epsilon} \cdot \hat{M}) - \hat{M}, \quad (1-78)$$

$\hat{\epsilon}$ = unit vector in the direction of $\Delta \bar{k}$,

\hat{M} = unit vector in the direction of the magnetic moment.

The magnitude of \bar{q} is equal to $\sin \alpha$, where α is the angle between $\hat{\epsilon}$ and \hat{M} . In a paramagnetic material, $\hat{\epsilon}$ and \hat{M} can assume all possible relative orientations, and so

$$\begin{aligned} d\sigma_{\text{para}} &= q^2 p^2 \\ &= \frac{2}{3} g^2 J(J+1) \left(\frac{e^2 \gamma}{2mc^2}\right)^2 f^2 \end{aligned} \quad (1-79)$$

since $\overline{\sin^2 \alpha} = \frac{2}{3}$.

For materials that undergo magnetic ordering

$$d\sigma = q^2 (gJ)^2 \left(\frac{e^2 \gamma}{2mc^2}\right)^2 f^2 \quad (1-80)$$

below the critical temperature. Since the magnetic moments are ordered, \bar{q} cannot take on all possible values, but only those for which \bar{q} is equal to $\hat{\epsilon}(\hat{\epsilon} \cdot \hat{M}) - \hat{M}$ and $\hat{\epsilon}$ is parallel to a reciprocal lattice vector. The intensity of the magnetic scattering from a Bragg plane depends on the relative orientation of the magnetic moment and the scattering vector $\Delta\bar{k}$ which is perpendicular to the plane. If the moments are perpendicular to the scattering plane, then α and q^2 are zero. Consequently, the intensity of the Bragg scattering is zero from the plane perpendicular to the magnetic moment.

The differential scattering cross section for nuclear plus magnetic scattering can be expressed as

$$d\sigma = b^2 + 2bp\bar{q} \cdot \bar{\lambda} + p^2 q^2, \quad (1-81)$$

where $\bar{\lambda}$ is a vector in the direction of the polarization of the

incident neutron. When the incident neutrons are not polarized, the average value of $\bar{q} \cdot \bar{\lambda}$ is zero; therefore,

$$d\sigma = b^2 + p^2 q^2 . \quad (1-82)$$

Hence, the nuclear and magnetic scattering intensities are additive. The total scattering intensity is proportional to $F^2 \exp(-2W)$ where

$$F_{\text{nuc}}^2 \propto \left| \sum_j \bar{b}_j \exp 2\pi i (hx_j + ky_j + lz_j) \right|^2 , \quad (1-83)$$

$$F_{\text{mag}}^2 \propto \left| \sum_j P_j \exp 2\pi i (hx_j + ky_j + lz_j) \right|^2 , \quad (1-84)$$

and the resultant F^2 is defined by

$$F^2 = F_{\text{nuc}}^2 + q^2 F_{\text{mag}}^2 . \quad (1-85)$$

In section 1-6, we showed that there are four different spin configurations for the rare earth and titanium moments, which were labelled:

$$\begin{aligned} F &= \bar{S}_1 + \bar{S}_2 + \bar{S}_3 + \bar{S}_4 \\ G &= \bar{S}_1 - \bar{S}_2 + \bar{S}_3 - \bar{S}_4 \\ C &= \bar{S}_1 + \bar{S}_2 - \bar{S}_3 - \bar{S}_4 \\ A &= \bar{S}_1 - \bar{S}_2 - \bar{S}_3 + \bar{S}_4 . \end{aligned} \quad (1-86)$$

If we substitute the above spin configurations into the magnetic

structure factor for the rare earth and titanium moments, we can determine the conditions for which $F_{\text{mag}} \neq 0$. The results for the reflections (h, k, ℓ) are

$$\begin{aligned} F: h + k &= 2n & \ell &= 2n \\ G: h + k &= 2n+1 & , \ell &= 2n+1 \\ C: h + k &= 2n+1 & , \ell &= 2n \\ A: h + k &= 2n & , \ell &= 2n+1 \end{aligned} \quad (1-87)$$

where n is an integer. The above conditions are rigorous for the titanium moments as they occupy special positions. The rare earths are not on special positions, so the above conditions are such that F_{mag} is a maximum.

In order to determine the magnetic structure of a material, it is necessary to know the space group of the chemical cell. Neutron diffraction patterns are then collected above and below the critical temperature. Additional diffraction effects which develop below T_c can be attributed to magnetic ordering, on the assumption that the chemical cell remains the same. The procedure will be outlined for the rare earth titanium oxides.

The chemical cell belongs to the space group $P6mm$, which means that the following reflections will be absent from the nuclear diffraction pattern (Woolfson, 1970):

$$\begin{aligned} (h, 0, 0) & , h = 2n+1 \\ (0, k, 0) & , k = 2n+1 \\ (0, 0, \ell) & , \ell = 2n+1 \\ (0, k, \ell) & , k = 2n+1 \\ (h, 0, \ell) & , h + \ell = 2n+1 \end{aligned} \quad (1-88)$$

If the magnetic and chemical unit cells are the same size, all magnetic reflections can be indexed using integral h, k and l . Otherwise, some reflections will appear with fractional indices. A ferromagnetic array of magnetic moments has the same symmetry as the chemical cell, and therefore the magnetic reflections will have the same systematic absences as the nuclear reflections. If additional magnetic reflections appear which are systematically absent in the nuclear pattern, then the ordered array of magnetic moments has less symmetry than the nuclear structure. Such is the case when the moments order antiferromagnetically. The moments may have one component that is ferromagnetic and one that is antiferromagnetic, which leads to a canted spin structure. If antiferromagnetic reflections are present, we can determine the spin configuration by examining the conditions for which $F_{\text{mag}} \neq 0$. The direction of the magnetic moments can be determined by identifying which reflections are absent that are otherwise allowed by the above conditions. This procedure can be complicated in practice due to the many overlapping reflections that occur in the diffraction pattern of polycrystalline samples.

1-8 THE CRYSTAL FIELD

When an ion is placed in a crystalline environment, it is subject to an electrostatic potential due to the neighbouring anions and cations. If the neighbouring ions are treated as point charges, the energy of this interaction can be written

$$H_{CF} = \sum_i \sum_j \frac{z_j e^2}{|\bar{r}_i - \bar{R}_j|}, \quad (1-89)$$

where \bar{r}_i and \bar{R}_j are the position vector of the i^{th} electron on the ion of interest and the j^{th} neighbouring ion respectively and z_j is the effective charge of the j^{th} neighbouring ion. The ion of interest is placed at the origin of the coordinate system. In the limit that $\bar{R}_j \gg \bar{r}_i$, $(\bar{r}_i - \bar{R}_j)^{-1}$ can be expanded as follows (Arfken, 1970):

$$\frac{1}{|\bar{r}_i - \bar{R}_j|} = \sum_{k=0}^{\infty} \frac{r_i^k}{R_j^{k+1}} P_k(\cos\theta), \quad (1-90)$$

where θ is the angle between \bar{r}_i and \bar{R}_j and $P_k(\cos\theta)$ is a Legendre polynomial. $P_k(\cos\theta)$ can be expressed in terms of spherical harmonics such that (Arfken, 1970)

$$P_k(\cos\theta) = \frac{4\pi}{2k+1} \sum_{q=-k}^{+k} Y_q^k(\theta_i, \psi_i) Y_{-q}^k(\theta_j, \psi_j). \quad (1-91)$$

Thus, the crystal field Hamiltonian can now be expressed as

$$H_{CF} = \sum_i \sum_j \sum_{k=0}^{+\infty} \sum_{q=-k}^{+k} \frac{z_j e^2 4\pi r_i^k}{(2k+1) R_j^{k+1}} Y_q^k(\theta_i, \psi_i) Y_{-q}^k(\theta_j, \psi_j). \quad (1-92)$$

A term can be isolated which depends only on the crystalline environment. This term, labelled A_q^k , is composed of

$$A_q^k = \sum_j \frac{z_j e^2}{R_j^{k+1}} \sqrt{\frac{4\pi}{2k+1}} Y_{-q}^k(\theta_j, \psi_j). \quad (1-93)$$

A_q^k and r^k are often combined to form B_q^k , which is called the

crystal field intensity. If we replace the spherical harmonic $Y_q^k(\theta_i, \psi_i)$ with the tensor operator $C_q^k = \sqrt{\frac{4\pi}{2k+1}} Y_q^k$, the crystal field Hamiltonian becomes

$$H_{CF} = \sum_i \sum_{k=0}^{\infty} \sum_{q=-k}^{+k} B_q^k C_q^k(\theta_i, \psi_i),$$

$$= \sum_{k=0}^{\infty} \sum_{q=-k}^k B_q^k C_q^k, \quad (1-94)$$

where

$$C_q^k = \sum_i C_q^k(\theta_i, \psi_i). \quad (1-95)$$

For the f^N configuration of the rare earth ion, the matrix elements of H_{CF} are given by:

$$\langle f^N SLJM_J | H_{CF} | f^N SL'J'M_J' \rangle = \sum_{k,q} B_q^k \langle f^N SLJM_J | C_q^k | f^N SL'J'M_J' \rangle, \quad (1-96)$$

where

$$\langle f^N SLJM_J | C_q^k | f^N SL'J'M_J' \rangle = (-1)^{J-J_z} \begin{pmatrix} J & K & J' \\ -M_J & q & M_J' \end{pmatrix} \langle f^N SLJ || C^k || f^N SL'J' \rangle \quad (1-97)$$

$$\langle f^N SLJ || C^k || f^N SL'J' \rangle = (-1)^{S+L+J'+K} \sqrt{(2J+1)(2J'+1)} \begin{Bmatrix} J & J' & K \\ L' & L & S \end{Bmatrix}$$

$$\times \langle f^N SL || C^k || SL' \rangle, \quad (1-98)$$

and

$$\langle f^N SL || C^k || f^N SL' \rangle = \langle f^N SL || U^k || f^N SL' \rangle \langle f || C^k || f \rangle. \quad (1-99)$$

The above equations are derived in detail in the literature (Judd 1963, Silver 1976, Wybourne 1965). The reduced matrix element $\langle f || C^k || f \rangle$ imposes the condition $k \leq 6$, since $\ell = 3$ for

an f electron. Also, $\langle f || C^k || f \rangle$ will vanish unless k is even, as a result of parity. The 3-j symbol $\begin{pmatrix} J & K & J' \\ -M_J & q & M_J' \end{pmatrix}$ imposes the further restriction that $M_J + q + M_J' = 0$. U^k is an n -electron unit operator such that

$$U^k = \sum_{i=1}^n u_i^k \quad \text{and} \quad \langle f || u_i^k || f \rangle = 1, \quad (1-100)$$

where u_i^k is a 1-electron unit operator. The 3-j symbol $\begin{pmatrix} J & K & J' \\ -M_J & q & M_J' \end{pmatrix}$ and the 6-j symbol $\begin{Bmatrix} J & J' & K \\ L' & L & S \end{Bmatrix}$ have been tabulated by Rotenberg *et al.* (1959) and the reduced matrix elements $\langle SL || U^k || SL' \rangle$ and $\langle f || G^k || f \rangle$ have been calculated by Nielson and Koster (1963).

With these restrictions, the Hamiltonian simplifies to

$$H_{CF} = \sum_{k=0}^6 \sum_{q=-k}^{+k} B_q^k C_q^k, \quad k = 0, 2, 4, 6. \quad (1-101)$$

Many terms in the expansion of H_{CF} will vanish due to symmetry. For example, the rare earth ion in $RTiO_3$ occupies a site of mirror symmetry. The requirement that the Hamiltonian be invariant under all symmetry operations of the point group imposes the condition $k+q = 2n$, for n an integer. Since k is already restricted to even values, q must also be even. However, the crystal field Hamiltonian still has fifteen terms. Sites with higher symmetry impose more stringent conditions on k and q , and so the number of terms in the crystal field Hamiltonian decreases.

Equation (1-96) is completely general as it calculates the matrix elements of H_{CF} between states with different L, S ,

J and M_J . If the free ion multiplets are well separated in energy, then only the interaction between components of the same multiplet needs to be considered. Under this condition, the Hamiltonian is diagonalized with the free ion wavefunctions as a basis set. In the intermediate coupling scheme, matrix elements are calculated between multiplets that differ in L and S but which have the same J . The wavefunctions which form the basis for the diagonalization of H_{CF} are linear combinations of LS functions with constant J . If the free ion multiplets are not well separated, then the effects of J - J mixing must be taken into consideration (Dieke, 1968).

The point charge model of the crystal field has some severe limitations as it essentially ignores the overlap of the electronic wavefunctions in the crystal. Although this approximation is better for the $4f$ electrons than for the $3d$ electrons, it is still rather poor. Consequently the crystal field intensities, B_q^k , are usually treated as adjustable parameters to be fitted to experimental data, rather than to be calculated from first principles. Still, the point charge model has been used successfully in the interpretation of the optical spectrum of many rare earth and transition metal ions in crystal lattices. Once the energy levels of an ion have been fitted to a crystal field Hamiltonian, the appropriate ionic wavefunctions can be constructed as linear combinations of the free ion

wavefunctions. From a knowledge of the wavefunctions and energy levels, magnetic properties such as the magnetic susceptibility or the preferred direction of magnetization can, in principle, be calculated.

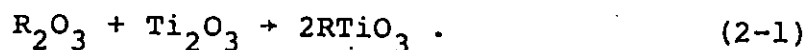
CHAPTER 2

SAMPLE PREPARATION AND CHARACTERIZATION

2 - 1 SAMPLE PREPARATION

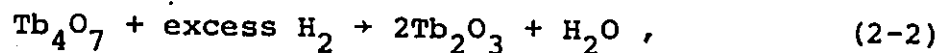
General Preparation Schemes

All samples with the exception of YbTiO_3 and LuTiO_3 were prepared as single phases by the following solid state reaction at a temperature of 1600°C :



This reaction temperature is below the melting point of both the reactants and the products. If the reaction was carried out in the molten state, the product included some pyrochlore phase $\text{R}_2\text{Ti}_2\text{O}_7$. The presence of any competing phase in the product was determined by powder X-ray diffraction.

R_2O_3 of 99.99% purity was obtained from Research Chemicals and pre-fired at 1000°C to drive off any hydroxides or carbonates. Tb_2O_3 had to be prepared by the reduction of Tb_4O_7 with H_2 at 1200°C :

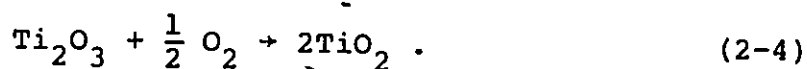


as terbium can exist in the 3^+ or 4^+ oxidation state.

Ti_2O_3 was prepared by the following reaction:



TiO_2 of 99.95% purity was obtained from Atomergic Chemicals Company and the titanium sponge was supplied by Ven-tran. Stoichiometric amounts were mixed together with a mortar and pestle, and then pressed into pellets which were arc melted on a water-cooled copper hearth under half an atmosphere of purified argon. The stoichiometry of the product was determined by measuring the oxidative weight gain of a small portion (~ 100 mg) of the product according to



Either TiO_2 or Ti was added and the product remelted until the stoichiometry was adjusted to $\text{TiO}_{1.500 \pm 0.005}$.

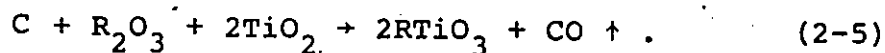
The prefired R_2O_3 and $\text{TiO}_{1.500}$ were mixed together in stoichiometric quantities using a mortar and pestle and then pressed into pellets. The pellets were sealed in a molybdenum crucible under half an atmosphere of purified argon and heated for twelve hours at 1600 C in a radio frequency induction furnace which had been evacuated to 10^{-5} torr. By this method, single phase products were obtained for $\text{R} = \text{Tb, Dy, Ho, Er}$ and Tm and used for bulk magnetic measurements.

YbTiO_3 and LuTiO_3

The method was not successful in producing single phase YbTiO_3 or LuTiO_3 . An examination of the products by powder

X-ray diffraction revealed prominent reflections due to $\text{Yb}_2\text{Ti}_2\text{O}_7$ and Lu_2O_3 respectively. A 32 mg sample of single phase LuTiO_3 in the form of small crystallites on the pellet surface was obtained by heating the pelletized reaction products in a closed molybdenum crucible sealed under half an atmosphere of purified argon at 1600 C for 72 hours. It was used for the bulk magnetic measurements.

Further attempts were made to produce YbTiO_3 and LuTiO_3 without impurity phases through the following synthesis described by Bazuev and Shveikin (1977).



The Gibbs free energy of reaction was calculated to be - 18 Kcal. per mole at 1600 C. Powder X-ray diffraction experiments showed that the products included small amounts of the pyrochlore phase. Attempts to eliminate the pyrochlore by heating the sample under a reducing atmosphere of hydrogen at 1200 C were not successful.

Sample Preparation for Neutron Diffraction

Equimolar quantities of R_2O_3 and Ti_2O_3 were mixed together with a mortar and pestle and pressed into pellets. These pellets were arc melted on a water-cooled copper hearth under half an atmosphere of purified argon. A disadvantage of this preparation is that a small amount of pyrochlore appears upon melting. This was not considered serious for neutron diffraction measurements as the pyrochlore reflections were easily identi-

fied. The advantage of the method is that it allows larger quantities of material to be prepared, which are necessary for neutron diffraction experiments.

Crystal Growth

Various attempts were made to grow single crystals from the melt. Crystals ranging in mass from 12mg. to 60mg. were obtained for ErTiO_3 and HoTiO_3 with the Czochralski technique and a Centorr modified tri-arc crystal growing apparatus (Reed, 1968). The charge was melted in a water-cooled molybdenum hearth under a continuous flow of argon gas and the crystals were pulled with a water-cooled tungsten seed rod. Stable growth conditions could be maintained for approximately two hours with a charge of 2.5 g. and a pulling rate of 1 cm. per hour.

2-2 SAMPLE ANALYSIS

The crystal structures of selected members of the series RTiO_3 have previously been solved (MacLean, Ng and Greedan, 1979). The materials crystallize in the GdFeO_3 -type structure which is an orthorhombic distortion of the cubic perovskite. The space group is Pbnm and there are four formula units per unit cell, It was assumed that the heavy rare earth titanium oxides would also crystallize in the GdFeO_3 structure and the lines in the X-ray diffraction patterns were indexed accordingly. The magnetic structures and the nuclear contribution to the neutron diffraction intensities are consistent with the space group Pbnm as will be shown in a later chapter.

The results of the X-ray powder diffraction data for DyTiO_3 are given in table 2-1. They are typical of other members of the series. The data were analyzed for an orthorhombic unit cell and the agreement is excellent. Table 2-2 shows the unit cell parameters calculated for all members of the series with a least squares refinement of at least sixteen unambiguous reflections. The peak positions were corrected to an internal silicon standard.

Figure 2-1 shows a plot of unit cell volume against the trivalent rare earth radius cubed in eight-fold coordination (Shannon and Prewitt, 1969). The linear relationship indicates that the change in cell volume is governed by the volume occupied by the rare earth ion and that there is no change in the crystal structure across the series.

The extent of non-stoichiometry of the materials was checked by measuring the oxidative weight gain, a technique known as thermal gravimetric analysis. Nonstoichiometry has been investigated in perovskite structures ABO_3 and three models have been proposed (Tofield and Scott, 1974):

- a) Interstitial oxygen may be present on sites of low electrostatic potential.
- b) Vacancies may exist on both A and B sites leaving a perfect oxygen lattice.
- c) Vacancies may exist on the A site only.

Another means of maintaining perfect B cation and oxygen lattices at the expense of A cation vacancies is the formation of a second phase but it would be detected by X-ray or neutron dif-

Table 2-1

Observed and calculated d-spacings for DyTiO₃
determined by powder X-ray diffraction (CuK_α
radiation)

h k l	d (observed)	d (calc)
1 1 0	3.881	3.897
0 0 2	3.821	3.827
1 1 1	3.468	3.473
0 2 0	2.839	2.841
1 1 2	2.728	2.731
2 0 0	2.679	2.678
0 2 1	2.666	2.663
2 1 1	2.309	2.309
2 0 2	2.194	2.194
;1 1 3	2.131	2.135
2 2 0	1.947	1.948
0 0 4	1.915	1.914
2 2 1	1.889	1.888
3 0 1	1.739	1.739
1 3 2	1.618	1.618
2 2 3	1.551	1.549

Table 2-2

Unit cell parameters for RTiO_3 , R = Tb-Lu

RTiO_3	a (Å)	b (Å)	c (Å)	Vol. (Å) ³
TbTiO ₃	5.355 (2)	5.665 (2)	7.647 (r)	232.0
DyTiO ₃	5.355 (2)	5.681 (2)	7.655 (3)	232.9
HoTiO ₃	5.347 (2)	5.672 (5)	7.621 (5)	230.9
ErTiO ₃	5.295 (2)	5.649 (2)	7.588 (2)	226.9
TmTiO ₃	5.293 (2)	5.648 (2)	7.586 (3)	226.8
YbTiO ₃	5.288 (3)	5.638 (3)	7.585 (4)	226.1
LuTiO ₃	5.282 (2)	5.617 (1)	7.583 (3)	225.0

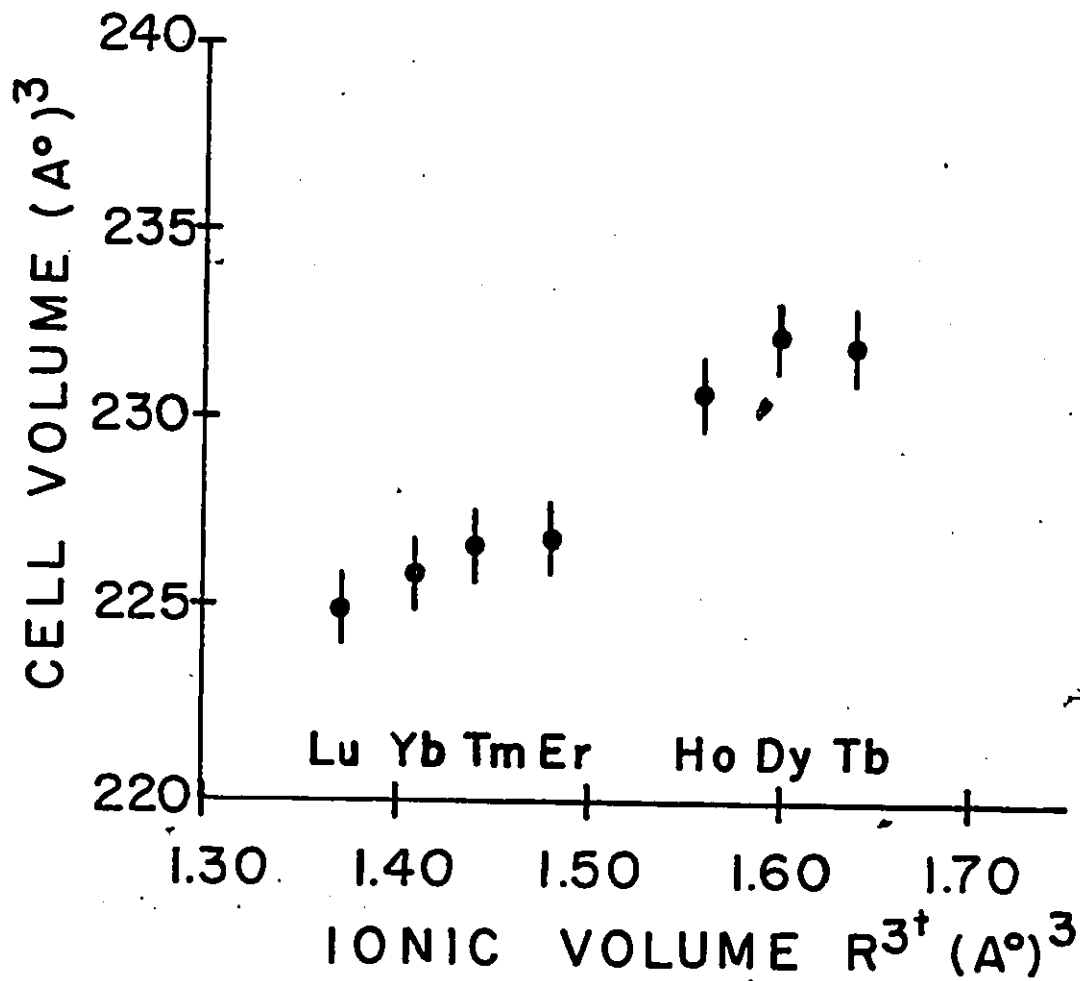
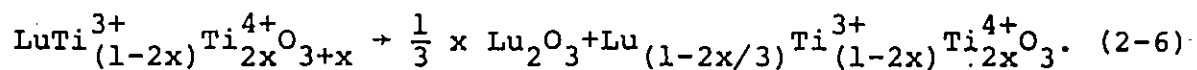


Fig. 2-1 Unit cell volumes for $RTiO_3$, R = Tb-Lu.

fraction. The Lu_2O_3 phase in the LuTiO_3 preparation may arise from (Tofield and Scott, 1974)

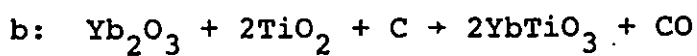
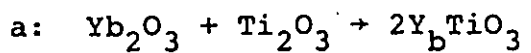


The results of the thermal gravimetric analysis are listed in table 2-3. No attempt has been made to fit these data to any particular model. In every case, except YbTiO_3 , the experimental results are within a few percent of the calculation based on a stoichiometric product. Table 2-3 also includes the R:Ti ratios determined by neutron activation analysis where possible.

Table 2-3

Results of thermogravimetric and neutron activation analyses

$RTiO_3$	% mass gain (exp)	% mass gain (theo)	R:Ti
TbTiO ₃	3.13	3.14	
DyTiO ₃	2.99	3.10	
HoTiO ₃	3.06	3.07	1.02±.01
ErTiO ₃	2.99	3.04	.998±.010
TmTiO ₃	3.09	3.02	
YbTiO ₃ a	2.37	} 2.98	
YbTiO ₃ b	2.66		
LuTiO ₃	2.89	2.95	



CHAPTER 3

EXPERIMENTAL PROCEDURES

3-1 INTRODUCTION

Bulk magnetic data, collected as a function of temperature and applied magnetic field can provide much useful information about the magnetic properties of a material. However, these data do not necessarily give information regarding the microscopic magnetic properties such as the magnitude and direction of the magnetic moments in the crystal lattice. This information can, in principle, be determined from magnetic neutron diffraction experiments. The following sections outline the experimental procedures used to investigate both the macroscopic and the microscopic magnetic properties of the heavy rare earth titanium oxides.

3-2 BULK MAGNETIC MEASUREMENTS

Data were collected from polycrystalline samples of mass 100 mg. to 400 mg.³⁴ in the form of a finely ground powder pressed into 3/16" pellets. The pellets were fastened with ceramic cement (Sauerisen Cement Company, Pittsburgh) to a 1/4" O.D. quartz tube. For ErTiO_3 and HoTiO_3 , data were also collected from single crystals of mass 14 mg. and 42 mg. respectively. These crystals were aligned by X-ray diffraction tech-

niques and fastened to the quartz tube with G.E. 7031 low temperature varnish. This varnish is soluble in a 50:50 volume solution of toluene and methanol which allows the crystals to be retrieved and remounted in different orientations.

Magnetic data were collected at temperatures ranging from 4.2K to 300K using a Princeton Applied Research vibrating sample magnetometer. Magnetic fields up to 15 kilogauss were provided by a Magnion water-cooled electromagnet with the sample maintained in a liquid helium cryostat (Andonian Assoc.). For magnetic fields up to 60 kilogauss, the sample was placed in another cryostat (Sulfrian Cryogenics) containing a superconducting solenoid.

The temperature of the sample was measured with a calibrated chromel vs. gold - .07 atomic percent iron thermocouple. A small heater in the tail of the Andonian cryostat allowed temperatures up to 300K to be achieved.

Voltages proportional to the magnetization, temperature or applied field were collected by an on-line Texas Instruments computer which averaged the voltage proportional to the sample magnetization over one degree intervals in temperature or 500 gauss intervals in magnetic field. The magnetometer was calibrated with a pure nickel sphere of mass .07507 g. The accepted value for the magnetization of nickel at room temperature, $55.11 \pm .06 \text{ emu-g}^{-1}$, was used.

3-3 NEUTRON DIFFRACTION MEASUREMENTS

Neutron diffraction data were collected from polycrystalline samples above and below the critical temperature. The measurements were made at the McMaster Nuclear Reactor with the triple axis spectrometer in the double axis mode. This instrument is fully described in reference (Rowe, 1966). A monochromatic beam of wavelength 1.40 \AA was obtained from the (200) reflection of a single crystal of copper. The instrumental resolution, the zero angle and exact neutron wavelength were determined by measuring the diffraction peaks from finely divided polycrystalline copper. The full width at half maximum for a single reflection was .86 degrees in the parallel position which occurred at a scattering angle of about 45 degrees.

ErTiO₃ and HoTiO₃

Several grams of loosely packed powder were placed in a flat sample holder with vanadium windows. This sample holder was placed in a Sulfrian cryostat. Data were collected at scattering angles ranging from 10 degrees to 65 degrees at intervals of .2 degrees and temperatures of 4.2K and 298K. The sample temperature was monitored by a 100 ohm carbon resistance thermometer.

TbTiO₃, DyTiO₃, TmTiO₃ and YbTiO₃

A cylindrical thin-walled vanadium sample holder was used for TbTiO₃, TmTiO₃ and YbTiO₃ while DyTiO₃ was mounted in a flat geometry due to the large absorption cross section of

dysprosium. Several grams of sample were used in each case, maintained in a Displex Closed-Cycle Refrigeration System (Air Products and Chemicals, Inc.). Data were collected at scattering angles ranging from 10 degrees to 65 degrees in intervals of .2 degrees at temperatures of 10K and 100K. The temperature was measured using a calibrated chromel vs. gold - .07 atomic per cent iron thermocouple and was varied with an Air Products model APD-B temperature controller.

The Air Products Displex Refrigeration System and temperature controller were used for measurements of the temperature dependence of the magnetic scattering intensity for all of the materials mentioned above except YbTiO_3 . The experiment was not performed for YbTiO_3 due to the very small magnetic enhancement of the nuclear peaks found for this compound. This rendered the magnetic scattering too small for its temperature dependence to be measured with useful accuracy.

3-4 ALIGNMENT OF THE SINGLE CRYSTALS

The pseudo-cubic symmetry of this system can be exploited during the alignment of single crystals by the Laue method. The relationship between the orthorhombic unit cell and the pseudo-cubic unit cell is shown in figure 1-1. The pseudo-cubic $\langle 110 \rangle$ directions correspond to the orthorhombic a and b axes plus directions approximately 45° from the c axis in the orthorhombic $\{110\}$ planes. The Laue photograph provides

enough useful information to determine the orientation of the crystal axes relative to the incident beam, even when this alignment is arbitrary. This is not so with precession photographs. Once the Laue technique has been used to align the pseudo-cubic $\langle 110 \rangle$ direction parallel to the incident beam, the precession camera can be used for final adjustments and to determine which axis in the orthorhombic system is parallel to the beam. The oriented crystal can now be transferred to the experimental apparatus. Figure 3-1 shows a crystal of ErTiO_3 having been transferred from a goniometer to a quartz tube which is held by an xyz manipulator. The sample can now be transferred to the magnetometer for magnetic measurements.

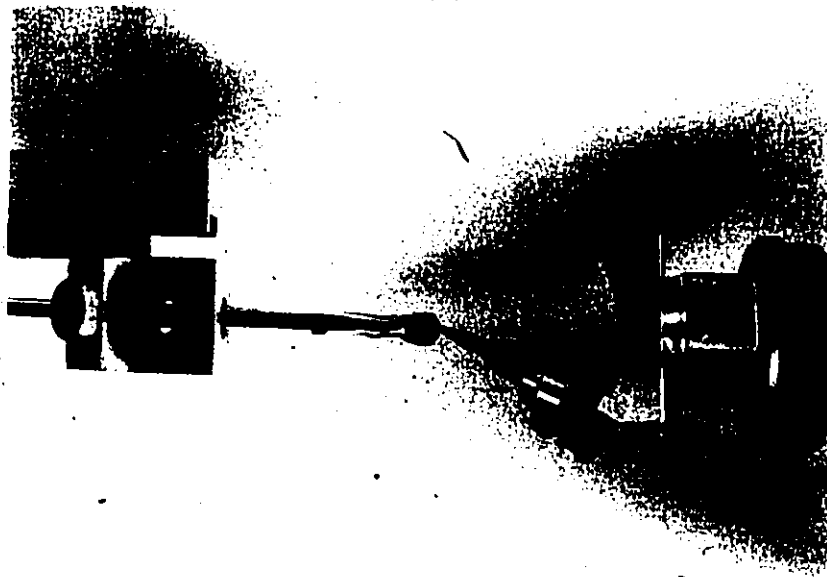


Fig. 3-1 The crystal of ErTiO_3 has been transferred from the goniometer to a quartz tube which is held by an xyz manipulator.

CHAPTER 4

EXPERIMENTAL RESULTS AND DISCUSSION

4-1 BULK MAGNETIC MEASUREMENTS

Figures 4-1a and 4-1b show the net magnetization cubed plotted as a function of temperature for the heavy rare earth-titanium oxide series. The marked change in the magnetization, which occurs over a broad range of temperature, is evidence for the onset of long range magnetic order. Molecular field theory predicts that the temperature dependence of the spontaneous magnetization will follow a Brillouin function (Smart, 1966):

$$B_J(x) = \frac{2J+1}{2J} \coth\left(\frac{2J+1}{2J} x\right) - \frac{1}{2J} \coth\left(\frac{x}{2J}\right),$$

J = free ion atomic angular momentum ,

$$x = \frac{g\mu_B J(H+\lambda M)}{kT} \quad (4-1)$$

For temperatures just below the critical temperature T_c , molecular field theory predicts that the spontaneous magnetization will be proportional to $T^{1/2}$. However, accurate NMR measurements on the insulating ferromagnet EuS give an exponent closer to 1/3 (Heller and Benedek, 1965). Therefore, it is the net magnetization cubed which is plotted against temperature in figure 4-1.

The critical temperature, below which the material de-

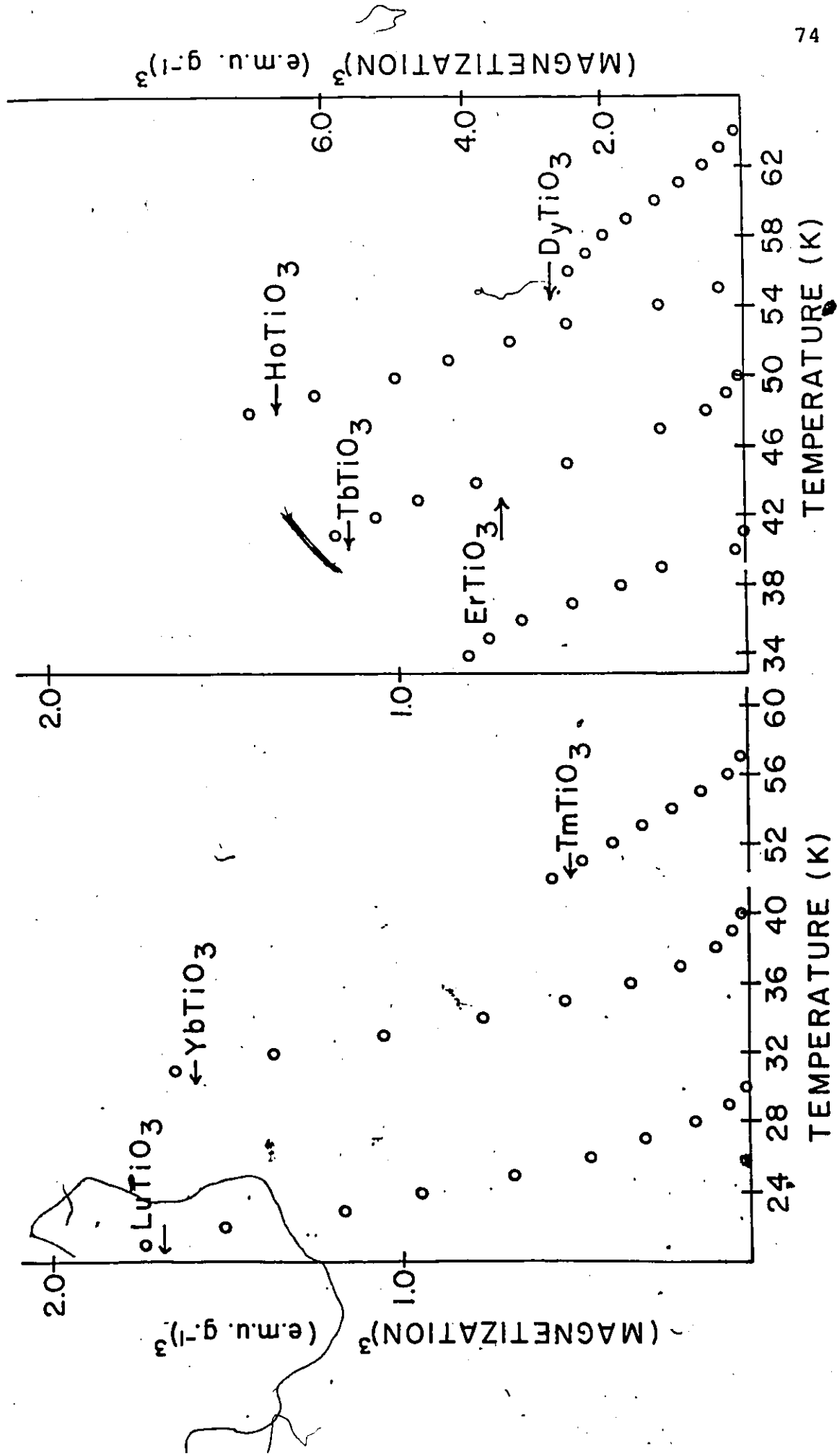


Fig. 4-1

a) Magnetization cubed versus temperature for $R\text{TiO}_3$, $R = \text{Tm, Yb and Lu.}$
 b) Magnetization cubed versus temperature for $R\text{TiO}_3$, $R = \text{Tb, Dy, Ho and Er.}$

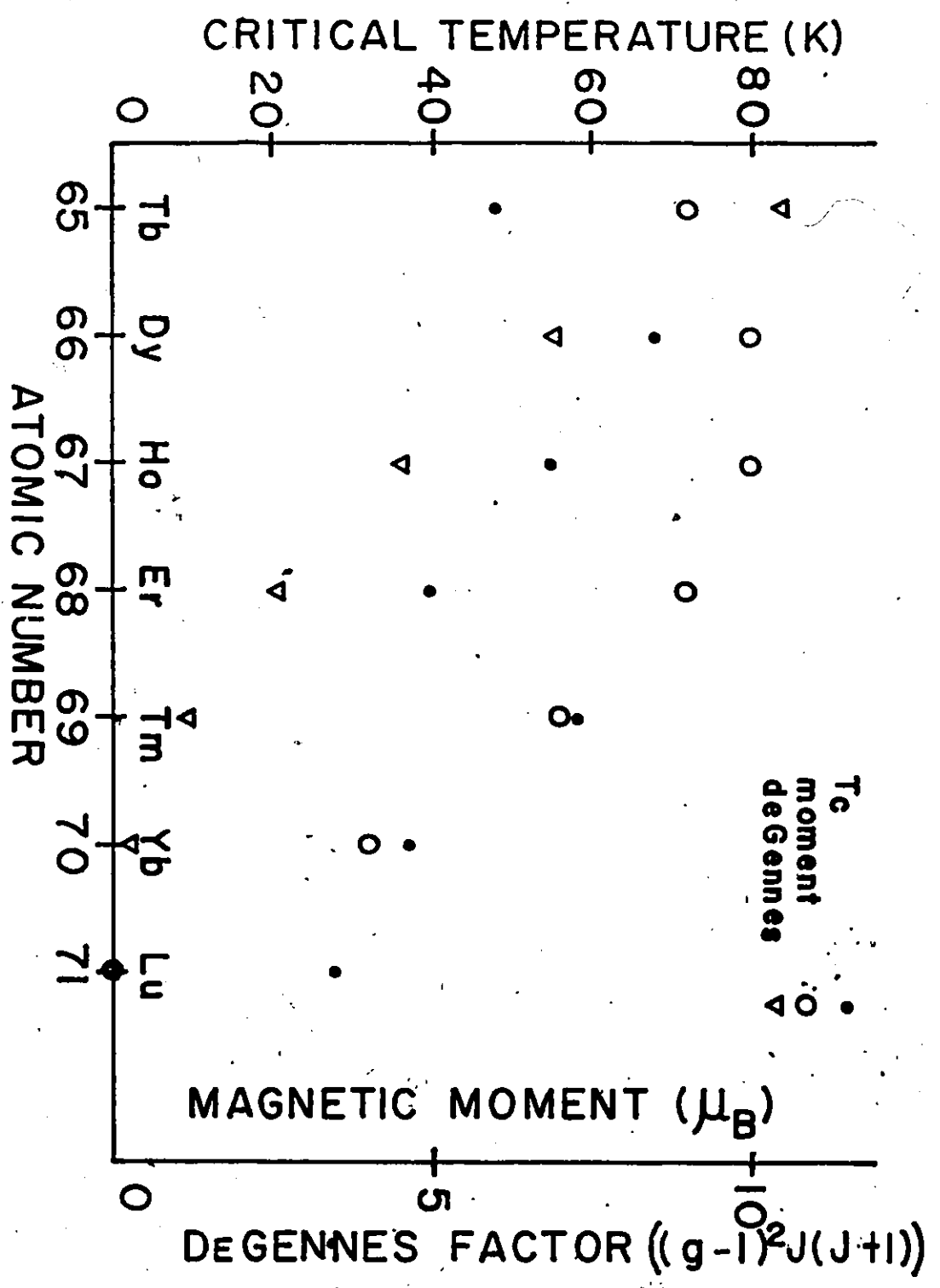


Fig. 4-2 Critical temperature, de Gennes factor and magnetic moment for $RTrIO_3$, R = Tb-Lu.

velops a spontaneous magnetization, is taken to be the intersection of the linear portion of the curve with the temperature axis. Some magnetization persists above the critical temperature due to short range order.

Figure 4-2 shows the critical temperature, the free ion magnetic moment and the de Gennes factor, $(g-1)^2 J(J+1)$, plotted against the rare earth atomic number. There is no obvious correlation between the critical temperature and either the free ion moment or the de Gennes factor. This is not surprising for the latter as T_c should only vary smoothly with $(g-1)^2 J(J+1)$ in systems where the R-R interactions are dominant (Wallace, 1973) and the exchange mechanism is RKKY coupling. Since the 3d wavefunctions are extended further into space than the 4f wavefunctions, one would expect the relative strengths of the cation-cation interactions to be Ti-Ti > R-Ti > R-R. For constant Ti-Ti coupling, we could argue that the critical temperature might vary with the strength of the R-Ti exchange. However it is surprising that this interaction should vary in the manner suggested by the critical temperatures. Without a theory for calculating the R-Ti exchange, one must resort to experiment. Measurement of the spin wave dispersion by inelastic neutron scattering is probably the best way to determine exchange coupling constants. However, this method requires large (~ 1 c.c.) single crystals which are not yet available for these materials. Therefore, coupling constants were

determined by fitting the paramagnetic susceptibility of polycrystalline samples to a model based on molecular field theory. The procedure is outlined in the next section.

One final comment on figure 4-1 is necessary. When a ferrimagnet or ferromagnet is cooled below its critical temperature, the magnetic moments begin to line up within regions called domains. The domains are oriented with respect to one another to give zero, or nearly zero, net magnetization. Imperfections in the crystal lattice, anisotropy, the arbitrary shape of the crystallites and the small residual magnetic field prevent an exact cancellation of the contributions from each domain and so there will be a small net magnetization (Morrish, 1965; Cullity, 1972). It is this magnetization cubed that is plotted in figures 4-1a and 4-1b. It should not be confused with the saturation magnetization which results when the sample consists of one large domain whose magnetization is parallel to the applied magnetic field.

The temperature dependence of the inverse magnetic susceptibility in the paramagnetic regime is shown in figure 4-3 for RTiO_3 , $R = \text{Gd, Tb, Dy, Ho, Er and Tm}$. Data were not collected for YbTiO_3 or LuTiO_3 as they could not be prepared as single phases. The hyperbolic shape of the curves is indicative of ferrimagnetism. In this case, the ferrimagnetism arises from the antiparallel coupling of the rare earth moment with the

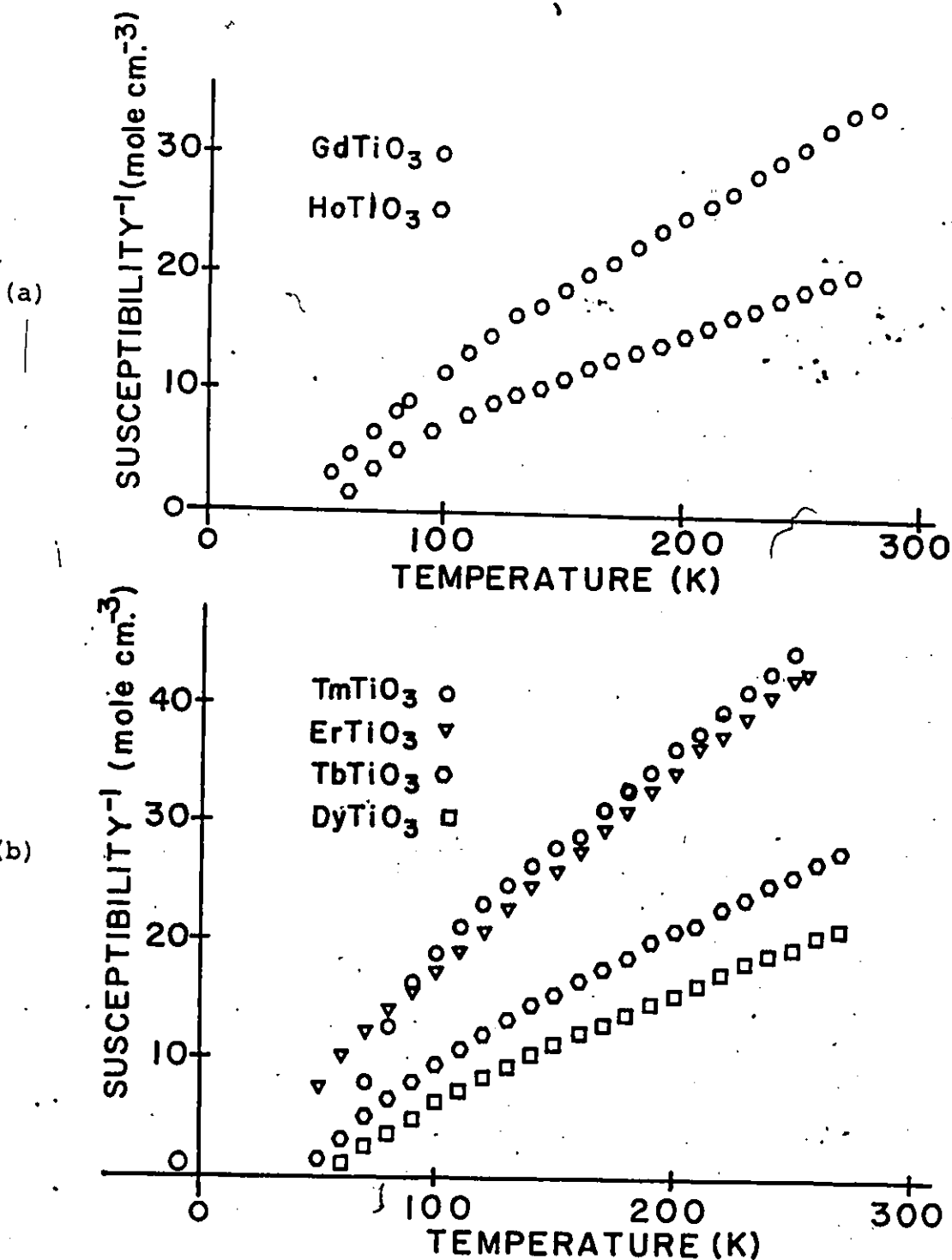


Fig. 4-3 a) Temperature dependence of the inverse susceptibility of $R\text{TiO}_3$, $R = \text{Gd}^\dagger$ and Ho
 b) Temperature dependence of the inverse susceptibility of $R\text{TiO}_3$, $R = \text{Tb}, \text{Dy}, \text{Er}$ and Tm .

[†]Goral and Greedan, 1982.

* smaller titanium moment. An antiparallel arrangement of two different magnetic moments results in a rapid change in $\frac{1}{X}$ near T_c which is not observed in ferromagnets or antiferromagnets. Ferrimagnetism is also observed in systems where the same magnetic ion resides on two different crystallographic sites which may have different occupation numbers. The concept of ferrimagnetism has been expanded to include systems with more than two magnetic sublattices as well as to spiral or triangular spin configurations (Morrish, 1965).

Deviations from linearity for the temperature dependence of X^{-1} have been observed in systems where the crystal field splittings are large compared to kT (Mabbs and Mackin, 1973). However, this is not believed to be the source of the nonlinear $X^{-1} - T$ curves observed for the heavy rare earth-titanium oxides. The temperature dependence of the reciprocal susceptibility of $GdTiO_3$ is also hyperbolic in shape (Goral and Greedan, 1982). $Gd^{3+}(4f^7)$ has an $^8S_{7/2}$ ground state. With zero orbital angular momentum, this state will not be split by the crystal field and Gd^{3+} should behave as a free ion in the crystalline solid. The shape of the $X^{-1} - T$ curve for $GdTiO_3$ can therefore be attributed to ferrimagnetic ordering of the gadolinium and titanium moments. Further evidence that the gadolinium moments are coupled antiparallel to the titanium moments comes from the saturation magnetization of $5.9 \mu_B$ per formula unit for $GdTiO_3$ (Goral and Greedan, 1982). If Gd^{3+}

and Ti^{3+} are contributing their free ion moments of $7.0 \mu_B$ and $1.0 \mu_B$ respectively, then it follows that the gadolinium and titanium moments are coupled antiparallel to one another.

The susceptibility data shown in Figure 4-3 were analyzed by applying molecular field theory to a two-sublattice model. The $X^{-1} - T$ curve predicted by this treatment can be expressed as:

$$X^{-1} = \frac{T-\theta}{C} - \frac{\xi}{T-\theta'} \quad (4-2)$$

The constants θ , ξ and θ' are defined as (Morrish, 1965)

$$\theta = -\frac{1}{C} (2C_{Ti}C_R\lambda_{R-Ti} - C_{Ti}^2\lambda_{Ti-Ti} - C_R^2\lambda_{R-R}) \quad (4-3)$$

$$\theta' = \frac{C_{Ti}C_R}{C} (2\lambda_{R-Ti} + \lambda_{R-R} + \lambda_{R-Ti}) \quad (4-4)$$

$$\xi = \frac{C_{Ti}C_R}{C^3} (C_{Ti}^2 (\lambda_{Ti-Ti} + \lambda_{R-Ti})^2 + C_R^2 (\lambda_{R-R} + \lambda_{R-Ti})^2 - 2C_R C_{Ti} (\lambda_{R-Ti}^2 + (\lambda_{Ti-Ti} + \lambda_{R-R})\lambda_{R-Ti} + \lambda_{R-R}\lambda_{Ti-Ti})) \quad (4-5)$$

where the Curie constant $C = C_R + C_{Ti}$ is equal to the inverse slope at high temperatures, C_{Ti} and C_R are the titanium and rare earth Curie constants respectively, and λ_{Ti-Ti} , λ_{R-Ti} and λ_{R-R} are the molecular field coupling constants. Positive and negative exchange constants imply parallel and antiparallel coupling respectively. For the above analysis the sign of λ_{R-Ti} was assumed to be negative as previously discussed for

the case of GdTiO_3 . This assumption is later substantiated by the neutron diffraction experiments. If C_{Ti} and C_{R} are re-defined as xC and $(1-x)C$ respectively, the above equations reduce to a form given by Néel for identical magnetic ions on two different sites with a fraction x on one site and $(1-x)$ on the other (Smart, 1966).

If the Curie constant for titanium is fixed at $0.36 \text{ cm}^3/\text{mole deg.}$ as measured for YTiO_3 (Johnson, 1975), equations (4-3), (4-4) and (4-5) can be solved for $\lambda_{\text{Ti-Ti}}$, $\lambda_{\text{R-Ti}}$ and $\lambda_{\text{R-R}}$. The results for TbTiO_3 through to TmTiO_3 are shown in table 4-1 along with the values of C , θ , θ' and ξ . The relative magnitude of the coupling constants - $\lambda_{\text{Ti-Ti}} > \lambda_{\text{R-Ti}} > \lambda_{\text{R-R}}$ are as expected from the spatial extension of the 4f and 3d wavefunctions. We do not attach any significance to the variation in the exchange constants across the series and there is no correlation between the exchange constants and the critical temperatures.

An independent determination of $\lambda_{\text{Ti-Ti}}$ is possible by fitting the temperature dependence of the magnetic susceptibility of the ferromagnet YTiO_3 to the Curie-Weiss law:

$$x = \frac{C}{T-\theta} \quad (4-6)$$

$\lambda_{\text{Ti-Ti}}$ is simply related to the Weiss constant θ by (Smart, 1966)

Table 4-1

Curve fitting parameters derived from the high temperature susceptibilities of RTiO_3 , R = Gd-Tm

RTiO_3	C_{exp} ($\text{cm}^3/\text{deg}/\text{mole}$)	C_{theor} ($\text{cm}^3/\text{deg}/\text{mole}$)	θ (K)	ξ ($\frac{\text{mole deg}}{\text{cm}^3}$)	θ' (K)	$\lambda_{\text{Ti-Ti}}$ ($\frac{\text{mole}}{\text{cm}^3}$)	$\lambda_{\text{R-Ti}}$ ($\frac{\text{mole}}{\text{cm}^3}$)	$\lambda_{\text{R-R}}$ ($\frac{\text{mole}}{\text{cm}^3}$)
GdTiO_3 (a)	7.9(1)	8.25	-13(5)	140(40)	30(5)	40.6	-23.8	.3
TbTiO_3	9.69(8)	12.19	-1(2)	40(4)	48(2)	122	-15	.9
DyTiO_3	11.9(1)	14.54	16(1)	36(4)	52(2)	122	-13	2
HoTiO_3	13.40(4)	14.44	-5.4(7)	26(3)	51(1)	126	-13	0
ErTiO_3	6.1(4)	11.85	-9(1)	18(2)	40(1)	90	-14	-2
TmTiO_3	6.1	7.52	-19.6(7)	55(7)	59(1)	142	-24	-1
YTiO_3 (b)	.36	.37	33	-	-	93	-	-

(a) (Goral and Greedan, 1982)

(b) (Johnson, 1975)

$$\lambda_{\text{Ti-Ti}} = \frac{3k\Theta}{Ng^2\mu_B^2S(S+1)}, \quad (4-7)$$

where k is the Boltzmann constant and μ_B is the Bohr magneton. If X is taken to be the molar susceptibility, N is Avogadro's number. The Weiss constant for YTiO_3 has been reported to be 33K (Johnson, 1975), which gives a value of 93 mole/cm³ for $\lambda_{\text{Ti-Ti}}$ that is in reasonable agreement with the values in table 4-1.

Mean field theory neglects short range order. Therefore, it gives erroneous results in the vicinity of the critical temperature. However, it is instructive to compare the critical temperature calculated from paramagnetic data T_p , with the critical temperature determined from data taken in the magnetically ordered regime. For a simple ferromagnet, mean field theory predicts $T_c = T_p = \Theta$ (Smart, 1966), while for the two sublattice ferrimagnet (Morrish, 1965),

$$T_c = T_p = \frac{1}{2} (\lambda_{aa}C_a + \lambda_{bb}C_b) + \frac{1}{2} \sqrt{(\lambda_{aa}C_a + \lambda_{bb}C_b)^2 - 4(\lambda_{aa}\lambda_{bb}C_aC_b - C_aC_b^2\lambda_{ab})}. \quad (4-8)$$

Table 4-2 shows a comparison of the critical temperatures T_c and T_p . T_p tends to be larger than T_c in most cases.

The field dependence of the sample magnetization at 4.2K is shown in figure 4-4 for fields up to 15 kilogauss and in figure 4-5 for fields up to 60 kilogauss. The data were ob-

Table 4-2

Critical temperatures determined from the temperature dependence of the spontaneous magnetization (T_c) and the paramagnetic susceptibility (T_p)

$RTiO_3$	T_c	T_p
TbTiO ₃	48	58
DyTiO ₃	64	61
HoTiO ₃	55	58
ErTiO ₃	40	42
TmTiO ₃	57	67
YTiO ₃	29	33

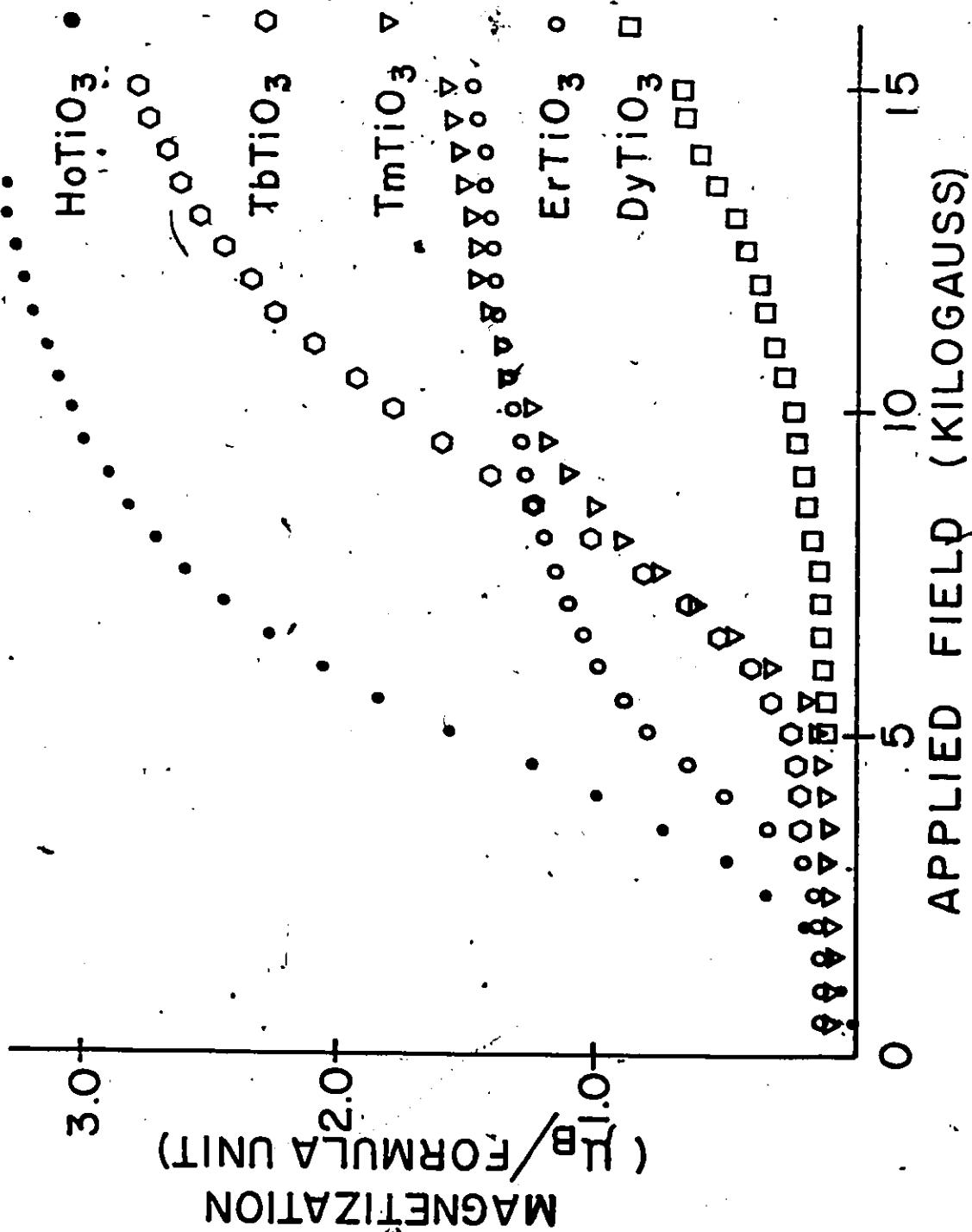


Fig. 4-4 Field dependence of the isothermal (4.2K) magnetization for $R\text{TiO}_3$,
 R = Tb-Tm and fields ranging from 0 + 15 kilogauss.

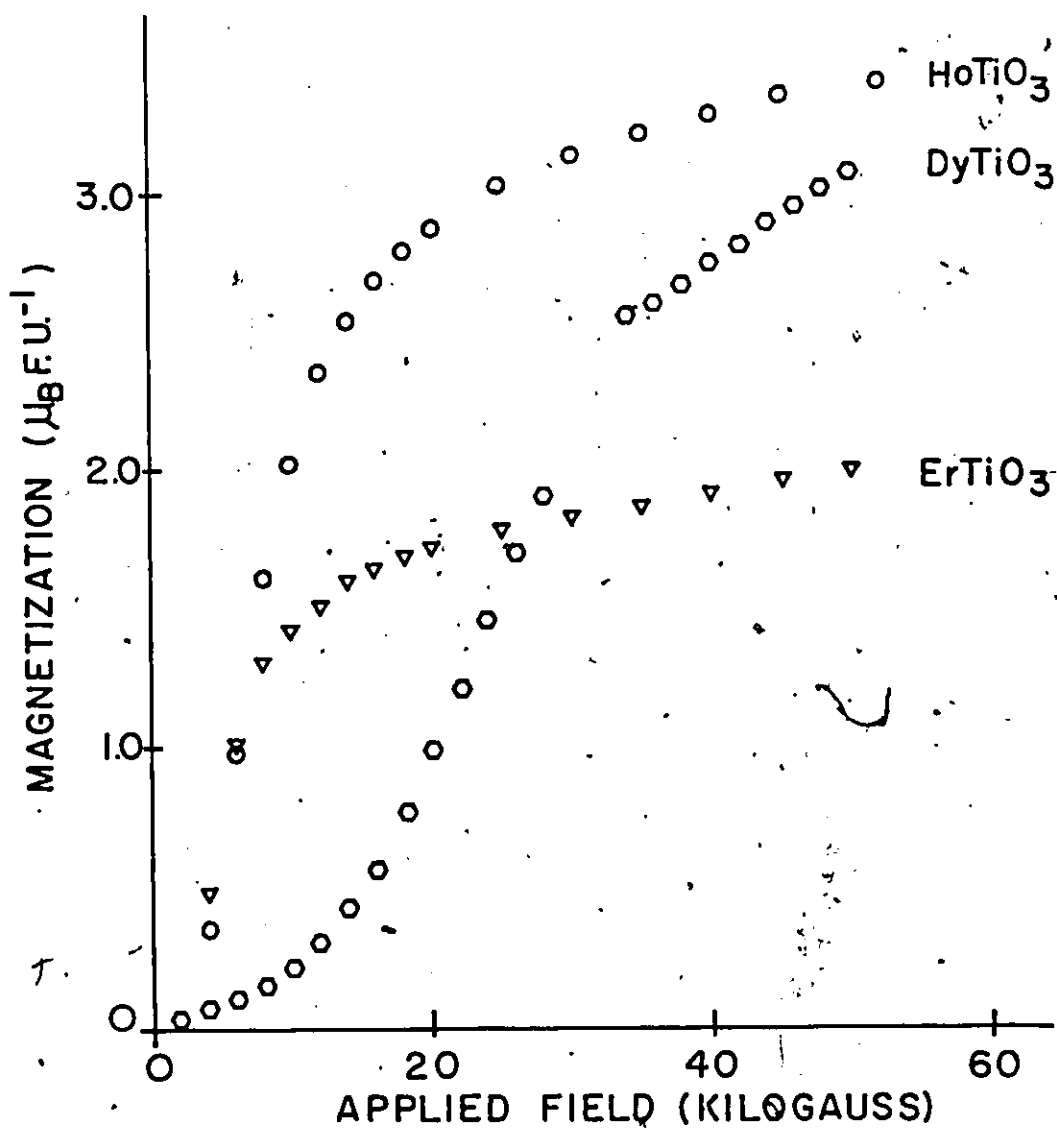


Fig. 4-5 Field dependence of the isothermal (4.2K) magnetization for RTiO_3 , $R = \text{Dy, Ho and Er}$ and fields ranging from 0 to 60 kilogauss.

tained for polycrystalline samples. The free energy of a ferromagnetic or ferrimagnetic material is given by (Morrish, 1965)

$$F_T = F_H + F_M + F_{EX} + F_{AN} + F_S + F_0 \quad (4-9)$$

F_H is the energy of the magnetization M in an external magnetic field H and is written as

$$F_H = \int_{\text{vol.}} M \cdot H dv \quad (4-10)$$

F_M is the energy of the magnetization in its own demagnetizing field H_M such that

$$F_M = \frac{1}{2} \int_{\text{vol.}} M \cdot H_M dv \quad (4-11)$$

The next term is the exchange energy. It can be written most generally as (Bertaut, 1963)

$$F_{EX} = \langle -2 \sum_{i,j} \bar{J}_i \cdot \bar{A}_{ij} \cdot \bar{J}_j \rangle \quad (4-12)$$

where A is a second rank Cartesian tensor for the coupling between the i^{th} and j^{th} ions and J_i is the total angular momentum of the i^{th} ion in the lattice.

F_{AN} is the magnetocrystalline anisotropy energy which is the energy necessary to rotate the magnetization away from the easy direction. For an orthorhombic system the anisotropic energy

to lowest order in the direction cosines has the form (Zijlstra, 1967)

$$F_{AN} = k_1 \cos^2 \alpha_1 + k_2 \cos^2 \alpha_2 + k_3 \cos^2 \alpha_3, \quad (4-13)$$

where α_1 , α_2 and α_3 are angles which give the orientation of the magnetization vector relative to the crystallographic axes. F_S is the free energy of magnetostriction, which is a strain energy produced in the crystal lattice by the ordering of the magnetic moments. F_0 represents all other sources of the free energy in the solid state that are not related to magnetic ordering. In zero applied field and at temperatures below the critical temperature, the magnetic moments form a domain structure that will minimize the total free energy. The process of magnetizing a sample to saturation involves applying a large enough external magnetic field so that the contribution from this term to the total free energy dominates all of the others.

There are two striking features about the curves in figures 4-4 and 4-5. Notice in figure 4-4 how the magnetization remains negligibly small until the field reaches 3 to 5 kilogauss at which point it rises abruptly to a new level. Also, the magnetization is much smaller than expected from the free ion magnetic moments, even at fields of 60 kilogauss as figure 4-5 indicates.

The peculiar "S" shape of the magnetization curves is not readily understood without more information about the magnetic structures. Relevant discussion will be deferred until the structures and single crystal magnetic data are presented. The lack of saturation at fields up to 60 kilogauss is probably due to the domination of the contribution from the magnetocrystalline anisotropy to the total free energy. The interaction of the 4f electrons with the electrostatic crystal field is much smaller than spin orbit coupling. Consequently, the orbital angular momentum is not quenched and the magnetic moments are coupled to the crystal field through spin orbit coupling (Cullity, 1972). The preferred direction of the magnetic moments in the crystal lattice is referred to as the easy direction of magnetization. Work must be done on the system to rotate the moments away from this direction. Since, in a polycrystalline sample, the easy direction in each crystallite is oriented at some arbitrary angle with respect to the applied magnetic field, large fields are necessary to magnetize the sample to saturation if the magnetocrystalline anisotropy energy is large.

4-2 MAGNETIC STRUCTURES

The bulk magnetic measurements have provided much useful information about the magnetic properties of the heavy rare earth orthotitanites. However, there are some questions for which the data cannot provide answers. Are the rare earth and

titanium moments coupled antiparallel to one another as in GdTiO_3 ? Is the shape of the M-H curve due to a reorientation of the magnetic moments as a function of the applied field? What are the magnitudes of the rare earth and titanium moments? These questions can be answered from a detailed knowledge of the magnetic structures which are determined using neutron diffraction techniques.

General Procedure

With unpolarized neutrons, the Bragg scattering below the critical temperature is the sum of the intensities due to nuclear and magnetic scattering. In order to determine the magnetic structure, the magnetic scattering intensity must be separated from the total scattering intensity. This is achieved by subtracting the scattering intensity measured above the critical temperature from the scattering intensity measured at a temperature sufficiently below T_c such that the sublattice magnetizations will be close to saturation. The difference will be the magnetic scattering provided that the crystal structure has not changed.

Quantitative information, such as the size of the magnetic moments, can be determined from the magnetic diffraction intensities after they have been normalized to account for sample size, counting time, incident neutron flux, etc. A detailed knowledge of the chemical structure is required such that the observed nuclear intensities can be fitted to calcu-

lated intensities with a scale factor as the only parameter. The scale factor is used to normalize the magnetic intensities. This procedure is outlined in the following section. Recently, Rietveld (1967) has introduced a profile analysis for neutron data obtained from polycrystals that is capable of refining both nuclear and magnetic structures but it requires a knowledge of the space group.

Nuclear Scattering: $T > T_c$

The X-ray analysis of the materials is consistent with the $GdFeO_3$ structure as discussed in chapter 2. Atomic positional parameters are obtained by extrapolation from those determined for the series $RTiO_3$, $R = La, Nd, Sm, Gd$ and Y (MacLean, Ng and Greedan, 1979) and are shown in table 4-3. The parameter used was the volume of the rare earth ion. The nuclear scattering intensities were calculated from these atomic positions and nuclear scattering lengths recorded in the literature (Bacon, 1975). They are in good agreement with the experimental nuclear intensities.

The scattering intensities for flat and cylindrical polycrystalline samples are given by

$$\text{Flat: } I = \frac{c e^{-\mu t \sec \theta} m F_{hkl}^2 e^{-2W}}{\sin^2(2\theta)} \quad (4-14)$$

where c = scale factor

μ = linear absorption coefficient (Bacon, 1975)

Table 4-3

Positional parameters for RTiO_3 , R = Tb-Yb

	Positional Parameter	Tb	Dy	Ho	Er	Tm	Yb
R	x	-0.0190	-0.0205	-0.0230	-0.0240	-0.0255	-0.0265
	y	0.0696	0.0730	0.0760	0.0780	0.0805	0.0820
	z	0.2500	0.2500	0.2500	0.2500	0.2500	0.2500
Ti	x	0.000	0.000	0.000	0.000	0.000	0.000
	y	0.500	0.500	0.500	0.500	0.500	0.500
	z	0.000	0.000	0.000	0.000	0.000	0.000
O(1)	x	0.1095	0.1165	0.1220	0.1240	0.1288	0.1316
	y	0.4668	0.4615	0.4570	0.4550	0.4516	0.4500
	z	0.2500	0.2500	0.2500	0.2500	0.2500	0.2500
O(2)	x	0.6942	0.6918	0.6900	0.6880	0.6860	0.6850
	y	0.3063	0.3083	0.3100	0.3110	0.3130	0.3145
	z	0.0541	0.0565	0.0580	0.0590	0.0603	0.0613

t = sample thickness

m = multiplicity of (hkl) reflection

F_{hkl} = structure factor amplitude per unit cell

W = Debye-Waller factor $(\frac{B \sin^2 \theta}{\lambda^2})$

2θ = scattering angle .

$$\text{Cylindrical: } I = \frac{cmF_{hkl}^2 e^{-2W} A_{hkl}}{\sin\theta \sin 2\theta} \quad (4-15)$$

where

A_{hkl} = absorption factor . (Bacon, 1975)

The nuclear intensities for HoTiO_3 and ErTiO_3 were measured at room temperature. The samples were maintained in a flat geometry and the sample thickness was chosen such that $\mu t \approx 1$. The coefficients B in the Debye-Waller factor were estimated from X-ray data (MacLean, Ng and Greedan, 1979). Since these materials have high melting points ($\approx 2000^\circ\text{C}$), the thermal amplitudes of vibration are small at room temperature. Consequently, they account for only a small ($\approx 9\%$) decrease in diffraction intensity over the angular range studied. For TbTiO_3 and TmTiO_3 , nuclear intensities were collected at 100K and the Debye-Waller effect was neglected. The materials were maintained in a cylindrical geometry. The absorption factor, A_{hkl} , which is a slowly increasing function of scattering angle, was set equal to a constant. This is a sufficient approximation for the samples and the angular range used. The nuclear intensities for DyTiO_3 , which was maintained in a flat

Table 4-4

Comparison of observed and calculated nuclear scattering intensities for TbTiO_3 . $R'' = 5.9\%$

h k l	I_{obs}	I_{calc}
1 1 0	803±38	854
0 0 2		
1 1 1	134±22	133
2 0 2	1005±44	1080
2 2 0	830±56	828
0 0 4		
0 2 3		
2 2 1		
1 2 3	83±8	57
1 3 0		
2 1 3	1004±50	918
3 0 1		
1 3 1		
2 2 2		
1 1 4		
3 1 0		
3 1 1	94±20	108
2 0 4	199±20	246
3 1 2		
2 2 3		
2 3 0	142±15	125
2 3 1		
3 2 0		
1 2 4	304±17	306
1 0 5		
3 0 3		
1 3 3	241±19	245
1 4 0		
2 2 4		

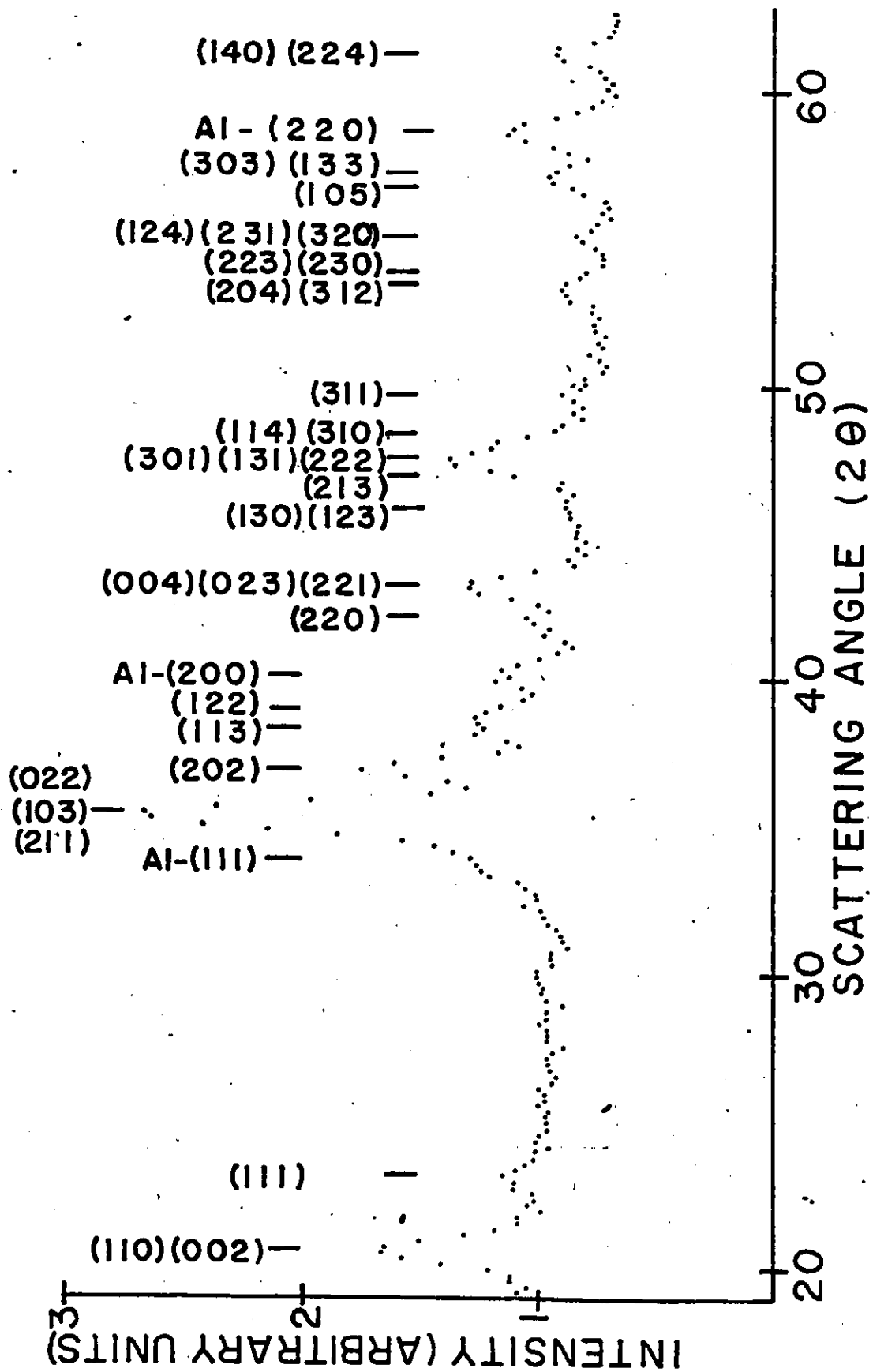


Fig. 4-6 Angular dependence of the neutron scattering intensity for TbTiO_3 at 100 K.

geometry, were also collected at 100K. The sample thickness was chosen such that $\mu t \approx 1$.

Table 4-4 shows a comparison of observed and calculated nuclear intensities for TbTiO_3 along with the agreement factor, R " (Hamilton, 1965). Comparisons for other members of the series are shown in Appendix A. The diffraction patterns also contained reflections from aluminum that was used for the cryostat tail. Sample reflections which are overlaid by aluminum reflections are not included in the comparisons. Figure 4-6 shows data collected at 100K for TbTiO_3 . Graphs of intensity against scattering angle for $T > T_c$ for other members of the series are shown in Appendix A.

Magnetic Bragg Scattering $T < T_c$

At temperatures below the critical temperature, the magnetic moments on neighbouring sites couple and become aligned. When this occurs, the magnetic scattering from different sites appears in the form of Bragg diffraction peaks. It is possible that the nuclear structure will change at or below the critical temperature, usually due to magnetostriction. There is no evidence that this occurs with the materials under investigation. When the nuclear structure is the same below T_c , a model for the magnetic structure can be determined by indexing the magnetic diffraction peaks on the basis of the chemical cell, as discussed in section 1-7.

The form factors for the rare earth and titanium ions, which account for the interference between neutrons scattered from different regions of the unpaired electron density within

an atomic site, were obtained from the calculations of Stassis et.al. (1977) and Freeman and Watson (1961). For the refinement of the magnetic structure, only the magnitude of the titanium moment and the magnitude and direction of the rare earth moment were adjustable parameters, while the atomic positional coordinates were fixed at their room temperature values. The function minimized by the least squares refinement was Hamilton's R'' defined as (Hamilton, 1965)

$$R'' = \left[\frac{\sum_i w_i (|F_i|_o - |F_i|_c)^2}{\sum_i w_i |F_i|_o^2} \right]^{1/2}, \quad w_i = \sigma_i^{-2}, \quad (4-16)$$

where the subscripts o and c refer to observed and calculated, F_i is the square root of the i^{th} intensity and σ_i is the standard deviation of F_{i0} . The standard deviations of the adjustable parameters correspond to a doubling of χ^2 defined by (Bevington, 1969)

$$\chi^2 = \sum_i w_i (|F_i|_o - |F_i|_c)^2 \quad (4-17)$$

TbTiO₃, DyTiO₃, HoTiO₃

The magnetic structure of the three compounds above 4.2K are basically the same and so they will be discussed together. A plot of scattering intensity against scattering angle for TbTiO₃ at 10K is shown in figure 4-7 and it illustrates the essential features of the common magnetic structure. Similar plots for HoTiO₃ and DyTiO₃ are given in Appendix B.

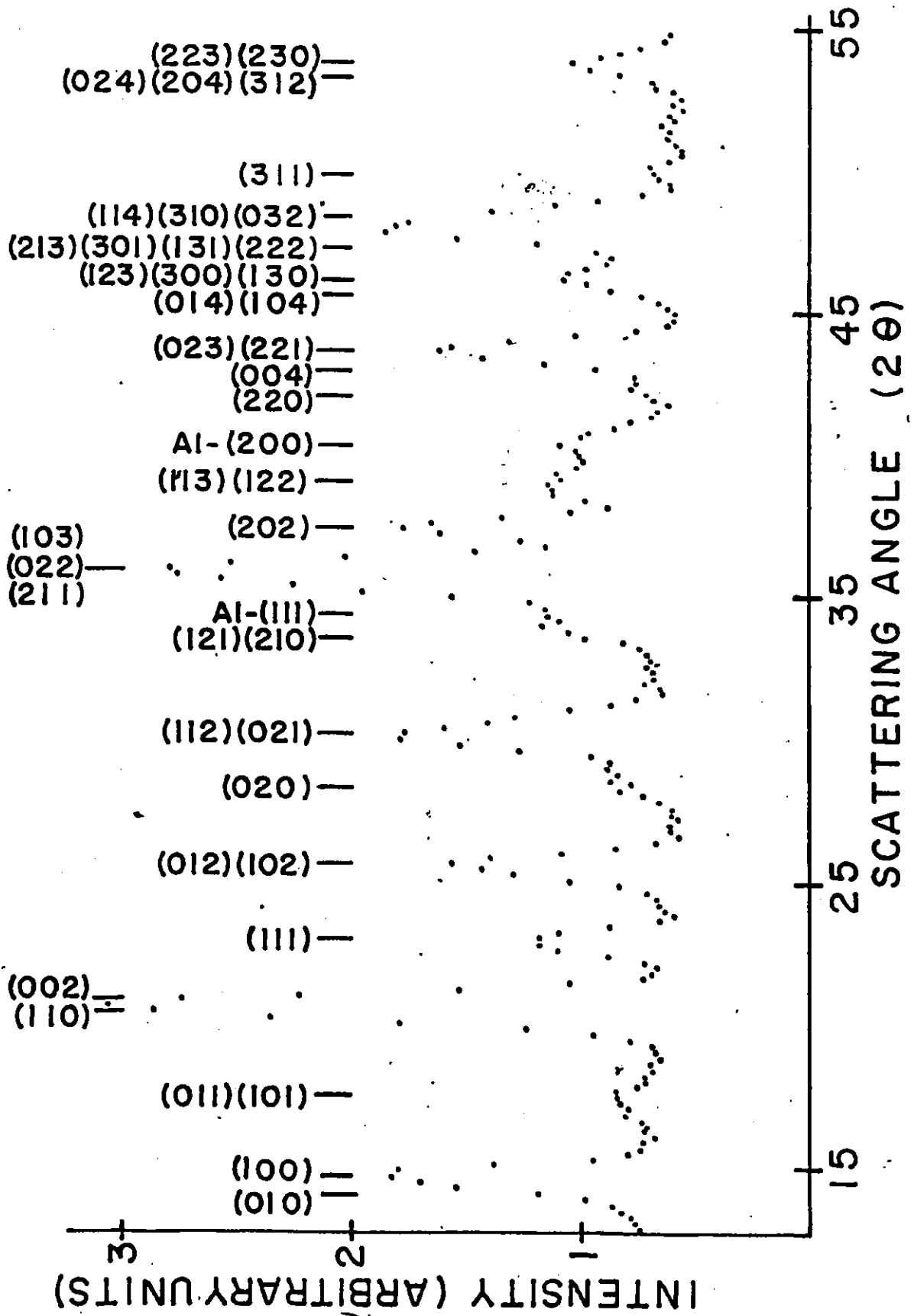


Fig. 4-7 Angular dependence of the neutron scattering intensity for TbTiO₃ at 10 K.

By comparison of figures 4-6 and 4-7, it is evident that extra Bragg scattering has developed at 10K. We attribute this to magnetic ordering on the rare earth and titanium sublattices. The magnetic scattering can be divided into two sets of reflections, one of which is coincident with the nuclear reflections. Since this set satisfies the same symmetry requirements as the nuclear reflections, it must arise from a ferro or ferrimagnetic ordering of the magnetic moments. The second set of reflections consists of (100), (010) in the case of HoTiO_3 and DyTiO_3 , (012) and (102) which are systematically absent in the nuclear structure but which can all be indexed on the basis of the chemical cell. Therefore the magnetic and chemical unit cells are the same size. The second set of reflections corresponds to a lowering of the symmetry upon magnetic ordering, as would happen if one component of the magnetic moments was ordered antiferromagnetically. The antiferromagnetic reflections satisfy $h+k = 2n+1$, $l = 2n$ and are characteristic of C-type ordering (++--).

We must choose a model for the magnetic structure which incorporates magnetic moments with both ferromagnetic and antiferromagnetic components. The largest antiferromagnetic and ferromagnetic reflections are the same order of magnitude as the nuclear reflections. The magnetic moment of Ti^{3+} cannot be larger than $1 \mu_B$ and is too small to give magnetic scattering intensity of the magnitude observed. However, the rare earth

moments can be as large as $10 \mu_B$ and are capable of producing a magnetic scattering intensity which is comparable with the nuclear scattering intensity. Thus, the rare earth magnetic moment must have both ferromagnetic and antiferromagnetic components. The titanium moment was put in a ferromagnetic array only, since $YTiO_3$ is a ferromagnet (Greedan and MacLean, 1978; Johnson, 1975).

The (010) antiferromagnetic reflection is absent in the $TbTiO_3$ data which indicates that the antiferromagnetic component of the terbium moments lies along the crystallographic b axis. Therefore, the components along the crystallographic a and c axes must be ferromagnetic. The ferromagnetic (002) reflection appears to make a significant contribution to the intensity at $2\theta = 21^\circ$ (see figure 4-7) from which we conclude that the ferromagnetic component is along the a axis.

Three refinements were tried with the titanium moments along each of the crystallographic axes. The terbium moments had an antiferromagnetic component in a C-type (++--) array along the b axis and ferromagnetic components in the ac plane. The best fit was obtained with the titanium moments along the a axis. The titanium moment refined to $-0.5 \pm 0.5 \mu_B$; the negative sign indicates that the titanium moment is antiparallel to the ferromagnetic component of the terbium moment along a. The terbium moment refined to $8.1 \pm 4 \mu_B$ at an angle of $35^\circ \pm 3^\circ$ with the a axis. The value of R'' was 5.2%. The terbium moment also

Table 4-5


Comparison of observed and calculated magnetic scattering intensities for TbTiO_3 , $R^w = 5.2\%$

h k l	I_{obs}	I_{calc}
1 0 0	1789±53	1682
1 0 1	241±41	173
0 1 1		
1 1 0	3010±75	3023
0 0 2		
1 1 1	547±41	640
0 1 2	1419±39	1543
1 0 2		
0 2 0	273±30	248
1 1 2	2117±72	2075
0 2 1		
1 2 1	237±64	498
2 1 0		
0 1 3	805±230	674
2 1 1		
1 0 3		
0 2 2		
2 0 2	382±88	259
1 1 3	246±90	313
1 2 2		
2 2 0	661±90	638
0 0 4		
0 2 3		
2 2 1	787±45	604
0 1 4		
1 0 4		
1 2 3		
1 3 0		
3 0 0		

(continued next page)

Table 4-5 (continued)

h k l	I _{obs}	I _{calc}
2 1 3		
3 0 1		
1 3 1		
2 2 2	1395±83	1278
1 1 4		
3 1 0		
0 3 2		
3 1 1	10±30	67
0 2 4		
2 0 4		
3 1 2	373±36	458
2 2 3		
2 3 0		



had a small component ($< 0.5 \mu_B$) along the c-axis but uncertainties in the data which result from the overlap of many reflections do not permit it to be stated with confidence that the c component exists. A comparison of the observed and calculated magnetic intensities for the best fit is shown in table 4-5.

Figure 4-8 shows a projection of the terbium and titanium moments in the ab plane. The titanium moments are in an F(++++) array along the a axis and the terbium moments have components in F(++++) and C(++--) arrays along the a and b axes respectively. The titanium moments are shown antiparallel to the ferromagnetic component of the terbium moments.

Similar sets of ferromagnetic and antiferromagnetic reflections were observed for HoTiO_3 and DyTiO_3 at 4.2K and 10K respectively. In these cases, the (100) and (020) reflections were absent, which indicates an antiferromagnetic component along the a axis and a ferromagnetic component along the b axis. The best fit was for the titanium moments colinear with the ferromagnetic component of the rare earth moments. Once again, the refinement gave a ferromagnetic component of the rare earth moment along the c axis but the data were not sufficient to confirm its existence. If there was a component along the c axis, it would contribute to the intensity of the (020) reflection. Since the structure factor for the (020) reflection is so small, it is impossible to surmise from the absence of the reflection

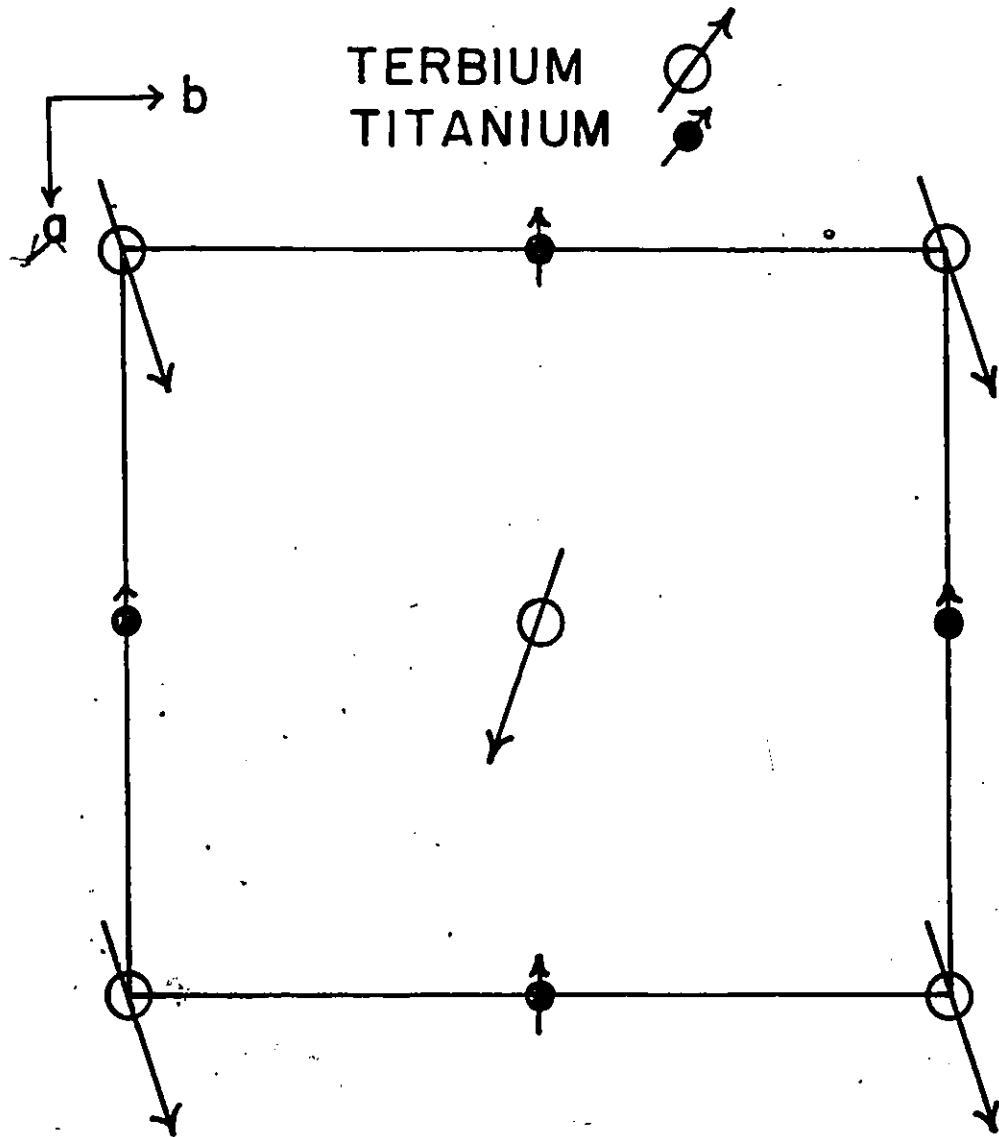


Fig. 4-8 Terbiium and titanium moment directions in the magnetic unit cell.

Table 4-6

Results of the magnetic structure refinements for $R\text{TiO}_3$, $R = \text{Tb-Tm}$

$R\text{TiO}_3$	Titanium Moment		Rare Earth Moment		R ["]
	Magnitude μ_B	Configuration	Magnitude μ_B	Configuration	
TbTiO_3	-0.5 ± 0.5	F_x	$8.1 \pm .4$	$F_x C_y$ (36 ± 3)° from [100]	5.2%
DyTiO_3	-0.9 ± 0.5	F_y	$9.7 \pm .7$	$C_x F_y$ (31 ± 5)° from [010]	7.7%
HoTiO_3	-0.8 ± 0.5	F_y	$8.3 \pm .5$	$C_x F_y$ (25 ± 3)° from [010]	4.3%
ErTiO_3	-0.7 ± 0.5	F_z	$8.5 \pm .5$	F_z	4.1%
TmTiO_3	-0.7 ± 0.5	F_z	$6.4 \pm .4$	F_z	4.2%

whether or not the rare earth moments have a c component.

The observed and calculated magnetic intensities for DyTiO_3 and HoTiO_3 for the best fit are given in Appendix B. The results of the refinements for DyTiO_3 and HoTiO_3 are shown in table 4-6.

ErTiO_3 , TmTiO_3

The magnetic structures of TmTiO_3 and ErTiO_3 are identical and thus the following analysis applies to both materials. Figure 4-9 shows the total scattering intensity for TmTiO_3 at 10K. Comparison with the scattering intensity at 100K, shown in Appendix A, indicates that extra Bragg scattering has developed at 10K. This is attributed to magnetic ordering of the thulium and titanium sublattices. All of the magnetic reflections are coincident with nuclear reflections which means that there has not been a reduction in symmetry with the onset of magnetic ordering. Therefore, the thulium and titanium moments form a strictly ferro or ferrimagnetic array with no anti-ferromagnetic component. The magnetic intensity at $2\theta = 21^\circ$ does not appear to have a contribution from the (002) reflection and so we expect that the moments are along the c axis. The data were refined using a model in which the thulium and titanium moments were in ferromagnetic arrays and colinear with one another. Table 4-7 shows the observed and calculated magnetic intensities for TmTiO_3 . Data for ErTiO_3 are shown in Appendix B. The results of the refinements for both compounds are given in table 4-6.

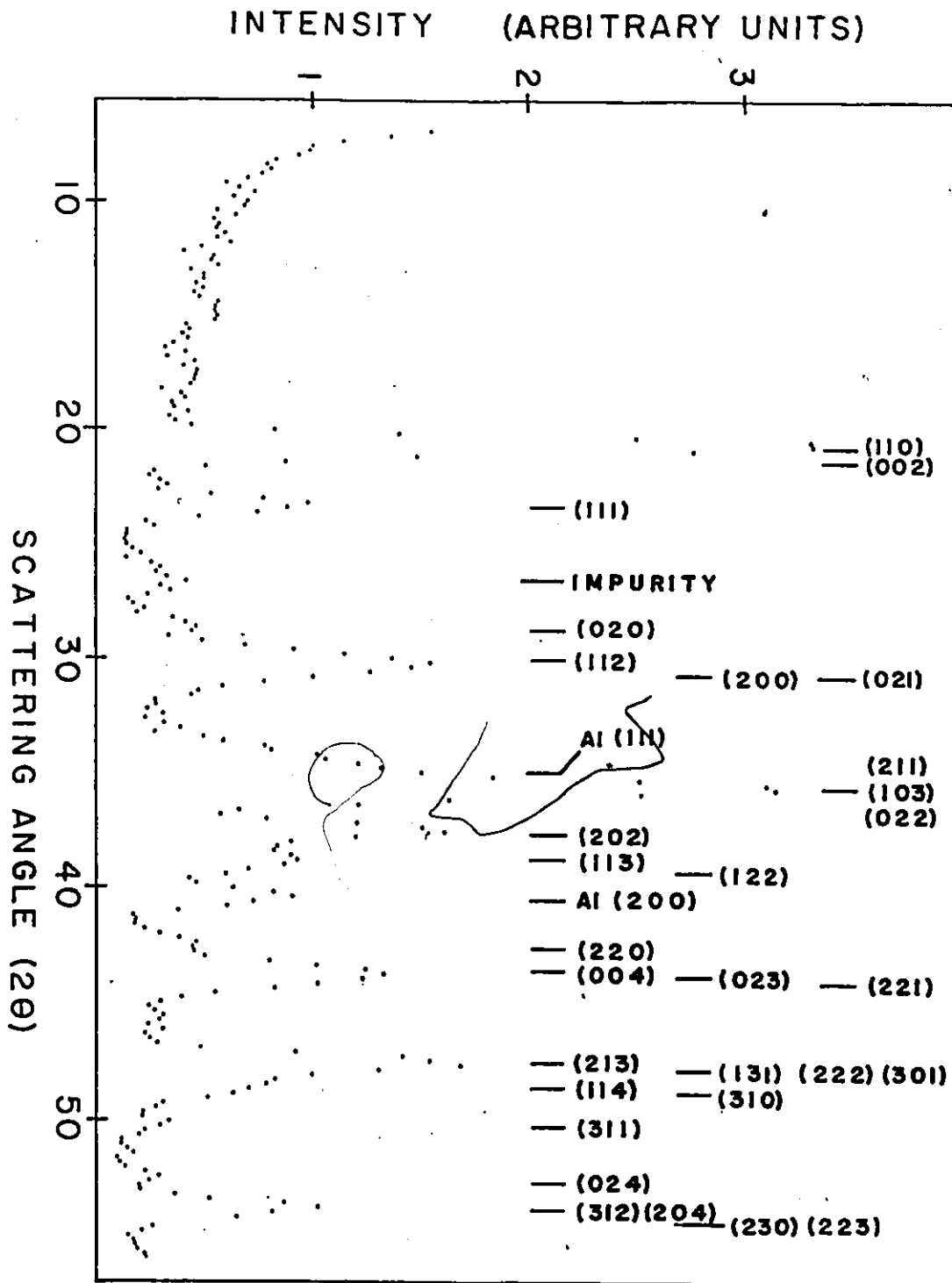


Fig. 4-9 Angular dependence of the neutron scattering intensity for $TmTiO_3$ at 10 K.

Table 4-7

Comparison of observed and calculated magnetic scattering intensities for TmTiO_3 . $R'' = 4.2\%$

h k l	I_{obs}	I_{calc}
1 1 0	2388±68	2342
0 0 2	34±34	42
1 1 1	592±34	713
0 2 0	231±34	123
1 1 2	1724±85	1750
2 0 0		
0 2 1		
2 1 1	298±144	276
1 0 3		
0 2 2		
2 0 2	400±61	446
1 1 3	98±47	102
1 2 2		
2 2 0	797±124	760
0 0 4		
0 2 3		
2 2 1	1473±102	1214
2 1 3		
3 0 1		
1 3 1		
2 2 2		
1 1 4		
3 1 0		

(Continued next page)

Table 4-7 (continued)

h k l	I _{obs}	I _{calc}
3 1 1	102±41	101
0 2 4	15±34	20
2 0 4		
3 1 2		
2 2 3	483±56	495
2 3 0		

There are several important conclusions that can be drawn from table 4-6. Although no titanium moment is more than two standard deviations in magnitude, the average value from the five structures is $.7 \pm .2 \mu_B$, which compares well with its value of $.84 \mu_B$ in $YTiO_3$ (Garrett, Greedan and MacLean, 1981). The titanium moment is consistently negative which indicates an antiparallel coupling between it and the ferromagnetic component of the rare earth moment. This confirms the assumption of antiparallel coupling between the rare earth and titanium moments that was made for the analysis of the paramagnetic susceptibility data. A comparison of table 4-6 with table 1-2 shows that the configurations of the titanium and rare earth moments belong to identical irreducible representations. Within the approximation of a bilinear Hamiltonian, this must be the case if the titanium and rare earth moments are to couple together (Bertaut, 1963). It was argued in section 1-4 that the rare earth sublattice undergoes magnetic ordering at the same critical temperature as the titanium sublattice due to the non-zero isotropic coupling between the rare earth and titanium ions. The magnetic structures determined by neutron diffraction have confirmed that the magnetic moments adopt configurations for which the coupling is allowed by symmetry.

For $TbTiO_3$, $DyTiO_3$ and $HoTiO_3$, the refinements of the data were inconclusive with respect to the existence of a c component for the rare earth moment. However, according to table 1-2, it would belong to an irreducible representation which

would not couple to either the $\Gamma_2(+++)$ or $\Gamma_3(-++)$ irreducible representation within the approximation of a bilinear Hamiltonian. It could couple via a higher order Hamiltonian but the resulting interaction would be weaker than the bilinear term. Therefore, the z component would not be expected to couple at the same critical temperature as the components coupled by the bilinear term. There is no evidence of more than one critical temperature in the temperature dependence of either the bulk magnetization or the magnetic scattering intensity (to be discussed in section 4-4). Thus, it is unlikely that the rare earth moment has a z component.

Neutron diffraction patterns were measured at 10K and 100K for YbTiO_3 as well. The differences between the two diffraction patterns were very small. The weak ferrimagnetic lines which were observed could all be indexed on the basis of the chemical cell and there was no evidence for any antiferromagnetic reflections. Powder patterns for YbTiO_3 at 100K and 10K are given in Appendices A and B respectively.

Only one magnetic peak was intense enough to allow a statistically significant determination of the ytterbium moment. It occurs at a scattering angle of 21° and arises from a combination of the (110) and (002) reflections. If the ytterbium moments lie along the crystallographic c-axis as do the erbium and thulium moments, then the (002) magnetic reflection will be absent and the magnetic intensity at $2\theta = 21^\circ$

will be due entirely to the (110) reflection. In this case, the ytterbium moment is found to be $1.7 \pm 0.2 \mu_B$. For the calculation the titanium moment was fixed at $.84 \mu_B$ (Garrett et. al. 1981); antiparallel to the rare earth moment. The ytterbium moments could also lie in the ab plane like the terbium, dysprosium and holmium moments. Then, both the (110) and (002) reflections will be present. The contribution from the (110) reflection will be zero if the ytterbium moments lie along [110] and will increase to a maximum if the moments lie along the crystallographic a or b axes. Once again, the titanium moments are assumed to be $.84 \mu_B$; antiparallel to the rare earth moment. For this model, the magnitude of the ytterbium moment ranges from $2.0 \pm 0.2 \mu_B$ up to $2.4 \pm 0.2 \mu_B$, depending on the contribution from (110). The ytterbium moment of $1.7 \pm 0.2 \mu_B$ determined for the moments parallel to the c axis is identical to the value found in $\text{Yb}_2\text{V}_2\text{O}_7$ by Solderholm, et.al. (1980).

It is instructive to compare the magnitudes and directions of the rare earth moments in RTiO_3 with those found in the isostructural series RMO_3 , M = Al, Fe and Cr*. Table 4-8

-
- *Goodenough and Longo, 1970
 Koehler, Wollan and Wilkinson, 1960
 Van Laar and Elemans, 1971
 Tamaki, Tsushima and Yamaguchi, 1977
 Bertaut and Mareschal, 1967a
 Bertaut, Mareschal and De Vries, 1967b
 Bertaut et. al., 1967c
 Mareschal et.al., 1968
 Bidaux and Mériel, 1968
 Herpin and Mériel, 1964
 Bielen, Mareschal and Sivardière, 1967
 Bertaut et.al., 1964
 Shamir et.al., 1981

Table 4-8

Comparison of the rare earth magnetic moments (in Bohr magnetons) found in RMO_3 , $M = \text{Cr, Fe, Al}$ and Ti with their free ion values

	Tb	Dy	Ho	Er	Tm
gJ (free ion)	9	10	10	9	7
gJ (M = Ti)	8.1±.4	9.7±.8	8.1±.5	8.5±.5 7.3±.3	6.0±.3
gJ (M = Fe)	8.6		7.5	5.8	
gJ (M = Cr)	8.6		7.8	5.2	
gJ (M = Al)	8.3	8.8			

compares the magnitudes of the rare earth moments found in each of the above series with their free ion values. With the exception of erbium, the rare earth moments are between 75% and 97% of their free ion values. The terbium and holmium moments show little variation between series, while the largest discrepancy is found for the erbium moment. The first measurement of this moment in ErTiO_3 by neutron diffraction yielded $8.5 \mu_B$ while a subsequent measurement gave $7.3 \mu_B$. Both values are somewhat larger than the erbium moment reported for ErCrO_3 and ErFeO_3 where it is only $5.2 \mu_B$ and $5.8 \mu_B$.

Table 4-9 shows the directions of the rare earth moments in the series RMO_3 , $M = \text{Fe, Cr, Al and Ti}$. It is clear from this table that the erbium and thulium moments prefer to lie along the c axis, while the terbium, dysprosium and holmium moments prefer to lie in the ab plane. The angles that the rare earth moments make with the crystallographic axes in the orthochromites, orthoferrites and orthoaluminates compare well with those found in the orthotitanites. This suggests that the interaction governing the direction of the rare earth moment is determined by the identity of the rare earth ion. Moreover, the existence of essentially identical angles in the orthoaluminates as in the other series shows that exchange with the transition metal ions is not involved in the interaction mechanism. One can also rule out the influence of rare earth-rare earth exchange as it appears to be negligibly small. Therefore, we conclude that it is the interaction between the rare earth

Table 4-9

Rare earth moment directions in RMO_3 , $M = \text{Cr, Fe, Al}$ and Ti

RMO_3	Rare Earth Moment Direction	Rare Earth Spin Configuration
DyAlO_3	ab plane, 33° to $[010]$	-
DyFeO_3	ab plane, 30° to $[010]$	-
DyCrO_3	ab plane, 29° to $[010]$	-
DyTiO_3	ab plane, 31° to $[010]$	$C_x^F Y$
TbAlO_3	ab plane, 34° to $[100]$	-
TbFeO_3	ab plane, 38° to $[100]$	$F_x^C Y$
TbCrO_3	ab plane, -	$F_x^C Y$
TbTiO_3	ab plane, 36° to $[100]$	$F_x^C Y$
HoFeO_3	ab plane, 27° to $[010]$	$F_x^C Y$
HoCrO_3	ab plane, 26° to $[010]$	$F_x^C Y$
HoTiO_3	ab plane, 24° to $[010]$	$C_x^F Y$
ErFeO_3	$[001]$	C_z
ErCrO_3	$[001]$	C_z
ErTiO_3	$[001]$	F_z
TmFeO_3	-	-
TmCrO_3	$[001]$	-
TmTiO_3	$[001]$	F_z

and the surrounding crystal field which is determining the preferred direction of the rare earth moments in these materials. As all members of the series RMO_3 , $M = \text{Al, Cr, Fe and Ti}$, $R = \text{Tb - Lu}$, are isostructural, the crystal field experienced by a heavy rare earth ion in any of the above compounds should be approximately the same.

If the rare earth moment direction is determined by the crystal field, then the preferred direction must correspond to a minimum in the magnetocrystalline anisotropy free energy. The free energy per ion can be expressed as a series expansion:

$$F_{\text{an}} = \sum_{i=1}^3 \Gamma_i \alpha_i + \sum_{i=1}^3 \sum_{j=1}^3 \Gamma_{ij} \alpha_i \alpha_j + \sum_{i=1}^3 \sum_{j=1}^3 \sum_{k=1}^3 \Gamma_{ijk} \alpha_i \alpha_j \alpha_k + \dots \quad (4-18)$$

where the α_i are the direction cosines of the magnetization with respect to some convenient set of axes and the Γ 's are property tensors (Birss, 1964). Magnetocrystalline anisotropy is a static property and is invariant with respect to time inversion. Since the magnetization reverses direction under time inversion, both orientations must have the same free energy. Therefore, terms containing odd powers of α in the above expansion must vanish. If we retain only the second order term, the anisotropy energy becomes

$$F_{\text{an}} = \sum_{i=1}^3 \sum_{j=1}^3 \Gamma_{ij} \alpha_i \alpha_j, \quad (4-19)$$

where Γ_{ij} is a symmetric second rank tensor. There exists a set of principal axes for Γ_{ij} , so it is possible to define the α_i as the direction cosines of the magnetization vector referred to these principle axes. Through transformation to the principle axis system, F_{an} can be written as

$$F_{an} = \sum_i \Gamma_{ii} \alpha_i^2 = \hat{\mu} \cdot \bar{\Gamma} \cdot \hat{\mu}, \quad (4-20)$$

where $\hat{\mu}$ is a unit vector in the direction of the magnetization. One can show that the extrema in the anisotropy energy occur when the magnetization lies along any of the principle axes, and one of these will correspond to a minimum (Zijlstra, 1967). The directions of the principle axes are determined by the site symmetry.

The symmetry at the site of the rare earth ion is a mirror plane perpendicular to the orthorhombic c axis. Therefore one principal axis must be perpendicular to the mirror plane and the remaining two axes will lie in the plane. As there is no unique direction within a mirror plane, the two principle axes can assume an arbitrary orientation with respect to the orthorhombic a and b axes. This has some important consequences.

The space group Pbnm is derived from the point group D_{2h} . The generators of the point group are three mutually orthogonal 2-fold axes of rotation which are labelled a, b and c in figure 4-10. The principal axes, x, y and z, of the tensor

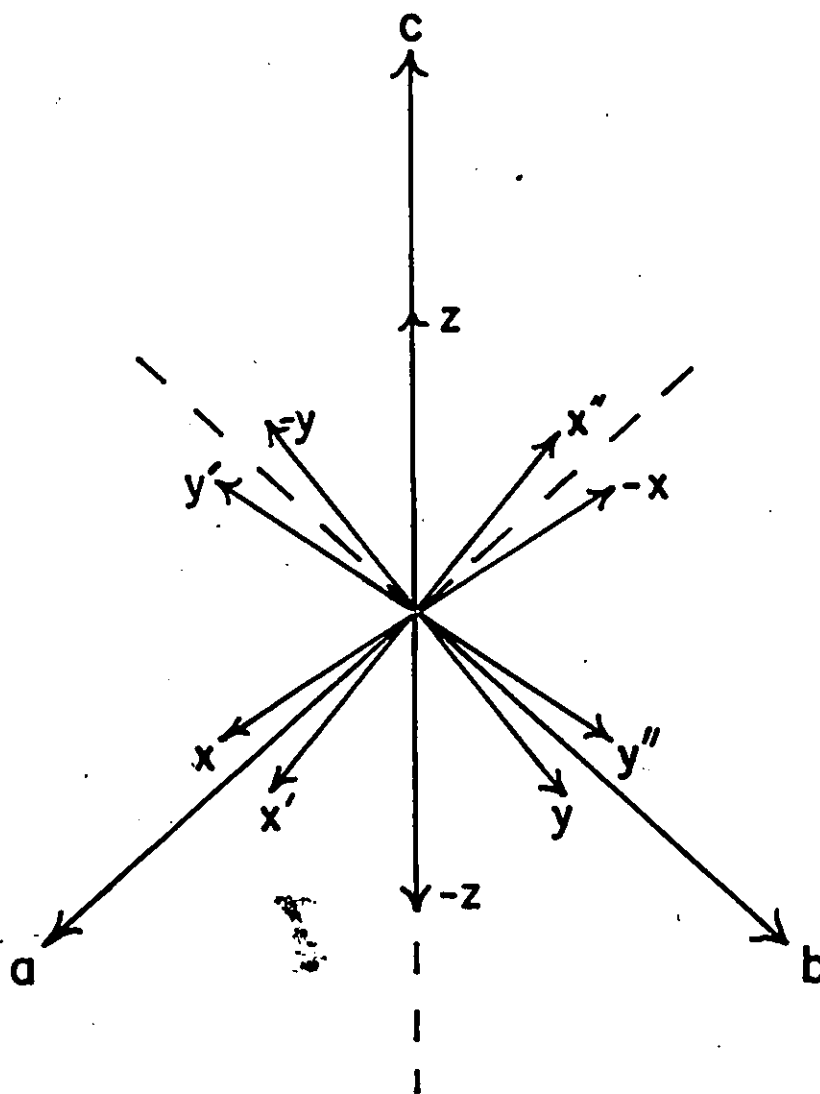


Fig. 4-10 Transformation properties of the principle axes of a second rank tensor in the point group D_{2h} . The principle axes are labelled x , y and z and the generators of D_{2h} are 2-fold axes of rotation along a , b and c .

$\bar{1}$ are also shown. The z axis is coincident with c, while x and y can assume an arbitrary orientation with respect to a and b.

Since the a axis is a two-fold axis of rotation, the axes (x,y,z) are equivalent to the set (x',y',-z). Similarly, the set (x,y,z) is equivalent to (x'',y'',-z) under a two-fold rotation about b and the sets (x,y,z) and (-x,-y,z) are equivalent due to a two-fold rotation about c. Therefore, if the rare earth moment lies along either the x or y principal axis, there are four directions in the plane which are equivalent by symmetry and must have the same energy. If the rare earth moment lies along the z principle axis, there are two equivalent directions which also must have the same energy.

The principal axes at two different rare earth sites in the unit cell are related to each other by the same transformation which takes one site to the other. Figure 4-11 shows the unit cell for the space group Pbnm with the crystallographic axes labelled a, b and c. The rare earth sites labelled (5) and (8) at $(x, y, \frac{1}{4})$ and $(\frac{1}{2} - x, \frac{1}{2} + y, \frac{1}{4})$ respectively are connected by a b glide plane located at $x = \frac{1}{4}$. Therefore, the principle axes (x_5, y_5, z_5) are transformed into $(-x_8, y_8, z_8)$ by the action of the b-glide plane.

Consider the situation where the rare earth moment lies along the principal axis labelled y. If the rare earth moments are coupled ferromagnetically then they will lie along y_5 and

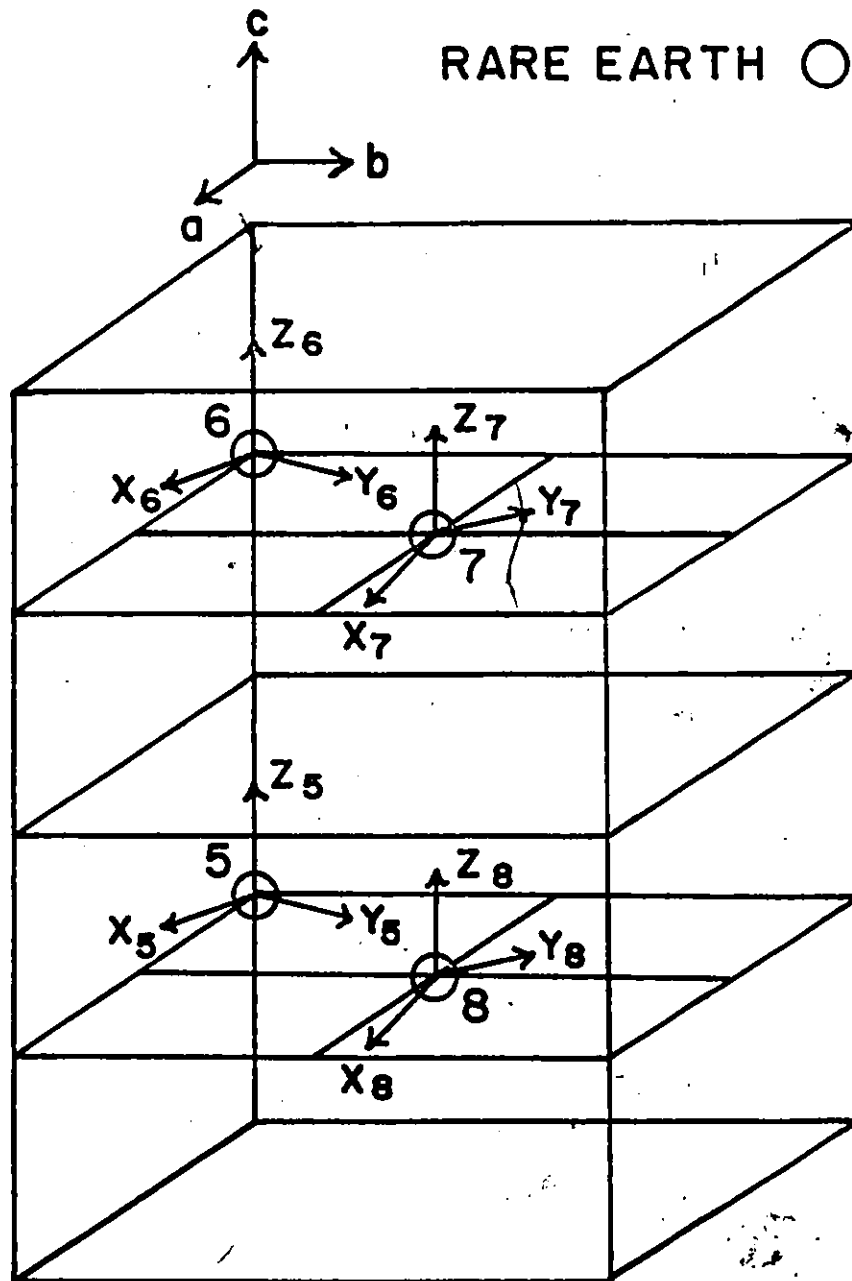


Fig. 4-11 The transformation properties of the principle axes of a second rank tensor in the space group Pbnm. Directions related by a 180° rotation are equivalent. Only the positive directions are shown.

$$\begin{aligned}
 (x_5, y_5, z_5) &\xrightarrow{\text{b-glide}} (-x_8, y_8, z_8) \\
 (x_5, y_5, z_5) &\xrightarrow{\text{n-glide}} (x_7, -y_7, z_7) \\
 (x_5, y_5, z_5) &\xrightarrow{2_1} (-x_6, -y_6, z_6)
 \end{aligned}$$

y_8 at sites (5) and (8) respectively. Thus, the rare earth moments will have ferromagnetic components along b, and antiferromagnetic components along a, as in HoTiO_3 . If the rare earth moments are coupled antiferromagnetically then they will lie along y_5 and $-y_8$ at sites (5) and (8). In this case, the ferromagnetic components will be along a and the antiferromagnetic components along b, as in HoFeO_3 and HoCrO_3 . The rare earth may also lie along the principal axis labelled z. Now, for both ferromagnetic and antiferromagnetic couplings, the rare earth moments at sites (5) and (8) will be colinear, with no antiferromagnetic components. This is observed for the erbium and thulium compounds in all of the above series. The sites labelled (6) and (7) are related to (5) by a 2 -fold screw axis and an n-glide plane respectively. Therefore, the principal axes are colinear at sites (5) and (6) and at sites (7) and (8) and the rare earth moments will be parallel at the respective sites.

Consideration of the symmetry at the rare earth site has shown that the moment can lie either parallel or perpendicular to the orthorhombic c axis. This, in turn, governs whether the rare earth moments are in a colinear or a canted array. The key to the discussion is that the rare earth moment directions are determined by the crystal field and therefore correspond to a minimum in the magnetocrystalline anisotropy energy. To determine which configuration has the lowest energy

requires a calculation which takes into account both the crystal field and the molecular field experienced by the rare earth ion. This calculation is the subject of the next section.

4-3 MAGNETIC STRUCTURE - CALCULATIONS

Crystal field calculations were briefly outlined in section 1-8 and are discussed in detail in the literature (Muchings, 1964). The perturbation Hamiltonian representing the crystal field acting on a rare earth ion at a site with only mirror symmetry is

$$H_{CF} = \sum_{k=0}^6 \sum_{q=-k}^{+k} B_q^k C_q^k, \quad k = 0, 2, 4, 6, \quad q = \pm 2, \pm 4, \pm 6 \quad (4-21)$$

where the axis of quantization is perpendicular to the mirror plane. The C_q^k are irreducible tensor operators and the B_q^k are the crystal field intensities which, although they can be calculated, are usually treated as adjustable parameters to be fitted to experimental data. The B_q^k are, in general, complex and $B_q^{k*} = (-)^q B_{-q}^k$.

A perusal of the literature disclosed three sets of crystal field intensities, B_q^k , relevant to the problem at hand and these were investigated. One set was determined by Shamir and Atzmony (1978) by fitting the crystal field energy levels of the rare earth ions in $R\text{CrO}_3$, for $R = \text{Tb}, \text{Dy}, \text{Ho}, \text{Er}, \text{Tm}$

and Yb, to the following crystal field Hamiltonian:

$$H_{CF} = H_{\text{cubic}} + H_{\text{pert}} \quad (4-22)$$

where,

$$H_{\text{cubic}} = B_0^4 (C_0^4 + \sqrt{5/14} (O_4^4 + O_{-4}^4)) \\ + B_0^6 (C_0^6 - \sqrt{7/2} (O_4^6 + O_{-4}^6))$$

and

$$H_{\text{pert}} = B_0^2 C_0^2 + B_1^2 (O_1^2 - O_{-1}^2) + B_2^2 (O_2^2 + O_{-2}^2) .$$

The authors argued that, since the orthochromite structure is an orthorhombic distortion of the cubic perovskite, the crystal field Hamiltonian could be written as a cubic term plus a perturbation which represented a distortion from cubic symmetry. In the Hamiltonian, the 4-fold axis of the cubic cell was taken as the axis of quantization.

The energy of a system is a scalar quantity, and, therefore, must be invariant under symmetry operations. The rare earth ion is located on a mirror plane. The invariance of the crystal field Hamiltonian with respect to reflection in the mirror plane requires that $k+q = 2n$, where n is an integer. The crystal field Hamiltonian that was chosen by Shamir and Atzmony contains a term for which the sum of k and q is odd. Thus, it has a lower symmetry than the rare earth site itself and is not useful for calculating the easy direction of magnetization of the rare earth ion.

A second set of crystal field intensities was determined by Karaziana, Wortman and Morrison (1976) by fitting the rare earth crystal field energy levels, for R in $YAlO_3$, to a crystal field Hamiltonian which had the correct symmetry. The crystal field intensities reported for erbium in yttrium aluminum garnet were used as starting parameters in the least squares refinement (Morrison et al., 1975). However, the fitting of a complicated function with many parameters to experimental data can have the result that the refinement depends on the choice of starting parameters. An incorrect choice of initial conditions can lead to an erroneous result. As the dependence of the crystal field intensities on the choice of starting parameters had not yet been investigated, this set of crystal field intensities was also not used.

A third set of crystal field intensities was investigated and proved to be satisfactory. It was determined by O'Hare and Donlan (1976, 1977), who fitted the polarized absorption spectra of erbium and thulium in $YAlO_3$ to a crystal field Hamiltonian with the correct symmetry. The starting parameters were carefully chosen with a technique known as descending symmetries. It is well described in the literature (Wybourne, 1965; O'Hare and Donlan, 1976) and will only be briefly outlined below.

The object of the method is to find reliable crystal field coefficients for ions on sites of low symmetry. It regards the low symmetry crystal field as being made up of

components of higher symmetry fields. The rare earth site in RTiO_3 has $C_s(m)$ symmetry. With the aid of table 4-10 the observed Stark spectrum is projected to an O_h spectrum then fitted to a crystal field Hamiltonian with cubic symmetry.

$$H_{O_h} = B_0^4(C_0^4 - \sqrt{5/14}(C_4^4 + C_{-4}^4)) + B_0^6(C_0^6 + \sqrt{7/2}(C_4^6 + C_{-4}^6)) , \quad (4-23)$$

where the quantization axes are chosen to be those of the orthorhombic unit cell. The O_h spectrum is then projected to a D_{4h} spectrum and fitted to a crystal field Hamiltonian of D_{4h} symmetry. The B_q^k 's determined in the refinement of the O_h spectrum are used as starting parameters in the D_{4h} Hamiltonian. The procedure is repeated as the D_{4h} spectrum is projected to a D_{2h} and, finally, a C_s spectrum. The crystal field Hamiltonians for D_{4h} and D_{2h} symmetry are as follows:

$$H_{D_{4h}} = B_0^2 C_0^2 + B_0^4 C_0^4 + B_4^4 (C_4^4 + C_{-4}^4) + B_0^6 C_0^6 + B_4^6 (C_4^6 + C_{-4}^6) , \quad (4-24)$$

and

$$H_{D_{2h}} = B_0^2 C_0^2 + B_0^4 C_0^4 + B_2^4 (C_2^4 + C_{-2}^4) + B_4^4 (C_4^4 + C_{-4}^4) + B_0^6 C_0^6 + B_2^6 (C_2^6 + C_{-2}^6) + B_4^6 (C_4^6 + C_{-4}^6) + B_6^6 (C_6^6 + C_{-6}^6) . \quad (4-25)$$

H_{C_s} resembles $H_{D_{2h}}$ except $B_q^k (C_q^k + C_{-q}^k)$ is replaced by $\text{Re} B_q^k (C_q^k + C_{-q}^k) + \text{Im} B_q^k (C_q^k - C_{-q}^k)$. When H_{C_s} was fitted to the C_s spectrum, the basis set was formed from all of the free

TABLE 4-10

Compatibility tables for the groups
 O_h , D_{4h} , D_{2h} and C_s (Koster et.al. 1963)

$O_h \rightarrow D_{4h}$	$D_{4h} \rightarrow D_{2h}$	$D_{2h} \rightarrow C_s$
$1\Gamma_1 \rightarrow 1\Gamma_1$	$1\Gamma_1 \rightarrow 1\Gamma_1$	$1\Gamma_1 \rightarrow 1\Gamma_1$
$1\Gamma_2 \rightarrow 1\Gamma_3$	$1\Gamma_2 \rightarrow 1\Gamma_3$	$1\Gamma_2 \rightarrow 1\Gamma_2$
$2\Gamma_3 \rightarrow 1\Gamma_1 + 1\Gamma_3$	$1\Gamma_3 \rightarrow 1\Gamma_1$	$1\Gamma_3 \rightarrow 1\Gamma_1$
$3\Gamma_4 \rightarrow 1\Gamma_2 + 2\Gamma_5$	$1\Gamma_4 \rightarrow 1\Gamma_3$	$1\Gamma_4 \rightarrow 1\Gamma_2$
$3\Gamma_5 \rightarrow 1\Gamma_4 + 2\Gamma_5$	$2\Gamma_5 \rightarrow 1\Gamma_2 + 1\Gamma_4$	

ion J multiplets, thus the crystal field calculations were fully J mixed. (O'Hare and Donlan, 1976).

When the B_q^k 's determined for erbium in $YAlO_3$ are compared with those determined for thulium in $YAlO_3$, there are some large discrepancies, even though many of the intensities compare well. O'Hare and Donlan suggest that the differences may be the result of a two-electron or higher order n-electron correlation potential (O'Hare and Donlan, 1977). The crystal field calculations described so far assume that each electron in the valence shell of the ion under consideration sees a potential which is independent of the states of the other valence electrons. A two-electron correlation potential can be introduced to describe the orbital correlation between pairs of valence electrons which is induced by the crystal field. The effect of this correlation potential is to introduce a term (LS) dependence to the B_q^k 's (Bishton and Newman, 1970). Configuration interaction also has contributions from a one-electron and two-electron correlation potential that introduces shielding (or anti-shielding) parameters which depend on the individual configurations. The parameters can depend on both k and q (linear shielding), and for some configurations, they can be different for different terms (non-linear shielding) (Rajnak and Wybourne, 1964). The neglect of the n-electron correlation potential and configuration interaction in the determination of the crystal field in-

tensities, B_q^k , ultimately limits the extent to which they can be used to calculate the magnetic properties of the rare earth ions in $RTiO_3$.

Despite the uncertainties, the B_q^k 's determined by O'Hare and Donlan (1977) for erbium in $YAlO_3$ were chosen to calculate the crystal field splittings of the ground multiplet for the rare earth ions Tb^{3+} through the Tm^{3+} in $RTiO_3$. Calculations were restricted to the ground multiplet as the excited multiplets have no appreciable population at, or below, room temperature. After the calculation of the crystal field eigenfunctions and eigenvalues, the crystal field plus molecular field were applied as simultaneous perturbations to obtain the eigenfunctions and eigenvalues of the rare earth ions in the magnetically ordered system. The molecular field was placed both parallel and perpendicular to the orthorhombic c axis.

In general, the molecular field at the rare earth site has contributions from rare earth-rare earth and rare earth-transition metal exchange. These interactions can be further subdivided into contributions from isotropic, anisotropic symmetric and antisymmetric exchange. However, table 4-9 indicates that the orientation of a given rare earth moment is independent of exchange with the transition metal ion. Therefore, a simplified model for the molecular field was used. Only isotropic coupling was considered, with the result that the rare earth magnetization must be colinear with the mole-

cular field. No attempt was made to partition the molecular field into contributions from R-R or R-Ti coupling. Instead, the molecular field at the rare earth site was represented by just one term, H_M . The energy of the rare earth moment in the field H_M , for the molecular field parallel and perpendicular to the orthorhombic c axis, is

$$H_z = - g_J \mu_B J_z H_M, \quad (4-26)$$

and

$$H_x = - g_J \mu_B J_x H_M \quad (4-27)$$

respectively. The rare earth site symmetry only defines a unique axis perpendicular to the mirror plane, thus the crystal field intensities contain no information about directions in the plane. Therefore, when H_M is placed along x it merely represents a direction perpendicular to the unique axis. Since the analysis considers only one molecular field, the magnitude of H_M was estimated from the critical temperature through molecular field theory applied to a ferromagnet. The relationship between T_c and H_M is given by (Cullity, 1972)

$$T_c = \frac{g \mu_B (J+1) H_M}{3k} \quad (4-28)$$

In this model the rare earth moment and the molecular field are colinear. Hence we conclude that the direction of H_M that gives the lowest energy will be the preferred direction for the rare earth magnetization.

In table 4-11 the results of the calculations are compared with the rare earth moment directions determined by neutron diffraction experiments. Only the energies of the ground states are tabulated. In every case, the energy of the ground state depends strongly on the direction of the molecular field. Moreover, the direction of the molecular field which gives the ground state with lower energy agrees with the direction of the rare earth moment determined by experiment. The calculations confirm that the crystal field determines whether the magnetically ordered rare earth moments lie parallel or perpendicular to the orthorhombic c axis. Presumably, the crystal field also determines the rare earth moment direction within the plane. However that information is not contained in the set of crystal field intensities which were used.

A diagonalization of the perturbation Hamiltonian, with the free ion wavefunctions forming a basis set, yields both the eigenvalues and their corresponding zeroth-order wavefunctions. The latter are linear combinations of the free ion wavefunctions, $\langle M_J \rangle$, multiplied by coefficients which are complex and dependent on the strength and symmetry of the perturbation. A typical zeroth order wavefunction may be written as

$$|\psi\rangle = \sum_{M_J=-J}^{+J} b_{M_J} |M_J\rangle \quad (4-29)$$

where J is the quantum number for the total angular momentum

Table 4-11

Energies and permanent magnetic moments of the ground states of R^{3+} in $RTiO_3$ for R^{3+} in C_s symmetry

R	E_0 (cm^{-1}) (H_{CF})	E_0 (cm^{-1}) ($H_{CF}+H_M c$)	E_0 (cm^{-1}) ($H_{CF}+H_M \perp c$)	Moment Direction (exp)	$\langle \mu \rangle^{exp}$ (μ_B)	$\langle \mu \rangle^{calc.}$ (μ_B)
Tb	-277	-279	-356	$\perp c$	$8.1 \pm .4$	8.2
Dy	-239	-293	-348	$\perp c$	$9.7 \pm .8$	9.3
Ho	-254	-304	-339	$\perp c$	$8.1 \pm .5$	8.2
Er	-263	-320	-284	$ c$	$7.9 \pm .4^*$	7.5
Tm	-338	-404	-359	$ c$	$6.0 \pm .3$	5.4

*average of two experiments

of the free ion. The complex coefficients, b_{M_J} , of the ground state wavefunctions determined from the perturbation Hamiltonians H_{CF} and $H_{CF} + H_M$ are listed in table 4-12. For the odd electron ions, only the coefficients for one member of the crystal field ground doublet are shown. The direction of the magnetic moment in the ground state of the various rare earth ions for the perturbation $H_{CF} + H_M$ can be determined by inspection of the coefficients. For example, the ground state of the thulium ion is composed mostly of $|M_J = 6\rangle$ while that of the erbium ion is largely $|M_J = \frac{15}{2}\rangle$. Both ions have their magnetic moments directed parallel to the c axis. By comparison, the ground state of the terbium ion has the largest coefficients for $|M_J = 1, 0, -1 \text{ and } -2\rangle$, corresponding to a magnetic moment perpendicular to the c axis.

Included in table 4-11 are the zero field magnetic moments calculated for the ground state wave functions and the moments measured by neutron diffraction. For the even electron ions, the crystal field eigenfunctions are singlets and the permanent magnetic moments are zero. Therefore, the ground state moments in the magnetically ordered system must be induced entirely by the molecular field. In view of the approximations made in the determination of the strength of H_M , the agreement between calculation and experiment is quite remarkable.

The calculations of this section have demonstrated that the crystal field at the rare earth site determines whether

Table 4-12

Coefficients of the wavefunctions of the ground states of R^{3+} in $R\text{TiO}_3$ for R^{2+} subject to the perturbations H_{CF}^0 and $H_{CF}^+ M$

M_J	Tb		Dy		Ho		Er		Tm		M_J
	H_{CF}	$H_{CF}^+ H_M$	H_{CF}	$H_{CF}^+ H_M$	H_{CF}	$H_{CF}^+ H_M$	H_{CF}	$H_{CF}^+ H_M$	H_{CF}	$H_{CF}^+ H_M$	
15/2			.12+i.01	-.03+i.05	-.08+i.13	.03+i.10	-.49-i.54	.84-i.01			8
13/2	0	0.2+i.01	0	.07-i.03	0	.18+i.20	0	0			7
11/2			.16+i.32	-.19	.49+i.02	.28+i.14	.09-i.09	.18	.49	.85	-6
9/2	-.06+i.06	-.05-i.01	0	.28+i.03	0	.23+i.09	0	0	0	0	5
7/2	0	.09-i.04	.29+i.51	-.34-i.02	27	.20+i.06	.58-i.05	-.30+i.39	-.26+i.16	.29+i.13	4
5/2	.12 i.20	-.07+i.14	0	.31+i.01	0	.25+i.03	0	0	0	0	3
3/2	0	.04-i.30	.16+i.31	.28-i.01	.33-i.16	.27	-.09-i.02	-.01-i.06	.05-i.35	.04-i.33	2
1/2	.66	.24+i.40	0	.26+i.01	0	.27-i.01	0	0	0	0	;
-1/2	0	-.41-i.35	.16+i.29	-.26	.25-i.03	.22+i.05	-.07-i.09	.09-i.01	.27+i.10	.17+i.06	0
-3/2	.49-i.44	.44+i.17	0	.28	0	.21+i.10	0	0	0	0	-1
-5/2	0	-.31	.13+i.33	-.32	.35+i.09	.23+i.13	-.22+i.14	.03-i.11	-.18+i.30	-.07+i.12	-2
-7/2	-.04-i.24	.14-i.09	0	.35-i.01	0	.23+i.10	0	0	0	0	-3
-9/2	0	-.03+i.09	.17+i.34	-.29+i.02	-.26-i.05	.20+i.05	.09+i.04	-.02+i.02	-.10-i.29	-.02-i.10	-4
11/2	-.09-i.01	-.02-i.06	0	.19	0	.23+i.05	0	0	0	0	-5
13/2	0	.02+i.02	i.11	-.08-i.03	-.47-i.12	.31+i.02	-i.07	.01+i.02	.38+i.31	.06+i.05	-6
15/2			0	.03+i.05	.05-i.15	.27-i.07	0	0	0	0	-7
											-8

the rare earth moments lie parallel or perpendicular to the orthorhombic c axis. It would be of interest to determine if the symmetry of the crystal field needs to be as low as C_s in order to predict this behaviour, or if a crystal field with some higher symmetry would suffice. Thus, the above calculations were repeated with a crystal field Hamiltonian of D_{4h} symmetry, and with the parameters of O'Hare and Donlan (1976).

The results of the calculations are shown in table 4-13. In every case, the direction of the rare earth moment predicted by the D_{4h} crystal field plus molecular field agrees with the rare earth moment direction determined by neutron diffraction experiments. Therefore, although the observed rare earth optical absorption spectrum ought to be fitted to a C_s crystal field, the observed axial-planar orientation of the rare earth moments can be explained with a crystal field of D_{4h} symmetry.

D_{4h} symmetry can be obtained from cubic symmetry by applying an axial distortion along one of the 4-fold cube axes. The distortion is represented by the $B_0^2 C_0^2$ term in the D_{4h} crystal field Hamiltonian. If it were the only term in the crystal field, it would arrange the crystal field wavefunctions in order of increasing or decreasing $|M_J\rangle$. Whether the ground states corresponded to maximum $|M_J|$, i.e. moments parallel to the unique axis, or minimum $|M_J|$, i.e. moments perpendicular to the unique axis, would depend on the sign of the

Table 4-13

Energies and permanent magnetic moments of the ground states of R^{3+} in $RTiO_3$ for R^{3+} in D_{4h} symmetry

R	E_0 (cm^{-1}) (H_{CF})	E_0 (cm^{-1}) ($H_{CF}+H_M c$)	E_0 (cm^{-1}) ($H_{CF}+H_M \perp c$)	Moment direction (exp)	$\langle \mu \rangle_{exp}$ (μ_B)	$\langle \mu \rangle_{calc}$ (μ_B)
Tb	-284	-285	-340	$\perp c$	$8.1 \pm .4$	7.0
Dy	-201	-223	-315	$\perp c$	$9.7 \pm .8$	9.8
Ho	-117	-161	-215	$\perp c$	$8.1 \pm .5$	9.5
Er	-216	-289	-219	$ c$	$7.9 \pm .4$	9.0
Tm	-425	-528	-428	$ c$	$6.0 \pm .3$	7.0

$B_0^2 C_0^2$ term. Although this is not the only term in the D_{4h} crystal field Hamiltonian, it makes a major contribution and the same systematics are present. The variation in sign of this term across the rare earth series is governed by the sign of C_0^2 , because B_0^2 is assumed to be constant. The matrix elements of C_q^k are given by (Wybourne, 1965)

$$\langle SLJJ_z | C_q^k | SLJJ_z \rangle = \langle \ell || C^k || \ell \rangle (-)^{J-J_z} \begin{Bmatrix} J & k & J \\ -J_z & q & J_z \end{Bmatrix} (-)^{S+L+J+k}$$

$$\begin{Bmatrix} J & J & k \\ L & L & S \end{Bmatrix} (2J+1) \langle SL || U^k || SL \rangle, \quad (4-30)$$

as discussed in section 1-8. The product of the terms which have $k=2$ and are independent of q are positive for erbium and thulium and negative for terbium, dysprosium and holmium. The variation in sign of this product corresponds with the axial-planar orientation of the rare earth moments. Similar behaviour has been reported for the rare earth moments in the systems RCo_5 and R_2Co_{17} (Greedan and Rao, 1973), where the crystal field also is dominated by the $B_0^2 C_0^2$ term. Experiments have shown that the erbium and thulium moments are parallel to the unique axis, while terbium, dysprosium and holmium moments are perpendicular to this axis. The directions deduced were confirmed by a calculation in which the crystal field was represented solely by the $B_0^2 C_0^2$ term.

The magnetic moments calculated for the ground state for the D_{4h} crystal field plus molecular field are compared with the results of neutron diffraction experiments in table 4-13. The agreement is not as good as for the C_s crystal field (Table 4-11).

4.4 Temperature Dependence of the Magnetization

The temperature dependence of the total magnetization in the system $RTiO_3$ for $R = Tb, Dy, Ho, Er$ and Tm was measured by neutron diffraction techniques. In every case, the intensity of a ferrimagnetic peak with a large magnetic contribution, such as (110), (002) or (200), (112), (021), was monitored as a function of temperature for temperatures ranging from 10K to the critical temperature. For $TbTiO_3$, $DyTiO_3$ and $HoTiO_3$, the intensity of an antiferromagnetic reflection was monitored as well. The critical temperature was estimated by extrapolation from plots of magnetization against temperature to the temperature at which the magnetization vanished. Sufficient data were not collected near T_c to justify plotting the magnetization cubed against temperature and estimating the critical temperature by extrapolation of the linear portion of the curve, as was discussed in section 4-1. Table 4-14 compares the critical temperatures determined from bulk magnetic measurements and by neutron diffraction. The agreement is good in every case.

Table 4-14

Critical temperatures for $RTiO_3$, $R = Tb-Tm$, from spontaneous magnetization (a) and neutron diffraction (b)

	Tb	Dy	Ho	Er	Tm
T_c °K $\pm 1^\circ$ K a)	48	64	55	40	57
T_c °K $\pm 1^\circ$ K b)	50	61	55	39	57

Figure 4-12 shows a plot of the reduced magnetization (σ) against reduced temperature (τ) for ErTiO_3 where reduced magnetization and reduced temperature are defined as $M(T)/M(0)$ and T/T_c respectively. Similar data are shown for TmTiO_3 in appendix C. Figures 4-13a and 4-13b display the reduced magnetization against reduced temperature for TbTiO_3 where separate plots are shown for ferrimagnetic and antiferromagnetic reflections. Data for DyTiO_3 and HoTiO_3 are given in Appendix C. Figures 4-12 and 4-13 include reduced magnetization vs. reduced temperature calculated for a ferromagnet with J equal to the free ion angular momentum quantum number and J equal to $\frac{1}{2}$. In each case, the data agree well with the calculation for $J = \frac{1}{2}$. This behaviour can be put into perspective by comparison with the rare earth iron garnets.

The rare earth iron garnets (RIG) have the formula $\text{R}_3\text{Fe}_5\text{O}_{12}$. They are cubic and belong to space group I_{a3d} with $Z = 8$. The R-atoms occupy the 24 c sites (dodecahedral), one set of Fe atoms occupy the 24 d sites (tetrahedral) and the others the 16 a sites (octahedral). The critical temperatures for RIG, $R = \text{Gd-Lu}$ and Y , are nearly identical, hence R - Fe exchange is small compared to Fe-Fe exchange (Pauthenet, 1958). Below T_c , the 16 irons on the a sites are antiparallel to the 24 irons on d sites and the net iron moment is antiparallel to the moment of the 24 rare earth ions on c sites (Pauthenet,

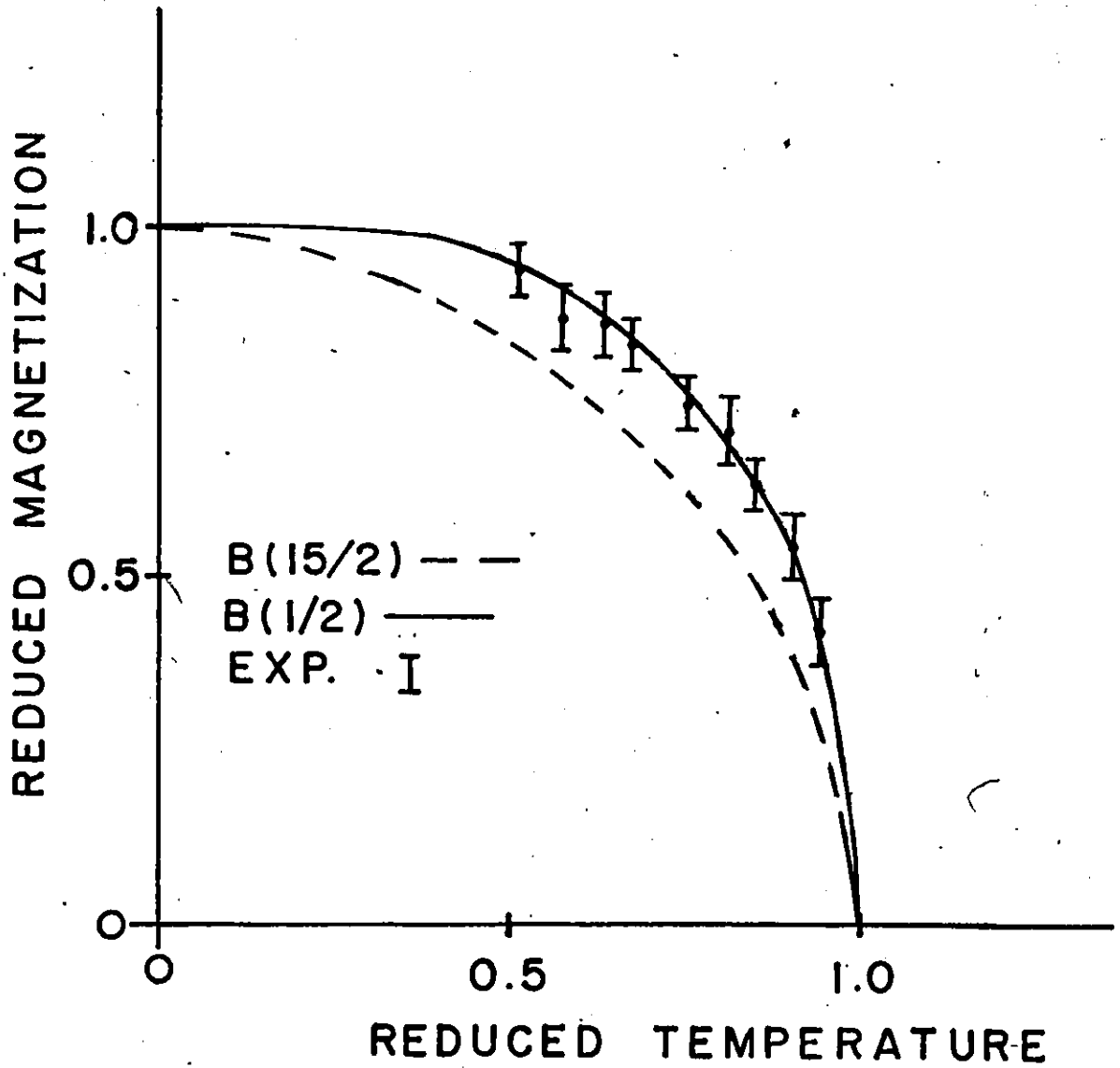


Fig. 4-12 Reduced magnetization versus reduced temperature for the (110) ferrimagnetic reflection of ErTiO_3 .

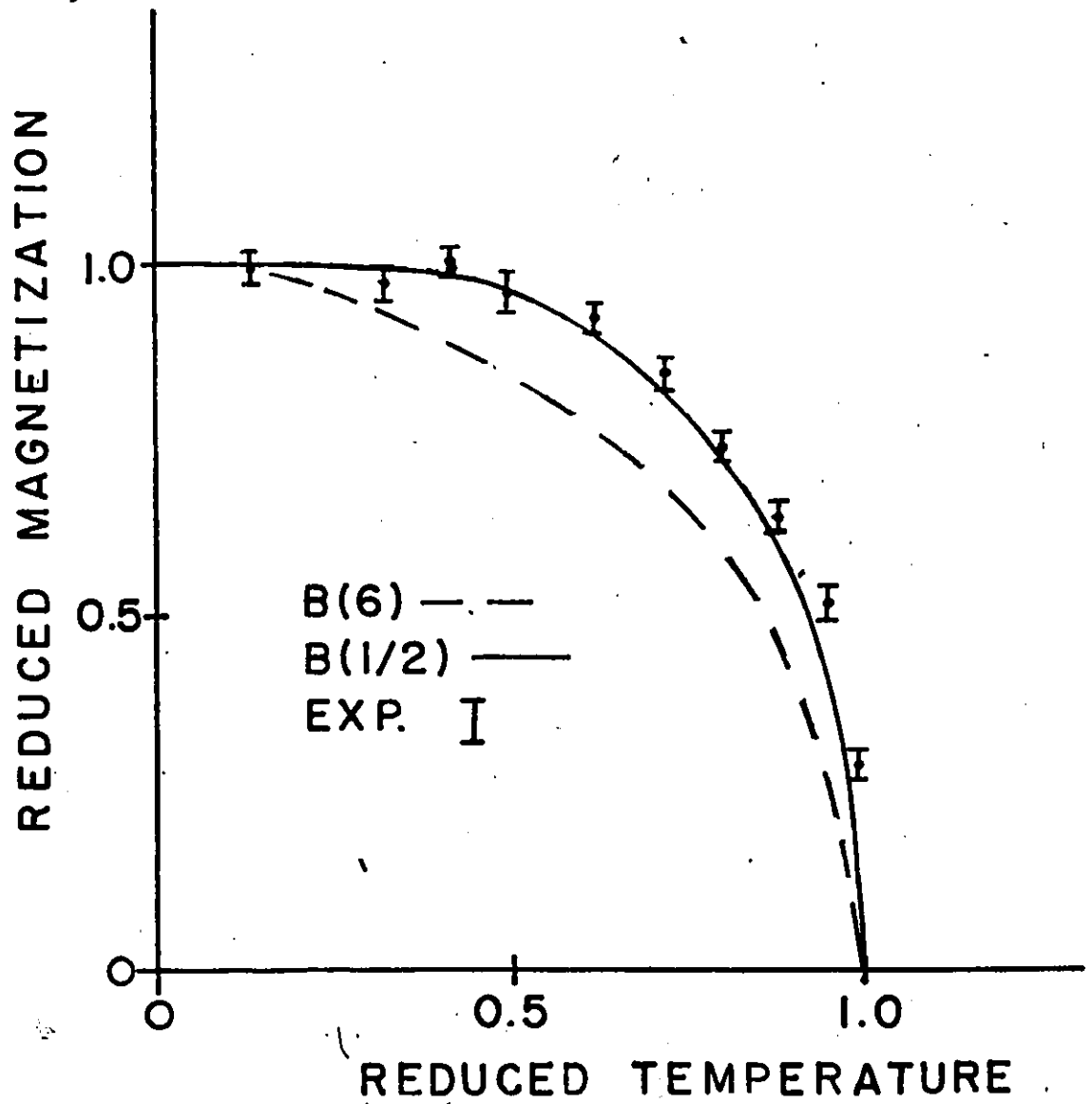


Fig. 4-13 a) Reduced magnetization versus reduced temperature for the (110), (002) ferrimagnetic reflection of TbTiO_3 .

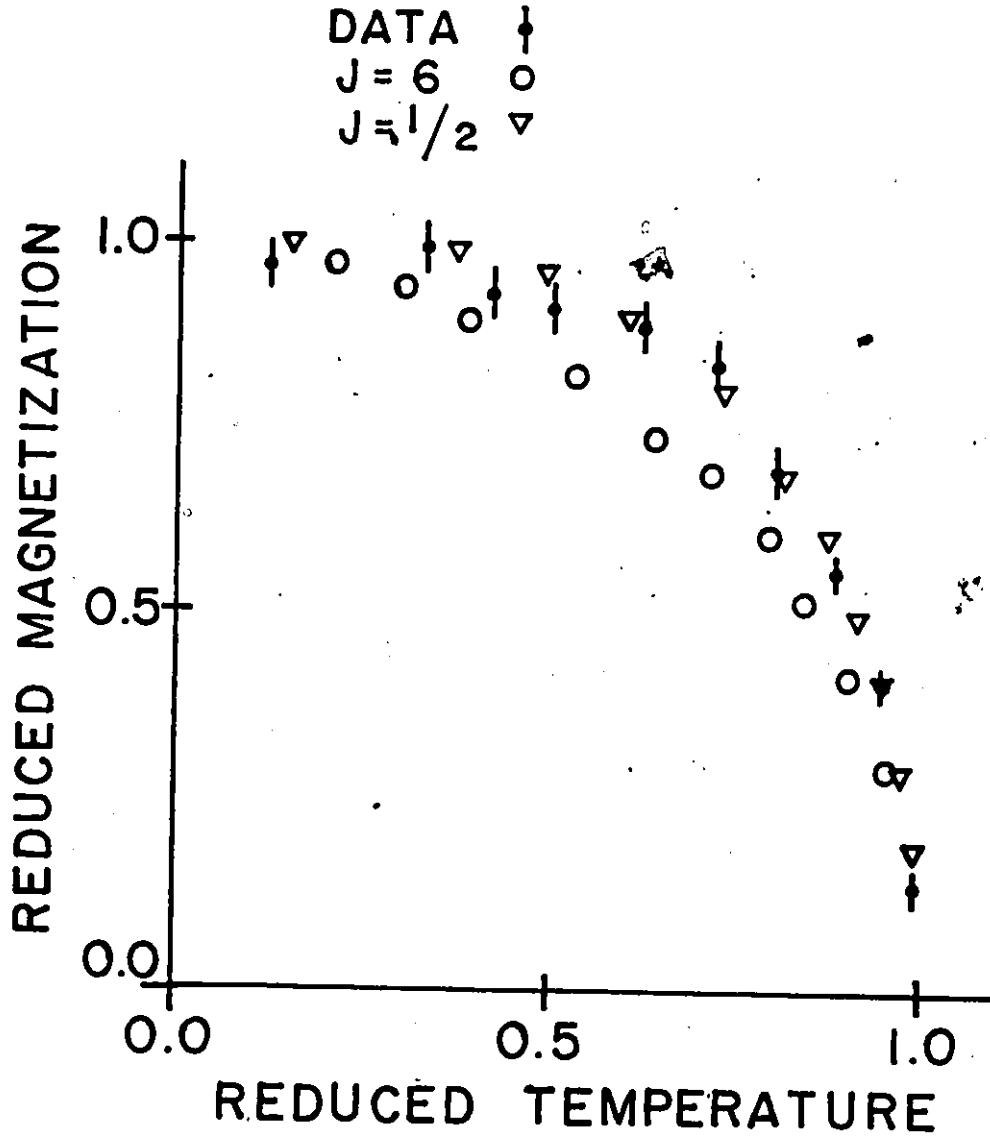


Fig. 4-13 b) Reduced magnetization versus reduced temperature for the (102), (012) anti-ferromagnetic reflection of TbTiO_3 .

1958). As a consequence of the weak R-Fe coupling and the high critical temperature (≈ 560 K), the rare earth sublattice magnetization grows comparatively slowly with decreasing temperature down to approximately 400 K. Below 400 K, it increases more rapidly and we observe a compensation temperature where the direction of magnetization switches from being parallel with the net iron moment to parallel with the rare earth magnetization. This behaviour is shown schematically in figure 4-14.

By comparison, the critical temperatures of $RTiO_3$ depend strongly on the identity of R which indicates that R-Ti exchange is comparable in magnitude with Ti-Ti coupling. In addition, T_c for $RTiO_3$ is one order of magnitude smaller than for RIG. As a result, the thermal energy of the rare earth moments in $RTiO_3$ will be smaller than in RIG at the critical temperature. The lower thermal energy of the rare earth moments at T_c plus the relatively larger R-Ti coupling has the result that the rare earth sublattice magnetization increases more rapidly with decreasing temperature in $RTiO_3$ than in the garnets.

The magnetic scattering from $RTiO_3$ is sufficiently dominated by the contributions from the rare earth moments

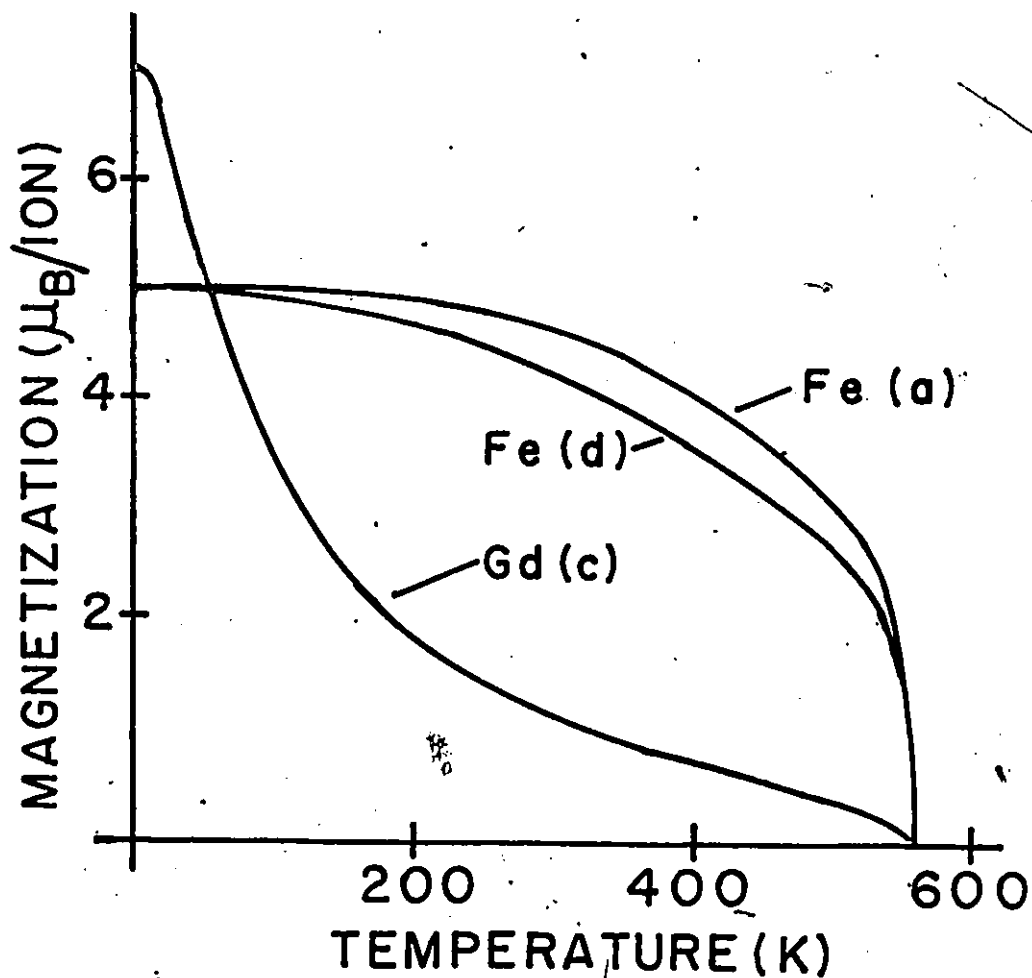


Fig. 4-14 Temperature dependence of the Fe^{3+} and Gd^{3+} sublattice magnetization in $\text{Gd}_3\text{Fe}_5\text{O}_{12}$. The Gd^{3+} moments are antiparallel to the net Fe^{3+} moment and their algebraic sum is zero at the compensation temperature of 290 K (Pauthenet, 1958).

that the data in figures 4-12 and 4-13 show essentially the temperature dependence of the rare earth sublattice magnetization. We see, in accordance with the previous arguments, that the rare earth magnetization grows rapidly with decreasing temperature. However, it is not clear why it should follow so closely a spin $\frac{1}{2}$ Brillouin function for a ferromagnet. A further understanding must wait until detailed calculations have been performed.

4-5 Bulk Magnetic Data - Single Crystals

Magnetic data were collected for single crystals of ErTiO_3 and HoTiO_3 along the crystallographic axes. Figures 4-15a and 4-15b show the magnetic anisotropy of HoTiO_3 in the ab and bc planes respectively. The data clearly show that the b axis is the easy axis of magnetization - in agreement with the results of the neutron diffraction experiments. Figure 4-16 shows the magnetization at 4.2K against the applied magnetic field along the three crystallographic axes of HoTiO_3 . The saturation moment along b is $7.4 \pm .2 \mu_B$ per formula unit. A moment of $6.8 \pm .6 \mu_B$ per formula unit is predicted along the b axis from the magnitudes of the titanium and holmium moments and the angle that the latter makes with the b axis, as determined by neutron diffraction (see table 4-6).

Figure 4-16 shows the same plateau in the magnetiza-

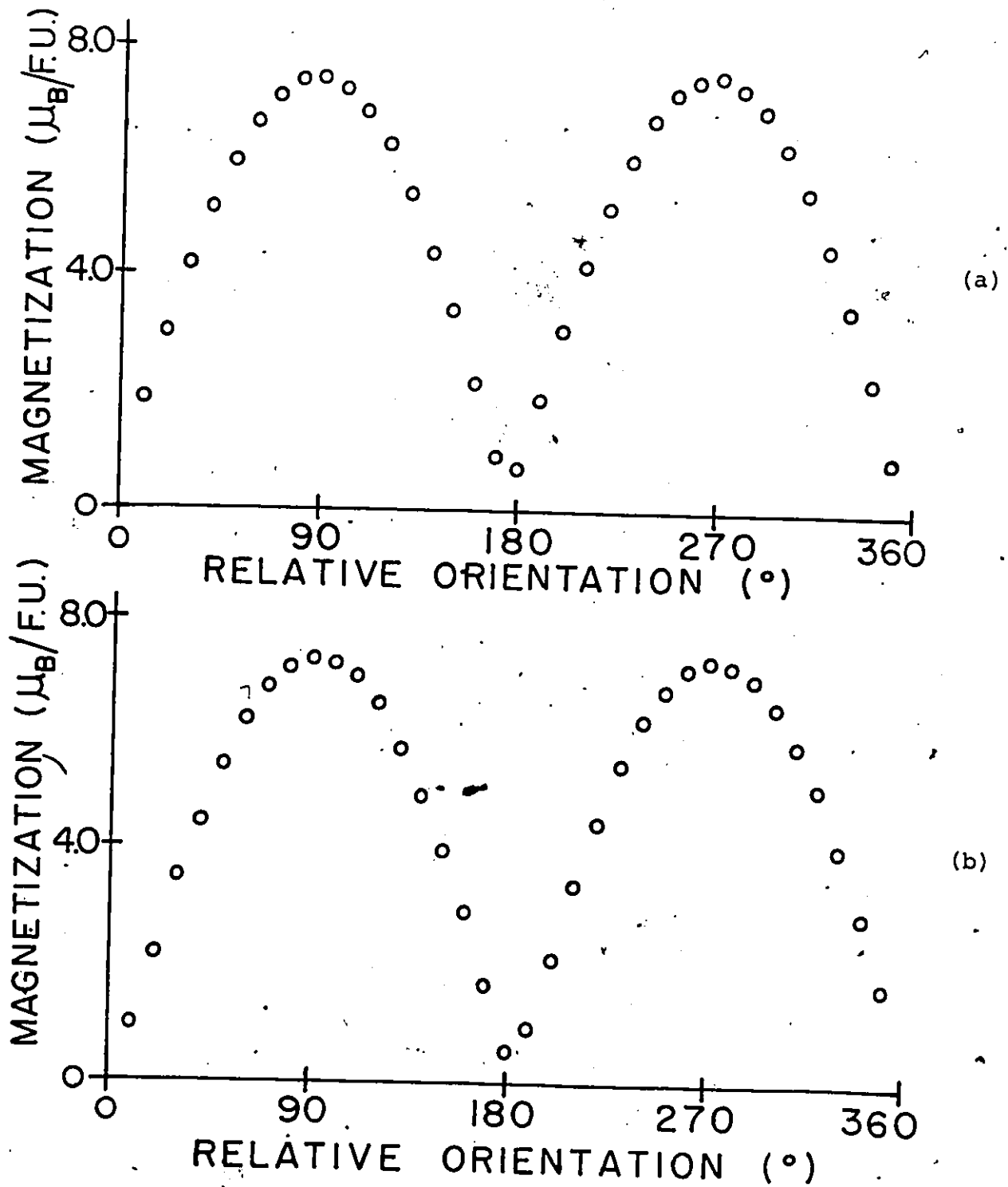


Fig. 4-15 Isothermal (4.2K) magnetization at a field of 7 kilogauss for HoTiO_3 as a function of the orientation in the ab (a) and bc (b) planes. 0° corresponds to the a(c) axis being parallel to the pole axis of the magnet while 90° corresponds to the b axis being parallel.

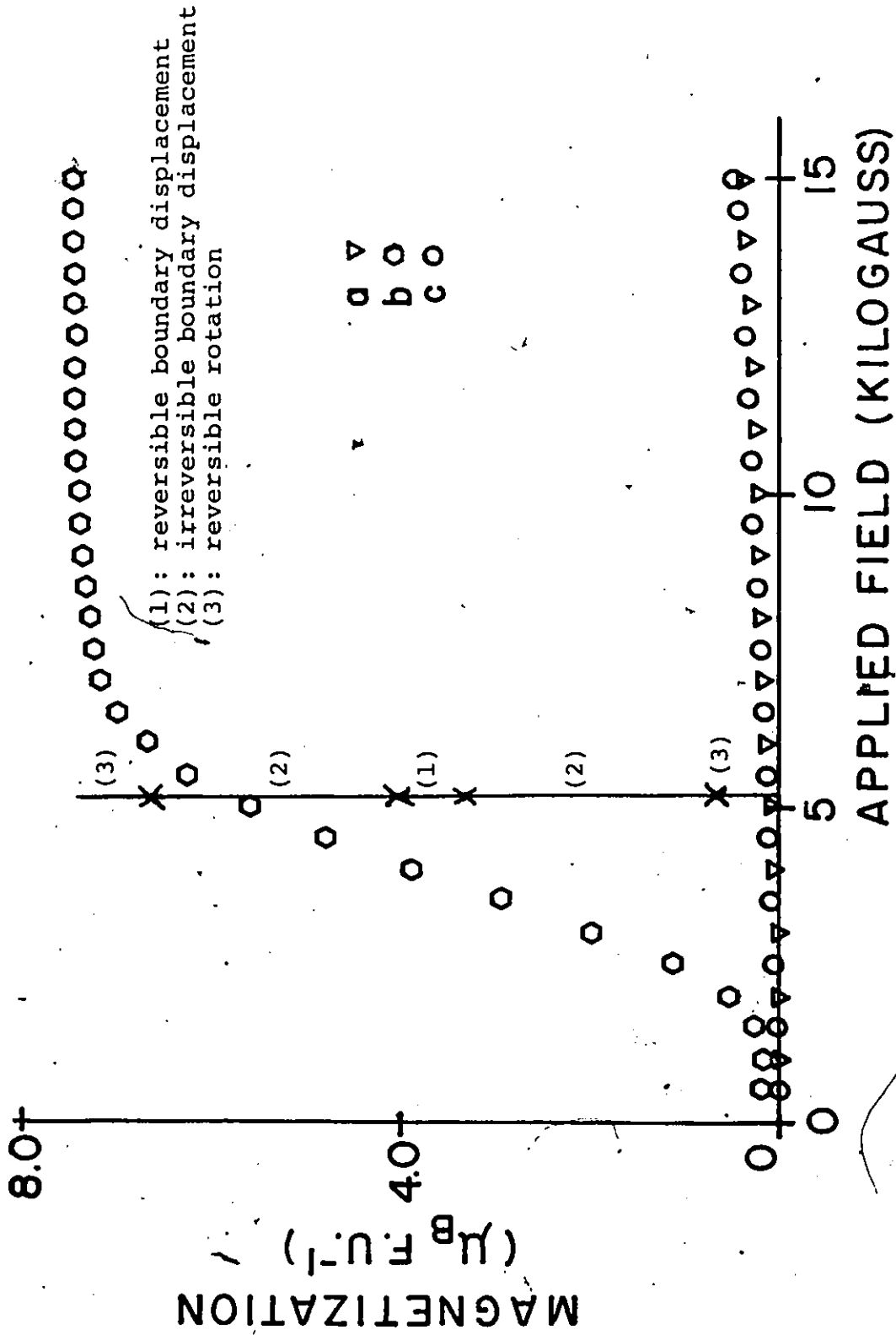


Fig. 4-16 Field dependence of the isothermal (4.2 K) magnetization of HoTiO₃ along the crystallographic axes and fields ranging from 0 → 15 kilogauss.

tion curve between 45 gauss and 5 kilogauss as was observed from the data for a polycrystalline specimen (see figure 4-4). To investigate further, the field dependence of the magnetization was measured along the easy axis at selected temperatures between 4.2K and 30 K. The data are shown in figure 4-17. As expected, the saturation magnetization decreases as the temperature is increased. However, at low applied fields, the magnetization is larger at higher temperatures. This can be understood if we consider the processes which occur as a ferromagnet or a ferrimagnet is magnetized to saturation.

Below the critical temperature and in zero applied field, a ferromagnet or a ferrimagnet will consist of domains. The directions of the domains are distributed in such a way that the magnetization of the sample is zero, or nearly zero (section 4-1). The magnetic moment of a domain is specified by the direction and magnitude of the magnetization and by the volume of the domain. At constant temperature, the magnetization of a ferromagnet or a ferrimagnet is altered by either a change in direction of magnetization of the domain or a change in its volume. The first process, domain rotation, is reversible while the second process, domain wall motion, occurs reversibly and irreversibly (Cullity, 1972). The regions of the magnetization curve where these processes occur are shown in figure 4-16. Any imperfections

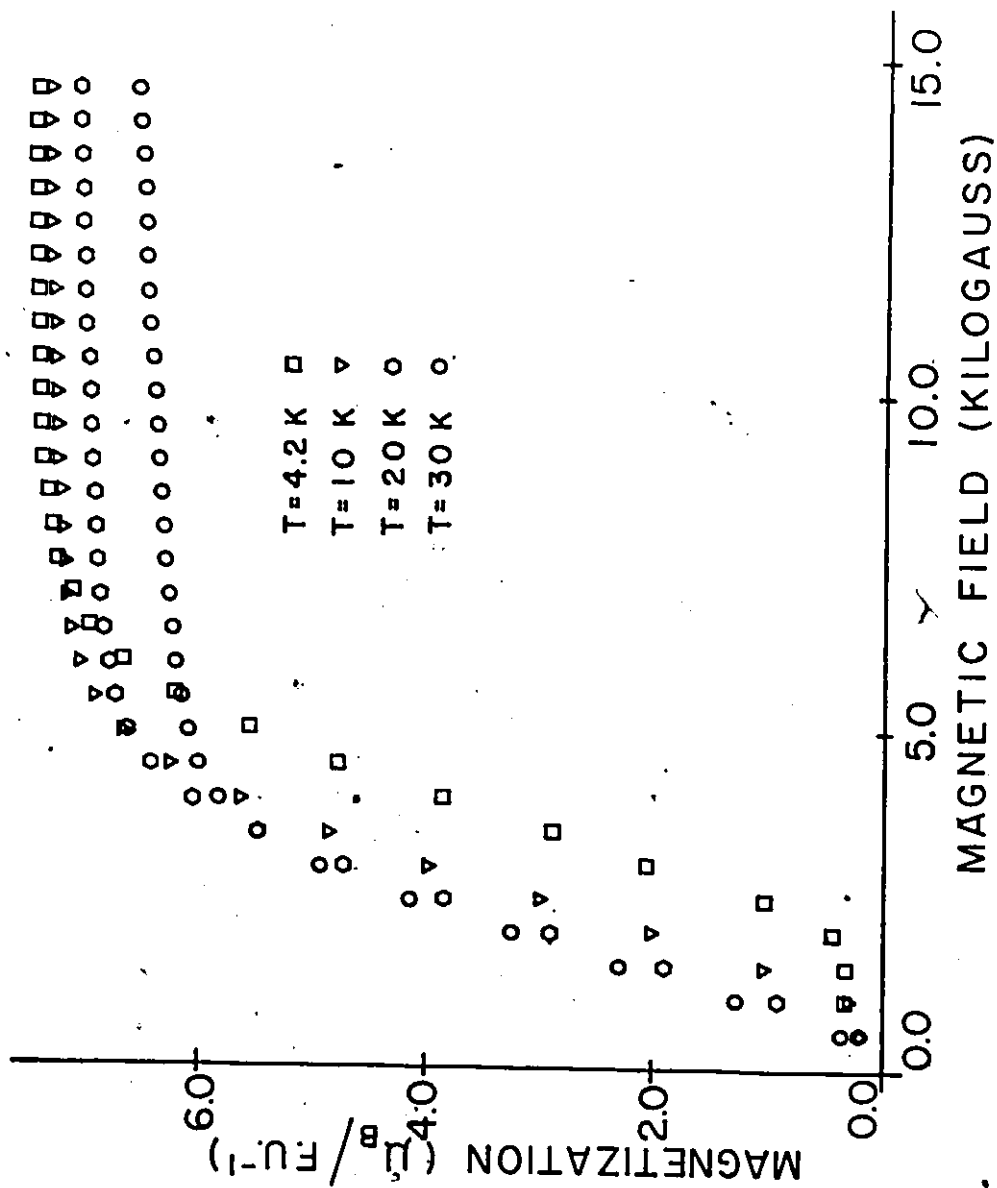


Fig. 4-17 Field dependence of the isothermal magnetization of $HoTiO_3$ at selected temperatures below T_c .

in the crystal lattice can pin the domain wall and hinder either its rotation or displacement through the lattice. Whenever a domain wall is pinned, there will be some activation energy to be overcome before the motion can continue. At higher temperatures, it is easier to move the domain walls through the lattice and so the magnetization at low fields will be higher, as observed in figure 4-17.

The magnetic anisotropy in the bc plane of ErTiO_3 is shown in figure 4-18; it indicates that the c axis is the easy axis of magnetization which agrees with the results of neutron diffraction. Figure 4-19 shows the field dependence of the magnetization along the c axis at selected temperatures between 4.2K and 30K. Once again, the magnetization at low fields is larger for higher temperatures, while the saturation magnetization decreases with increasing temperature. The saturation magnetization at 4.2K is $6.9 \mu_B$ per formula unit as compared with $7.2 \mu_B$ as deduced from neutron diffraction, where the erbium moment is taken from table 4-11 and the titanium moment from table 4-6.

In section 4-1, the equation for the inverse paramagnetic susceptibility for a two sublattice ferrimagnet in the molecular field approximation was given by

$$x^{-1} = \frac{T-\theta}{c} - \frac{\xi}{T-\theta} \quad (4.31)$$

This is derived by defining the magnetization of the rare earth and titanium sublattices as

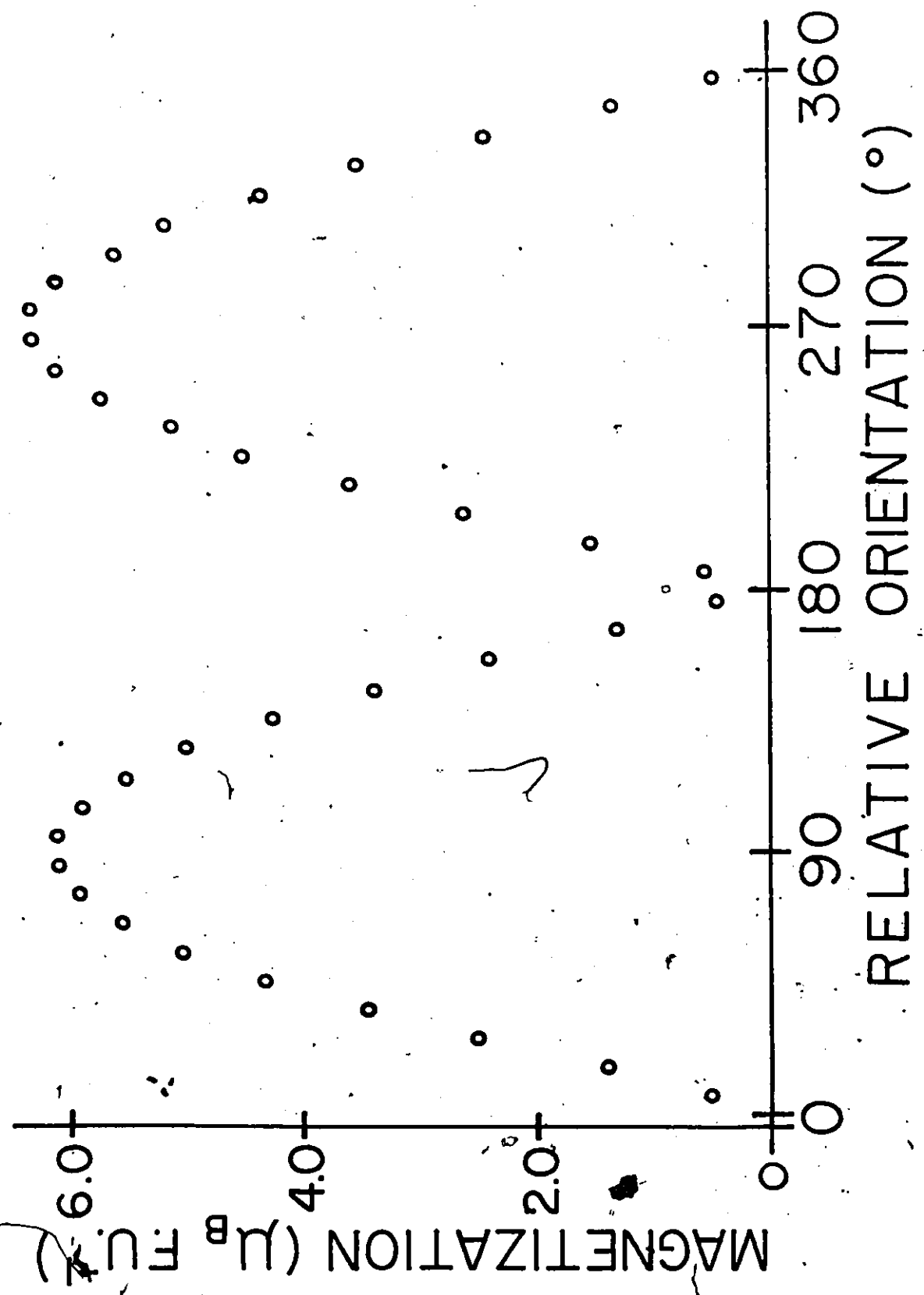


Fig. 4-18 Anisotropy of the magnetization in the bc plane of ErTiO₃. 90° corresponds to the c axis being parallel to the pole axis of the magnet.

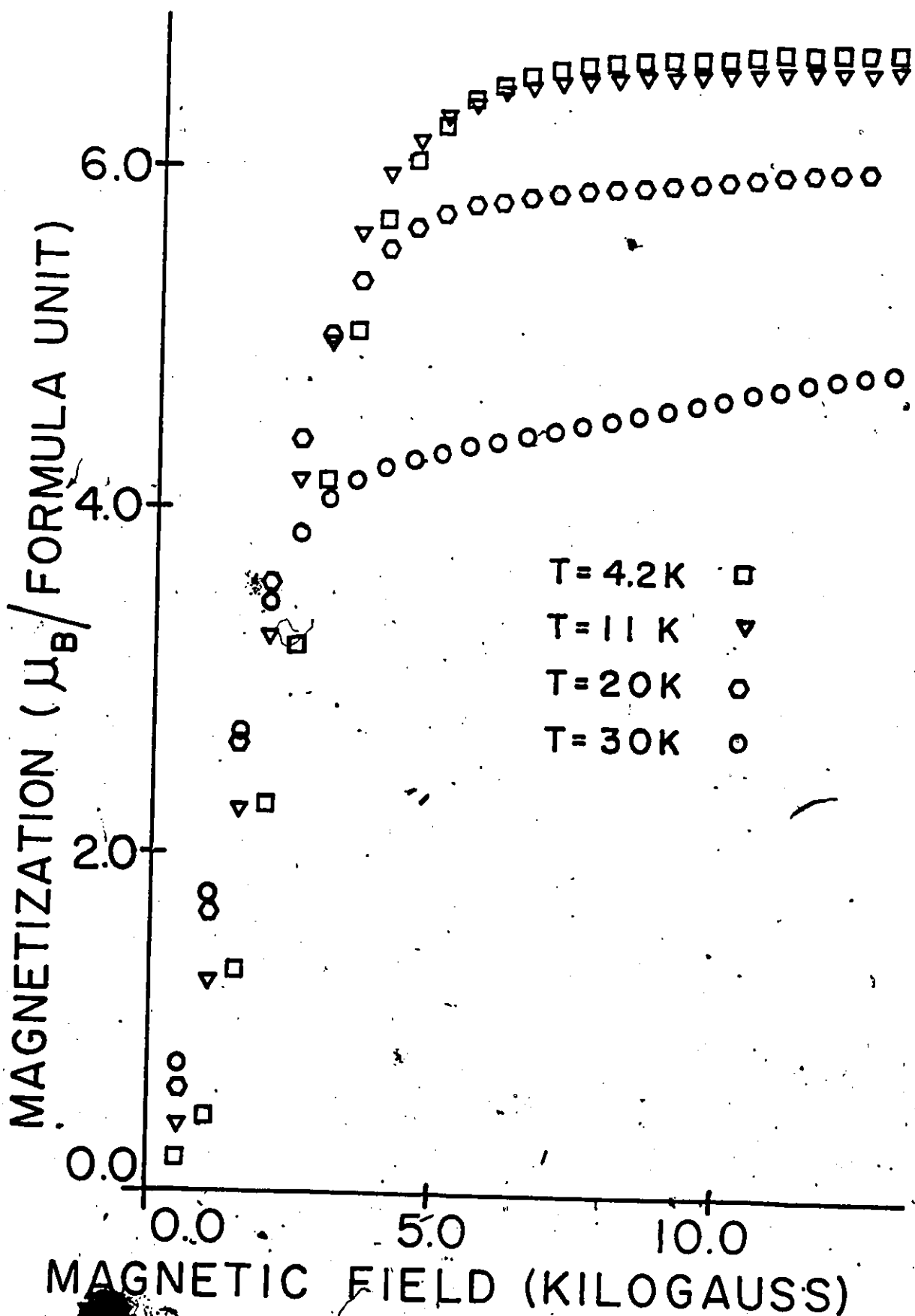


Figure 10. Field dependence of the isothermal magnetization of ErTiO_3 at selected temperatures below T_c .

$$M_{\text{Ti}} = \frac{C_{\text{Ti}}}{T} H_{\text{Ti}} \quad \text{and} \quad M_{\text{R}} = \frac{C_{\text{R}}}{T} H_{\text{R}} \quad (4-32)$$

where

$$H_{\text{Ti}} = H_0 + \lambda_{\text{Ti-Ti}} M_{\text{Ti}} + \lambda_{\text{Ti-R}} M_{\text{R}}, \quad (4-33)$$

$$H_{\text{R}} = H_0 + \lambda_{\text{R-Ti}} M_{\text{Ti}} + \lambda_{\text{R-R}} M_{\text{R}},$$

C_{Ti} = Curie constant for titanium,

C_{R} = Curie constant for the rare earth,

and

H_0 = the external magnetic field.

The paramagnetic susceptibility is defined as

$$\chi = \frac{M}{H_0} \quad \text{where} \quad M = M_{\text{Ti}} + M_{\text{R}}.$$

C_{Ti}/T and C_{R}/T are the free ion susceptibilities of titanium and the rare earth respectively, in the absence of exchange. A plot of χ^{-1} against T for a free ion should be a straight line that passes through the origin. For the two sublattice ferrimagnet, a plot of χ^{-1} against T is a hyperbola. Deviations from free ion behaviour are attributed to exchange. However, in real systems, exchange is not the only perturbation to the free ion susceptibility. The crystal field plays a role as well. If the crystal field splittings are comparable to kT , deviations from free ion behaviour will be observed which are not due to exchange. The susceptibility of a single ion, subject to a crystal field but not to exchange, was first derived by Van Vleck (1932).

$$X = \frac{\sum_i (E_i^{(1)})^2 / kT - 2E_i^{(2)} \exp(-E_i^{(0)}/kT)}{\sum_i \exp(-E_i^{(0)}/kT)}$$

where $E_i^{(0)}$ = i th crystal field energy level

$$E_i^{(1)} = g\mu_B \langle i | \tilde{J} | i \rangle, \quad (4-35)$$

$$E_i^{(2)} = g^2 \mu_B^2 \sum_{j \neq i} \frac{\langle i | \tilde{J} | j \rangle \langle j | \tilde{J} | i \rangle}{E_i^{(0)} - E_j^{(0)}}$$

$|i\rangle$ = i^{th} wavefunction

and

\tilde{J} = angular momentum operator.

Thus, an expression for the susceptibility of the ferrimagnets, RTiO_3 , was derived in which the free ion rare earth susceptibility, C_R/T , was replaced by the crystal field susceptibility which was calculated from the crystal field wavefunctions and energy levels derived in section 4-3.

Figure 4-20 shows the inverse susceptibility in the paramagnetic regime as a function of temperature for HoTiO_3 along the crystal axes. The susceptibility is largest along the easy axis and is virtually indistinguishable between the a and c axes. The average susceptibility, defined as $\frac{1}{3}(X_a + X_b + X_c)$ agrees with the polycrystalline susceptibility to within a few per cent. Figure 4-21 shows the inverse paramagnetic susceptibility as a function of temperature for ErTiO_3 .

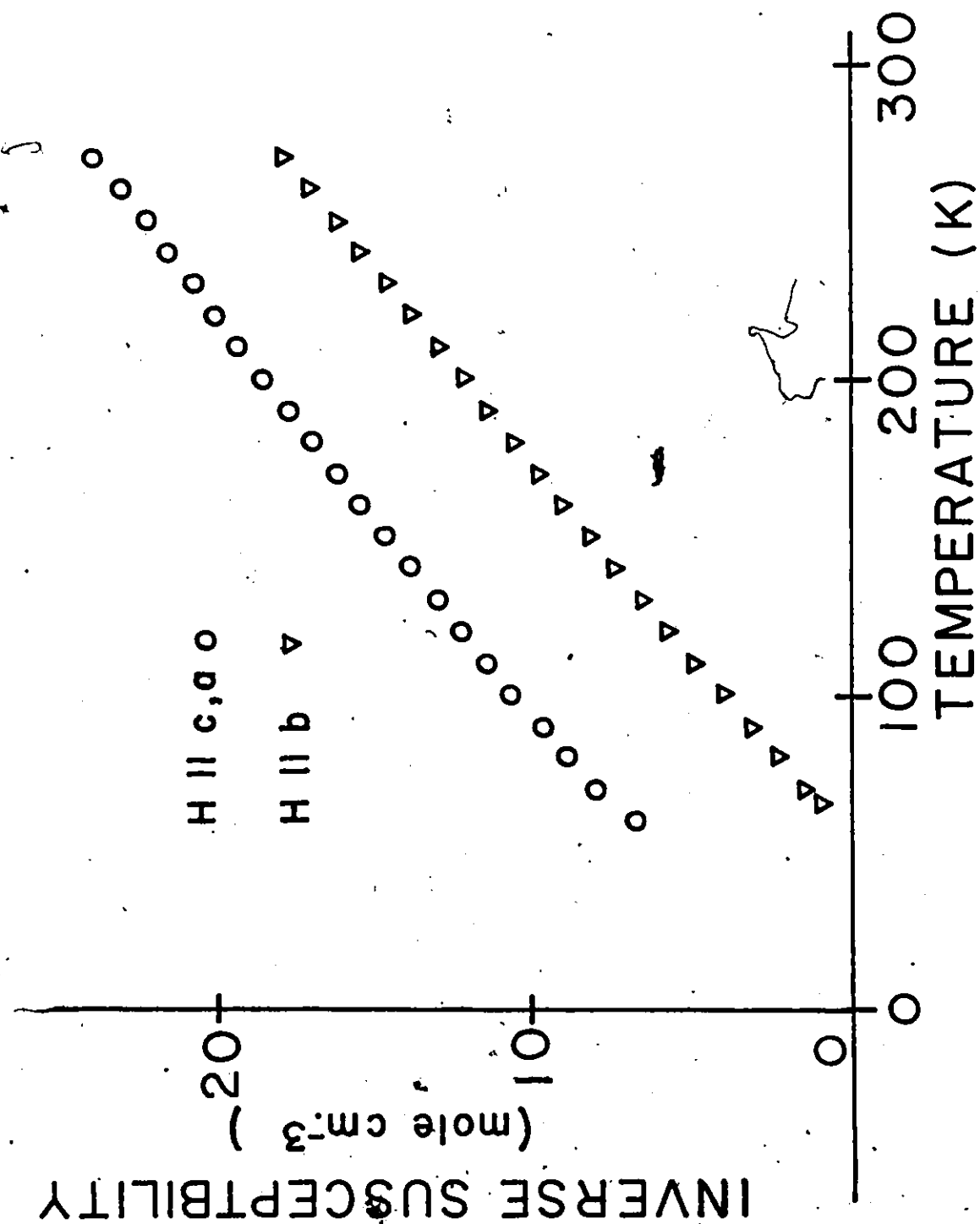


Fig. 4-20 Temperature dependence of the inverse susceptibility of HoTiO_3 along the crystallographic axes.

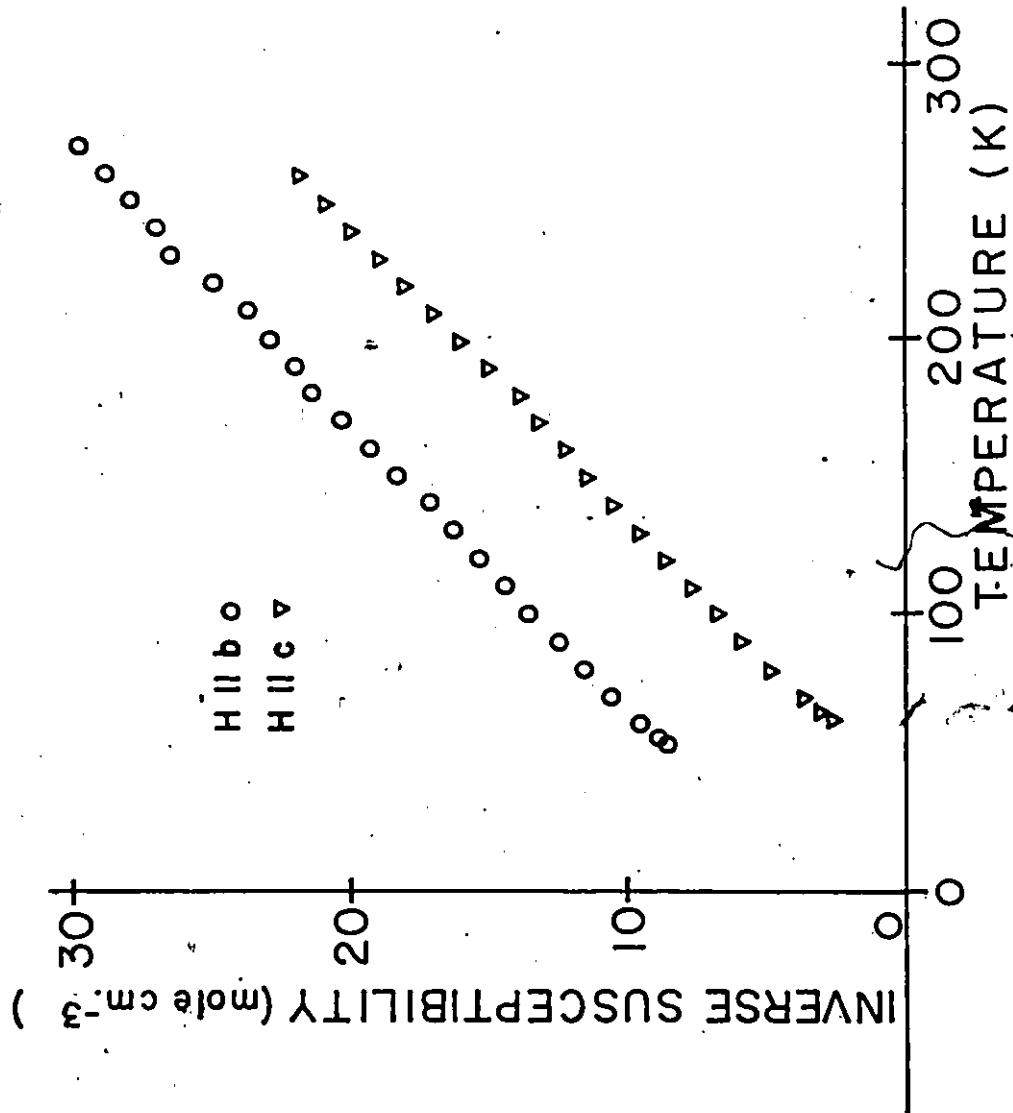


Fig. 4-21 Temperature dependence of the inverse susceptibility of ErTiO_3 along the b and c axes.

measured along the b and c axes. Unfortunately, attempts to fit the data to the paramagnetic susceptibility calculated through consideration of crystal field and exchange effects did not yield meaningful values for the molecular field coupling constants. A refinement of the average susceptibility of HoTiO_3 , defined above as $\frac{1}{3}(X_a + X_b + X_c)$, resulted in the following coupling constants:

$$\lambda_{\text{Ti-Ti}} = 165 \text{ cm}^3/\text{mole}, \quad \lambda_{\text{R-R}} = 6 \text{ cm}^3/\text{mole} \quad \text{and} \quad \lambda_{\text{R-Ti}} = -6 \text{ cm}^3/\text{mole}.$$

Although $\lambda_{\text{Ti-Ti}}$ is not unreasonable (compare table 4-1), in view of the greater spatial extension of the 3d wavefunctions over that of the 4f wavefunctions, $\lambda_{\text{R-Ti}}$ and $\lambda_{\text{R-R}}$ should not have the same magnitude. A refinement of the susceptibility of ErTiO_3 measured along the c axis yielded

$$\lambda_{\text{Ti-Ti}} = -25 \text{ cm}^3/\text{mole}, \quad \lambda_{\text{R-Ti}} = -15 \text{ cm}^3/\text{mole} \quad \text{and} \quad \lambda_{\text{RR}} = 1 \text{ cm}^3/\text{mole}.$$

$\lambda_{\text{R-R}}$ and $\lambda_{\text{R-Ti}}$ compare well with the values given in table 4-1, but $\lambda_{\text{Ti-Ti}}$ is not sensible because the titanium sublattice is definitely ferromagnetic.

We conclude that an explicit account of the crystal field acting on the rare earth ion does not lead to a better determination of the molecular field coupling constants. Unless kT is large compared to the overall separation of the crystal field energy levels, each state will not be equally populated. Therefore, the paramagnetic susceptibility will

depend critically on the separation between energy levels and the magnetic moment of each level. This is the situation with respect to both holmium and erbium in RTiO_3 where the overall splittings were calculated to be 717K and 772K respectively. Uncertainties in the crystal field parameters can lead to errors in both the level splittings and the magnetic moments of each level. These, in turn, will affect the calculated susceptibility. In the paramagnetic regime, the molecular field is a small perturbation compared to the crystal field. This is unlike the situation at or below the critical temperature, where the molecular field is much greater due to the large spontaneous magnetization. Since the molecular field is a small perturbation above T_c , uncertainties in the crystal field intensities make it impossible to determine sensible molecular field coupling constants.

CHAPTER 5
CONCLUSIONS

Some magnetic properties of the heavy rare earth titanium oxides have been investigated and comparisons have been made with the rare earth iron garnets and the isostructural RMO_3 , $M = \text{Fe}, \text{Cr}$ and Al . The rare earth titanium oxides are distinguished by a ferromagnetic exchange coupling between the titanium moments which is comparable in magnitude to the antiferromagnetic rare earth-titanium exchange. With the titanium moments in a ferromagnetic array, the isotropic rare earth-titanium coupling does not vanish by symmetry, hence both moments order at the same critical temperature. This behaviour can be contrasted with RMO_3 , $M = \text{Fe}$ or Cr , where the R-M isotropic exchange is zero as a consequence of antiferromagnetic ordering of the iron and chromium. This results in the rare earth and transition metal moments being ordered at very different critical temperatures; the upper one ($\sim 100\text{K}$ for Cr and $\sim 600\text{K}$ for Fe) corresponds to ordering of the $\text{Cr}(\text{Fe})$ moments and the lower one ($\sim 4\text{K}$) represents ordering of the rare earth moments (Goodenough and Longo, 1970). Evidence that the R-Ti exchange cannot be ignored compared to the Ti-Ti exchange is found in the temperature dependence of the rare earth sublatt-

tice magnetization as determined by neutron scattering and in the strong dependence of the critical temperatures on the identity of R. Such is not the case in the rare earth iron garnets where the R-Fe exchange is much smaller than the Fe-Fe exchange with the result that the critical temperatures are essentially independent of the identity of R (Pauthenet, 1958).

The magnetic structures of $RTiO_3$, $R = Tb-Tm$, were solved with neutron diffraction techniques and compared with the isostructural $RMnO_3$. The directions of the rare earth sublattice magnetization below the respective critical temperatures were essentially the same for a given rare earth ion in the series $RMnO_3$, $M = Fe, Cr, Al$ and Ti for $R = Tb-Tm$. We attribute this to the interaction between the 4f electrons on the rare earth ion and the crystal field. Calculations in which the rare earth ion was subject to a crystal plus molecular field have shown that the energy is a minimum for erbium and thulium moments which are parallel to the c axis, while for $R = Tb, Dy$ and Ho , the minimum energy occurs when the moments are perpendicular to the c axis. By repeating the calculation with crystal fields of progressively higher symmetry, we established a correlation between the preferred direction of the rare earth magnetization with respect to the c axis and a single term in the crystal field Hamiltonian which represents an axial distortion from cubic symmetry.

The existence of a canted arrangement for the rare earth moments in the ab plane as opposed to a strictly colinear struc-

ture when they are parallel to the c axis is also a consequence of the interaction between the 4f electrons and the crystal-line environment. The magnetocrystalline anisotropy energy, which can be written as $\hat{M} \cdot \bar{\Gamma} \cdot \hat{M}$, will be a minimum when the rare earth moments lie along one of the principal axes of $\bar{\Gamma}$. A transformation of the principle axes from one rare earth site to another in the unit cell leads directly to the observed spin structures in RMO_3 , $M = \text{Fe, Cr, Al and Ti}$.

It is interesting to note that, for $R = \text{Tb, Ho and Tm}$, the rare earth moments in the ground state are induced entirely by exchange interactions between the rare earth and titanium ions. This phenomenon has also been observed in systems where the rare earth ion is the only magnetic species. In these systems, the moment is induced by exchange between the rare earth ions themselves (Child et al, 1963) and is known as a "boot-strap magnetism" (Wallace, 1973).

Much of the magnetic behaviour of the heavy rare earth titanium oxides is now understood. When larger single crystals of these materials become available one could measure the spin wave dispersion curves by inelastic neutron scattering and obtain better estimates of the exchange integrals. These could lead to a better understanding of the variation of the critical temperature across the series. The temperature dependence of the rare earth sublattice magnetization could also be determined more precisely from single crystals although the data

should then be analyzed with a theory which goes beyond the assumptions of mean field theory. Now that susceptibility data from single crystals of HoTiO_3 and ErTiO_3 are available, it is desirable to have a more accurate set of crystal field coefficients, although this may not be possible considering the number of independent parameters in the crystal field Hamiltonian.

REFERENCES

- P.W. Anderson, Magnetism, Vol. 1, eds: G.T. Rado and H. Suhl, Academic Press, New York, 1963.
- G. Arfken, Mathematical Methods for Physicists, Academic Press, New York, 1970.
- N.W. Ashcroft and N.D. Mermin, Solid State Physics, Holt, Rinehart and Winston, 1976.
- G.E. Bacon, Neutron Diffraction, Clarendon Press, Oxford, 1975.
- G.V. Basuev and G.P. Shviekan, Russian Journal of Inorganic Chemistry 22 (5), 675 (1977).
- E.F. Bertaut, Magnetism, Vol. III, eds.: G.T. Rado and H. Suhl, Academic Press, New York, 1963.
- E.F. Bertaut, G. Buisson, A. Delapalme, B. Van Laar, R. Lemaire, J. Mareschal, G. Roult, J. Schweitzer, Vic Van Qui, H. Bortholin, M. Mercier and R. Pauthenet, Proc. Int. Conf. Mag., Nottingham, England, 275 (1964).
- E.F. Bertaut and J. Mareschal, Solid State Comm. 5, 93 (1967a).
- E.F. Bertaut, J. Mareschal and G.F. DeVries, J. Phys. Chem. Solids 28, 2143 (1967b).
- E.F. Bertaut, J. Chappert, J. Mareschal, J.P. Rebouillat and J. Sivardière, Solid State Comm. 5, 293 (1967c).
- E.F. Bertaut, Acta Cryst. A24, 217 (1968).

- P.R. Bevington, Data Reduction and Error Analysis for the Physical Sciences, McGraw-Hill, 1969.
- J.J. Bielen, J. Mareschal and J. Sivardière, *Z. Angew Phys.* 23, 243 (1967).
- R. Bidaux and P. Mériel, *J. Phys. (Paris)* 29, 220 (1968).
- R.R. Birss, Symmetry and Magnetism, North Holland Publishing Co., Amsterdam, 1964.
- S.S. Bishton and D.J. Newmann, *J. Phys. C* 3, 1753 (1979).
- H.R. Child, M. K. Wilkinson, J.W. Cable, W.C. Koehler and E.O. Wollan, *Phys. Rev.* 131, 922 (1963).
- B.D. Cullity, Introduction to Magnetic Materials, Addison-Wesley Publishing Co., 1972.
- G.H. Dieke, Spectra and Energy Levels of Rare Earth Ions in Crystals, Interscience, New York, 1968.
- G. Donnay, L.M. Corliss, J.D.H. Donnay, N. Elliot and J.M. Hastings, *Phys. Rev.* 112, 1917 (1958).
- I.E. Dzyaloshinsky, *J. Phys. Chem. Solids* 4, 214 (1958).
- A.J. Freeman and R.E. Watson, *Acta Cryst.* 14, 27 (1961).
- J.D. Garrett, J.E. Greedan and D.A. MacLean, *Mat. Res. Bull.* 16, 145 (1981).
- J.B. Goodenough, *Phys. Rev.* 100, 564 (1955).
- J.B. Goodenough, *J. Phys. Chem. Solids* 6, 287 (1958).
- J.B. Goodenough and J.M. Longo, Crystallographic and Magnetic Properties of Perovskite and Perovskite-related Compounds, *Londolt-Bornstein Tabellen Neure Serie 111/4a*, Springer-Verlag, Berlin, 1970.

- J.P. Goral and J.E. Greedan, *J. Solid State Chem.* (June 1982).
- J.E. Greedan and D.A. MacLean, *Inst. Phys. Conf. Sec. No. 37*, 249 (1978).
- J.E. Greedan and V.U.S. Rao, *J. Solid State Chem.* 6, 387 (1973).
- I.I. Gurevich and L.V. Tarasov, North-Holland Publishing Co., Amsterdam (1968).
- W.C. Hamilton, *Acta Cryst.* 18, 502 (1965).
- W. Heisenberg, *Z. Phys.* 38, 411 (1926).
- P. Heller and G. Benedek, *Phys. Rev. Lett.* 14, 71 (1965).
- A. Herpin and P. Mériel, *Compt. Rend.* 259, 2416 (1964).
- M.T. Huchings, *Solid State Physics*, Vol. 16, Academic Press, New York, 1964.
- D.C. Johnson, Ph.D. Thesis, University of San Diego (1975).
- B.R. Judd, *Operator Techniques in Atomic Spectroscopy*, McGraw-Hill
- J. Kanamori, *J. Phys. Chem. Solids* 10, 87 (1959).
- N. Karaziania, D.E. Wortman and C.A. Morrison, *Solid State Comm.* 18, 1299 (1976).
- W.C. Koehler, E.O. Wollan and M.K. Wilkinson, *Phys. Rev.* 118, 58 (1960).
- G.F. Koster, J. O. Dimmock, R.G. Wheeler and H. Statz, *Properties of the Thirty-Two Point Groups*, M.I.T., Cambridge, Mass., 1963.
- H. Kramers, *Proc. Acad. Sci. Amsterdam* 33, 959 (1930).
- H. Kramers, *Physica* 1, 182 (1934).

- I.N. Levine, Quantum Chemistry, Allyn and Bacon, Boston, 1974.
- F.E. Mabbs and D.J. Machin, Magnetism and Transition Metal Complexes, Chapman and Hall, London, 1973.
- D.A. MacLean, J. Solid State Chem. 30, 35 (1979).
- D.A. MacLean, Ph.D. Thesis, McMaster University, 1980.
- Marshall and Lovesey, Theory of Thermal Neutron Scattering, Oxford Press, 1971.
- J.J. Mareschal, J. Sivardière, G.F. de Vries and E.F. Bertaut, J. Appl. Phys. 39, 1364 (1968).
- T. Moriya, Phys. Rev. 120, 91 (1960).
- T. Moriya, Magnetism, Vol. 1, eds: G.T. Rado and H. Suhl, Academic Press, New York, 1963.
- A.H. Morrish, The Physical Principles of Magnetism, John Wiley and Sons, New York, 1965.
- C.A. Morrison, D.E. Wortman and N. Karaziania, J. Phys. C., 1299 (1975).
- C.W. Nielson and G.F. Koster, Spectroscopic Coefficients for the p^n, d^n and f^n Configurations, M.I.T. Press, Cambridge, Mass. 1963.
- J.M. O'Hare and V.L. Donlan, Phys. Rev. B 14, 3732 (1976).
- J.M. O'Hare and V.L. Donlan, Phys. Rev. B 15, 10 (1977).
- R. Pauthenet, Ann. Phys. (Paris) 3, 424 (1958).
- K. Rajnak and B.G. Wybourne, J. Chem. Phys. 41, 565 (1964).
- T.B. Reed and E.R. Pollard, J. Crys. Growth 2, 243 (1968).
- H.M. Rietveld, Acta Cryst. 22, 151 (1967).

- M. Rotenberg, R. Birss, N. Metropolis and J.K. Wooten Jr.,
The 3-j and 6-j Symbols, The Technology Press, M.I.T., Cam-
bridge, Mass. 1959.
- J.M. Rowe, Ph.D. Thesis, McMaster University, 1966.
- N. Shamir and V. Atmony, *Physica* 94B, 85 (1978).
- N. Shamir, H. Shaked and S. Shtrikman, *Phys. Rev. B* 24, 6642
(1981).
- R.D. Shannon and C.T. Prewitt, *Acta. Cryst.* B25, 925 (1967).
- B.R. Silver, Irreducible Tensor Methods, Academic Press, New
York, 1976.
- J.S. Smart, Effective Field Theories of Magnetism, W.B. Saun-
ders Company, Philadelphia, 1966.
- L. Solderholm, J.E. Greedan and M.F. Collins, *J. Solid State
Chem.* 35, 385 (1980).
- G.L. Squires, Introduction to the Theory of Thermal Neutron
Scattering, Cambridge University Press, Cambridge, 1978.
- H.E. Stanley, Introduction to Phase Transitions and Critical
Phenomena, Oxford University Press, 1971.
- C. Stassis, H.W. Deckman, B.N. Harmon, J.P. Desclaux and A.J.
Freeman, *Phys. Rev.* B15, 369 (1977).
- T. Tamaki, K. Tsushima and Y. Yamaguchi, *Physica* 86-88B, 923
(1977).
- B.C. Tofield and W.R. Scott, *J. Solid State Chem.* 10, 183 (1974).
- B. Van Laar and J.B.A.A. Elemans, *J. Phys.* 32, 301 (1971).

J.H. Van Vleck, The Theory of Electric and Magnetic Susceptibilities, Oxford University Press, London, 1932.

W.E. Wallace, Rare Earth Intermetallics, Academic Press, New York, 1973.

P. Weiss, J. Phys. Radium 4, 661 (1907).

R.M. White and R.L. White, Phys. Rev. Lett. 20, 62 (1968).

M.M. Woolfson, X-Ray Crystallography, Cambridge University Press, Cambridge, 1970.

B.G. Wybourne, Spectroscopic Properties of Rare Earths, John Wiley and Sons, New York, 1965.

Zijlstra, Experimental Methods in Magnetism, North Holland Publishing Company, Amsterdam (1967).

INTENSITY (ARBITRARY UNITS)

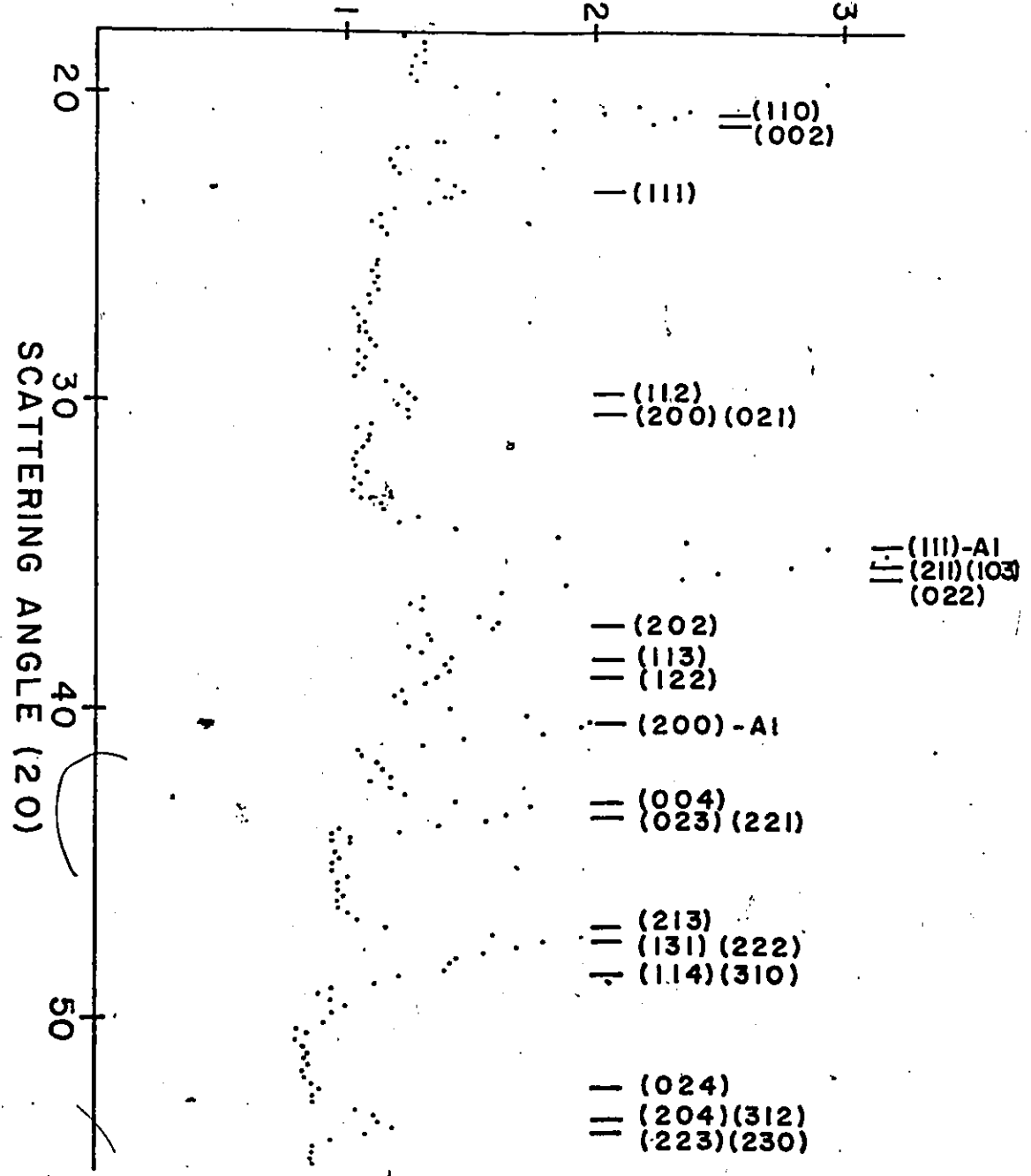


Fig. A-1 Angular dependence of the neutron scattering intensity for $DyTiO_3$ at 100 K.

Table A-1

Comparison of observed and calculated nuclear intensities for DyTiO_3 , $R'' = 7.9\%$

h k l	I_{obs}	I_{calc}
1 1 0	1321±41	1283
0 0 2		
1 1 1	268±25	261
1 1 2	293±31	263
2 0 0		
0 2 1		
2 0 2	605±35	752
1 1 3	586±35	423
1 2 2		
0 0 4	733±40	762
0 2 3		
2 2 1		
2 1 3	684±30	723
1 3 1		
2 2 2		
1 1 4	385±30	480
3 1 0		
0 2 4	450±42	534
2 0 4		
3 1 2		
2 2 3		
2 3 0		

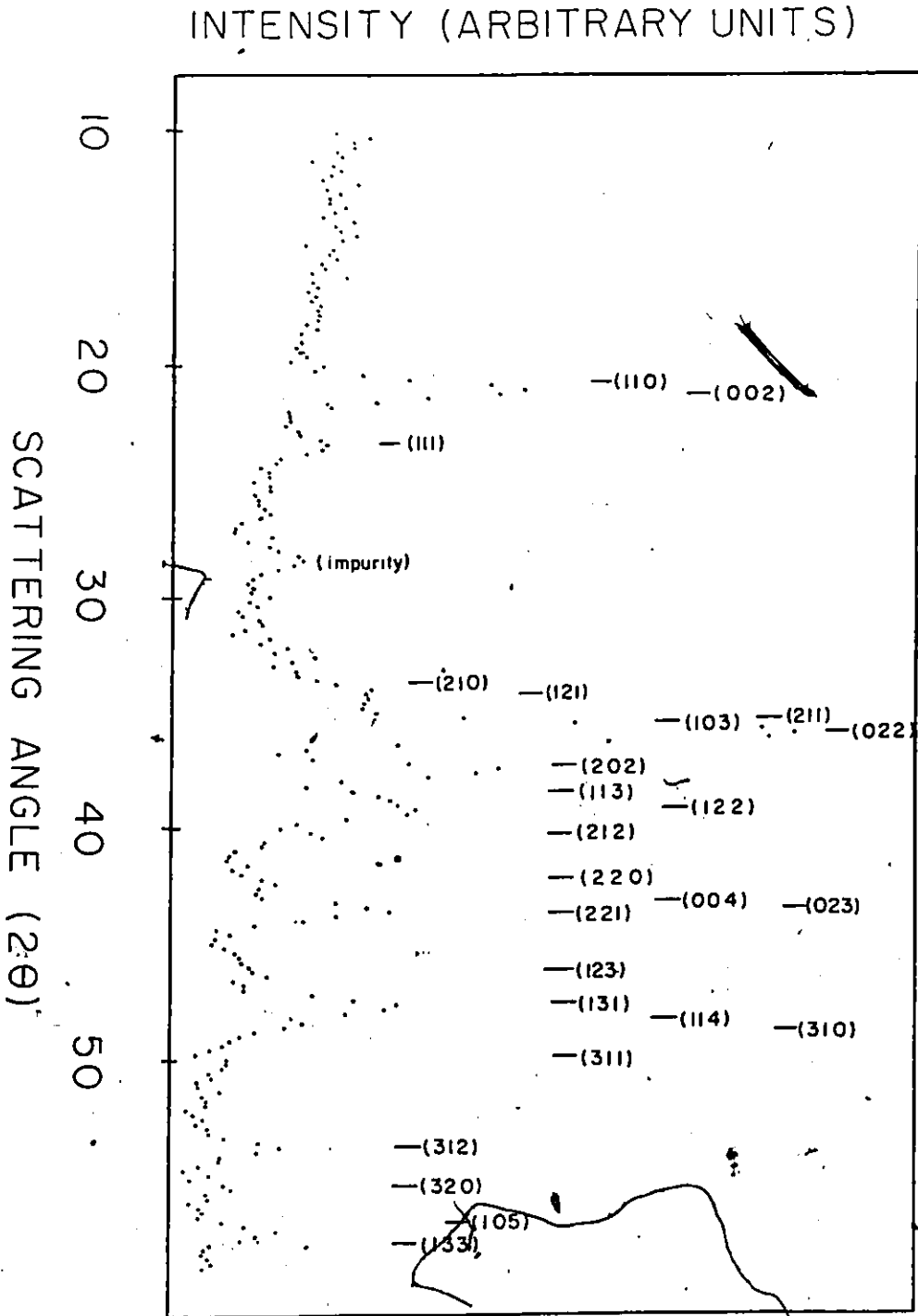
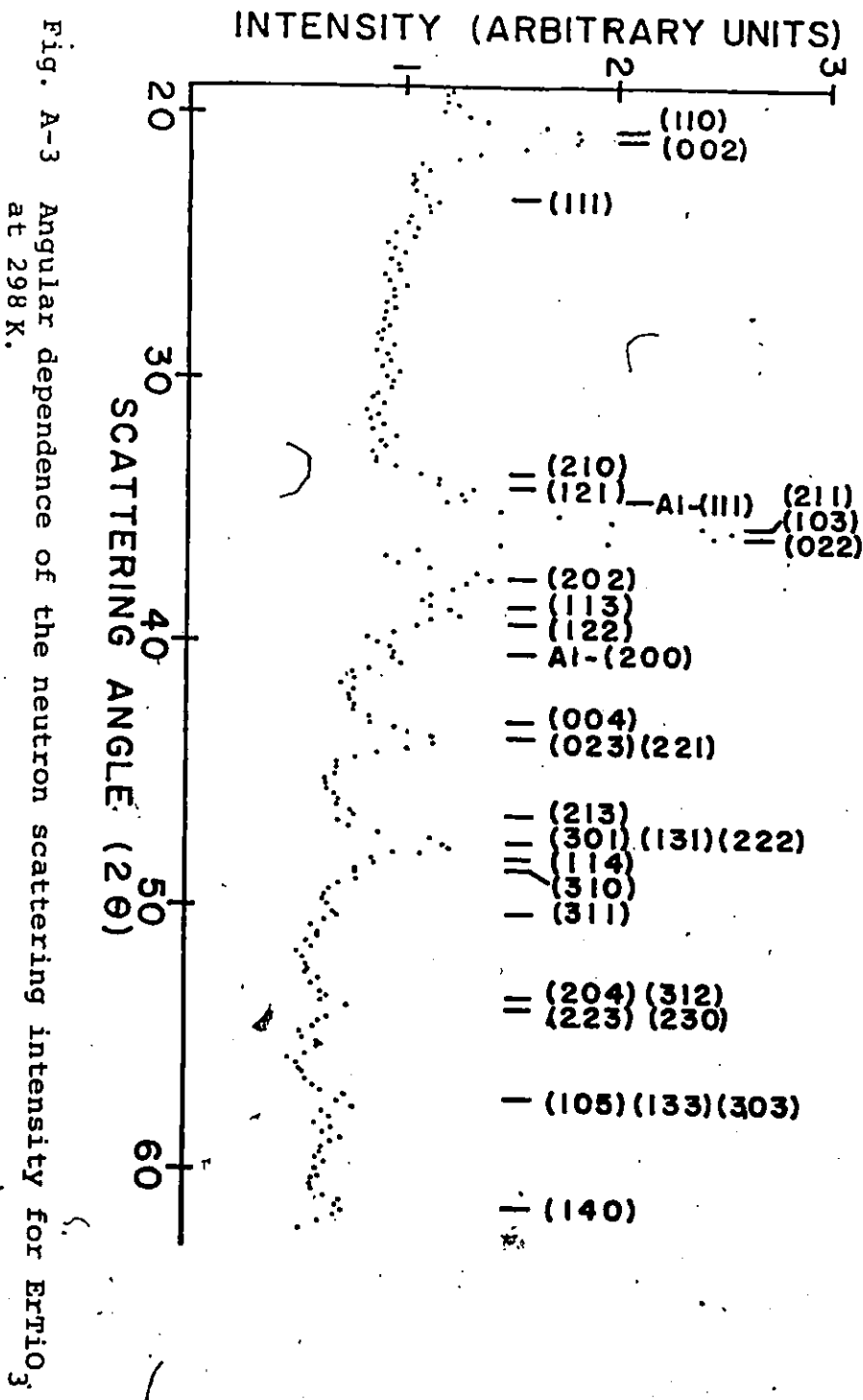


Fig. A-2 Angular dependence of the neutron scattering intensity for HoTiO_3 at 298 K.

Table A-2

Comparison of observed and calculated nuclear intensities for HoTiO_3 . $R'' = 8.1\%$

h k l	I_{obs}	I_{calc}
1 1 0	418±20	425
0 0 2		
1 1 1	87±12	75
2 0 2	412±20	398
1 1 3	428±20	325
1 2 2		
2 2 0	74±8	54
0 0 4	275±15	305
0 2 3		
2 2 1		
2 1 3		
3 0 1	435±42	429
1 3 1		
2 2 2		
1 1 4	97±24	145
3 1 0		
0 2 4		
2 0 4		
3 1 2	90±22	52
2 2 3		
2 3 0		
1 2 4		
2 3 1	90±22	52
3 2 0		



Comparison of observed and calculated nuclear intensities for ErTiO_3 . $R'' = 5.3\%$

h k l	I_{obs}	I_{calc}
1 1 0	305±21	253
0 0 2		
1 1 1	35±15	47
2 0 2	222±17	231
1 1 3	207±16	214
1 2 2		
0 0 4	173±20	187
0 2 3		
2 2 1		
2 1 3	286±26	266
3 0 1		
1 3 1		
2 2 2		
1 1 4	42±11	31
3 1 0		
3 1 1		
2 0 4	76±10	82
3 1 2		
2 2 3	84±10	89
2 3 0		
1 0 5	72±8	76
1 3 3		
3 0 3		
1 4 0		

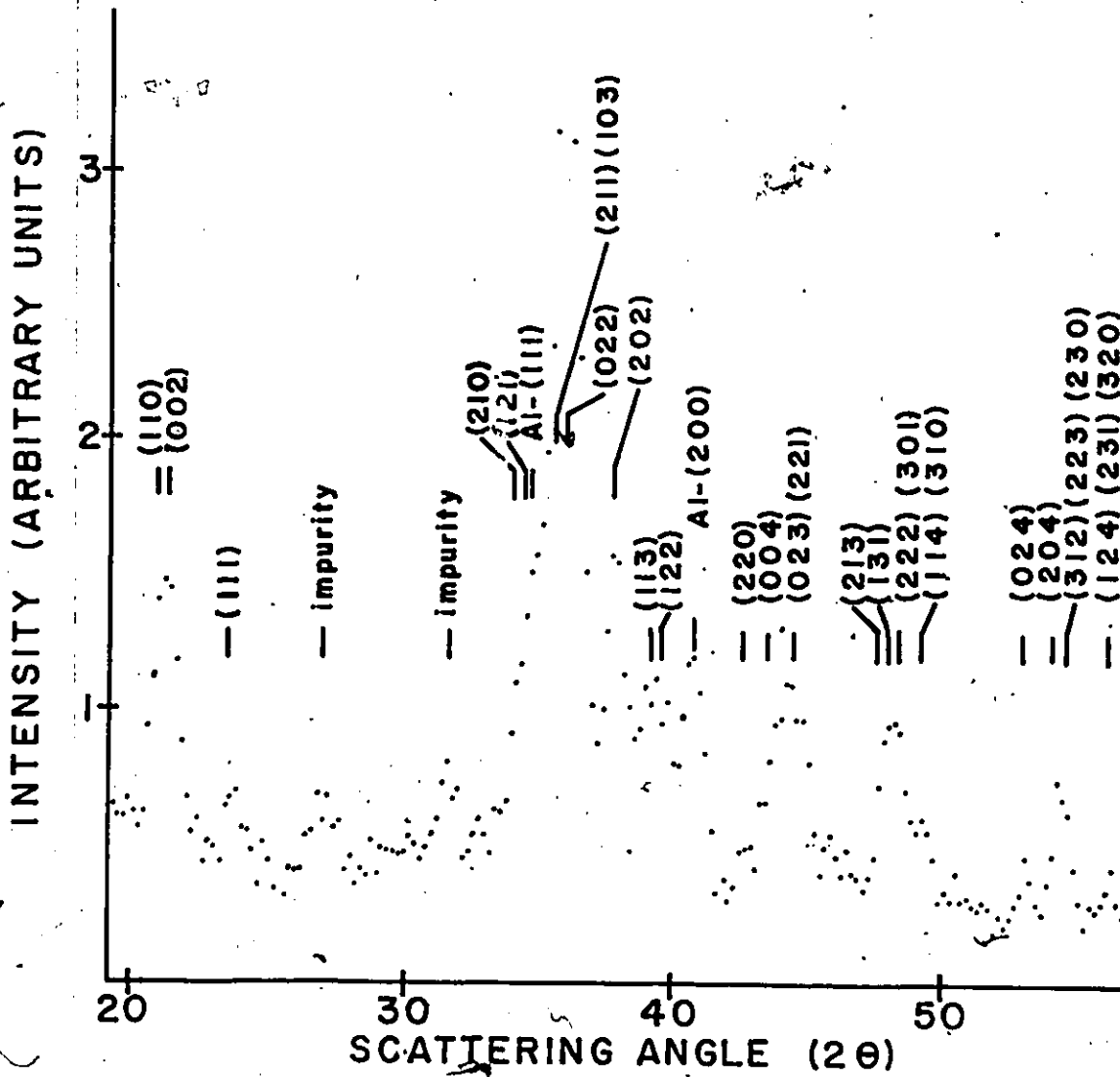


Fig. A-4 Angular dependence of the neutron scattering intensity for TmTiO_3 at 100 K.

Comparison of observed and calculated nuclear intensities of TmTiO_3 . $R'' = 4.9\%$

h k l	I_{obs}	I_{calc}
1 1 0	493±25	525
0 0 2		
2 0 2	546±20	466
1 1 3	460±20	510
1 2 2		
2 1 3	370±30	366
3 0 1		
1 3 1		
2 2 2	120±20	187
1 1 4		
3 1 0		
2 0 4		
3 1 2	212±22	181
2 2 3		
2 3 0		
1 2 4	57±15	76
2 3 1		
3 2 0		

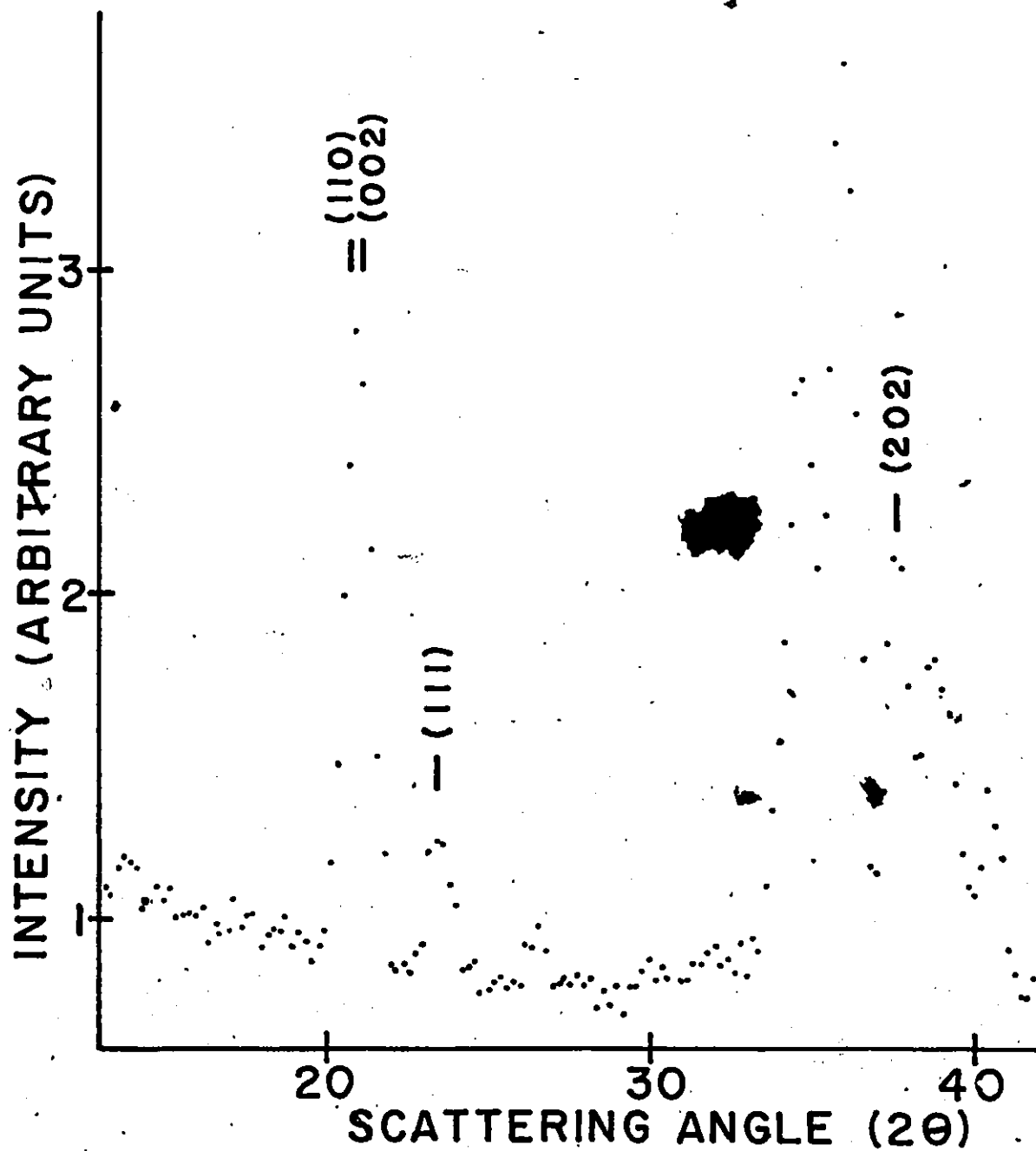


Fig. A-5 Angular dependence of the neutron scattering intensity for YbTiO_3 at 100 K.

INTENSITY (ARBITRARY UNITS)

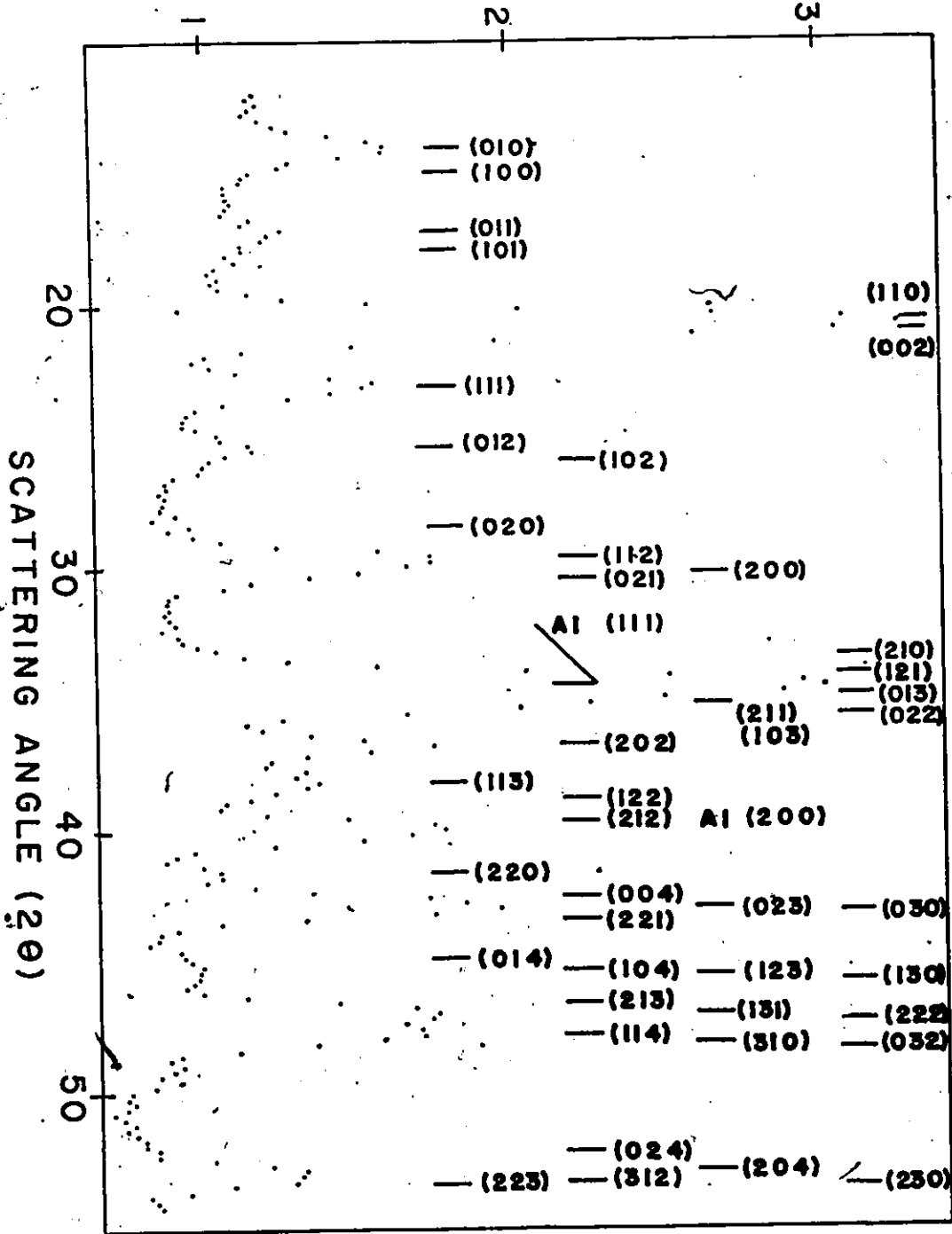


Fig. B-1 Angular dependence of the neutron scattering intensity for $DyF_{10}3$ at 10 K.

Table B-1

Comparison of observed and calculated magnetic intensities for DyTiO_3 . $R^2 = 7.7\%$

h k l	I_{obs}	I_{calc}
0 1 0	544±42	424
0 1 1	161±31	161
1 0 1		
1 1 0	1558±64	1604
0 0 2		
1 1 1	331±43	357
0 1 2	305±34	416
1 0 2		
0 2 0	15±15	23
1 1 2	889±54	892
2 0 0		
0 2 1	312±90	302
2 1 0		
1 2 1	103±46	167
0 1 3		
2 1 1	56±18	49
1 0 3		
0 2 2	15±15	36
1 1 3		
1 2 2		
2 1 2		
2 2 0		

(continued next page)

Table B-1 (continued)

h k l	I_{obs}	I_{calc}
0 0 4		
0 2 3		
0 3 0	422±72	337
2 2 1		
0 1 4		
1 0 4		
1 2 3	162±34	189
1 3 0		
2 1 3		
1 3 1		
3 0 1		
2 2 2	834±72	646
1 1 4		
3 1 0		
0 3 2		
0 2 4		
2 0 4		
3 1 2	280±72	382
2 2 3		
2 3 0		

INTENSITY (ARBITRARY UNITS)

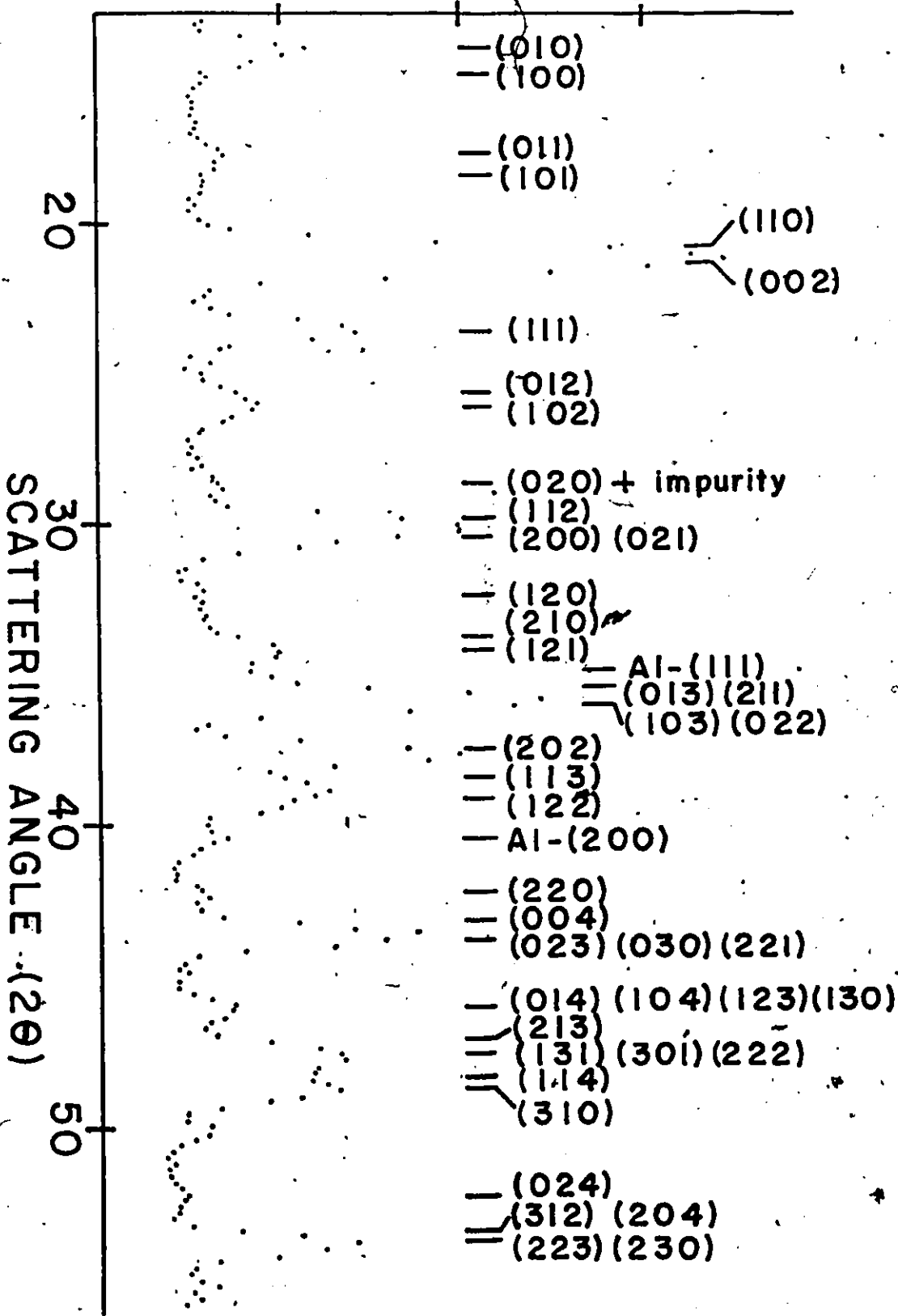


Fig. B-2 Angular dependence of the neutron scattering intensity for HoTiO_3 at 4.2 K.

Table B-2

Comparison of observed and calculated magnetic intensities of HoTiO_3 . $R^2 = 4.3\%$

h k l	I_{obs}	I_{calc}
0 1 0	309±20	272
0 1 1	82±15	91
1 0 1	22±15	41
1 1 0 } 0 0 2 }	1576±50	1584
1 1 1	373±19	362
0 1 2 } 1 0 2 }	251±15	263
0 2 0	15±15	7
1 1 2 } 2 0 0 } 0 2 1 }	971±25	995
1 2 0	20±20	17
2 1 0	20±20	2
1 2 1	66±17	117
2 1 1 } 1 0 3 } 0 2 2 } 0 1 3 }	84±50	206
2 0 2	352±22	377

(continued next page)

Table B-2 (continued)

h k l	I_{obs}	I_{calc}
1 1 3)		
1 2 2)	185±30	151
2 2 0	50±25	25
0 0 4)		
0 2 3	456±30	419
2 2 1		
0 3 0)		
0 1 4)		
1 0 4	110±20	118
-1 3 0		
1 2 3)		
2 1 3)		
3 0 1		
1 3 1		
2 2 2)	693±17	571
1 1 4		
3 1 0		
0 3 2)		
2 0 4)		
2 2 3		
3 1 2)	431±30	370
2 3 0		
0 2 4)		

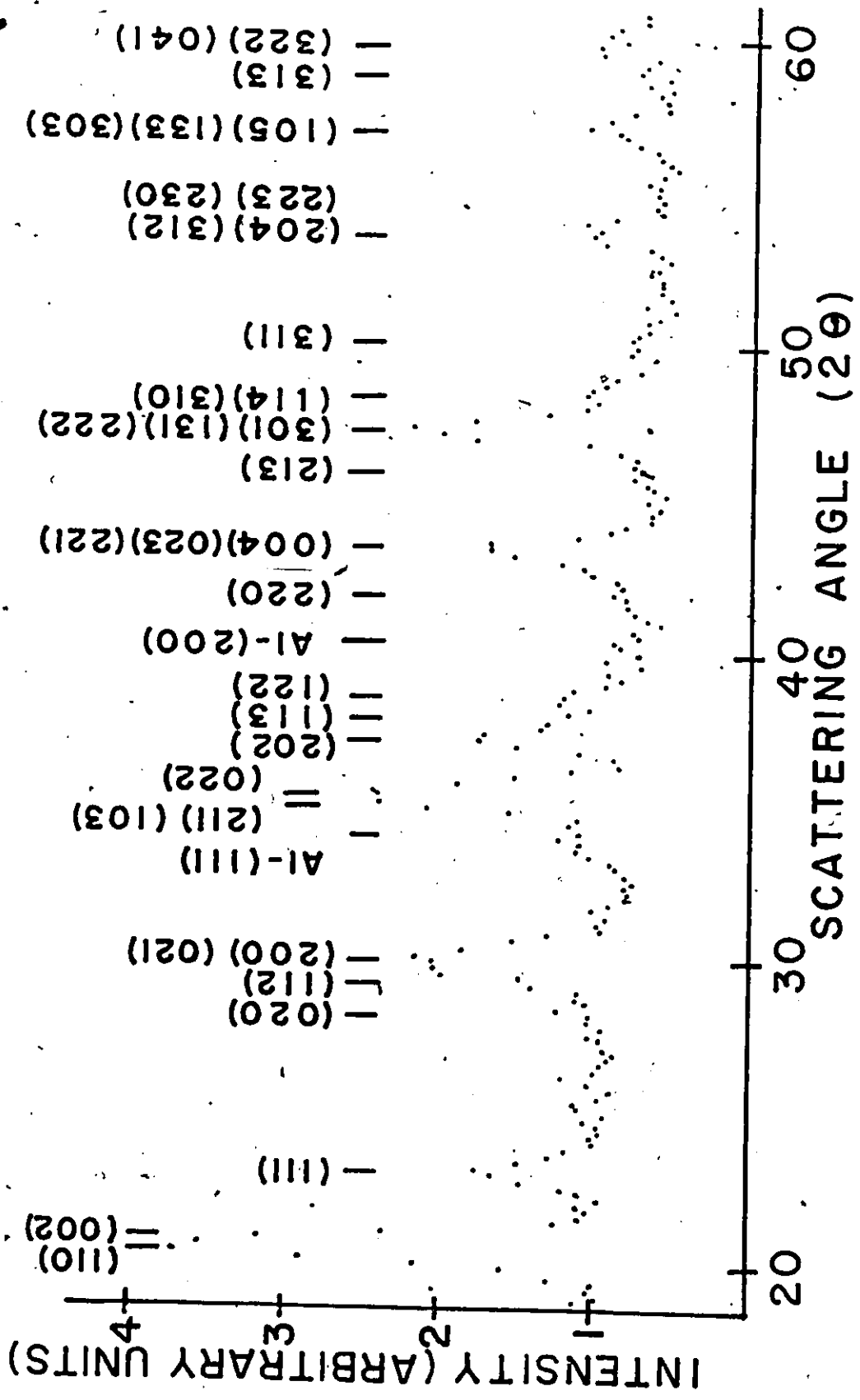


Fig. B-3 Angular dependence of the neutron scattering intensity for ErTiO_3 at 4.2 K.

Table B-3

Comparison of observed and calculated magnetic intensities of ErTiO_3 . $R'' = 4.1\%$

h k l	I_{obs}	I_{calc}
1 1 0	1124±50	1128
0 0 2	0±100	0
1 1 1	245±50	329
0 2 0	121±59	71
1 1 2	847±70	855
2 0 0		
0 2 1		
2 1 1	191±70	130
1 0 3		
0 2 2		
2 0 2	227±47	213
2 2 0	71±24	51
0 0 4	353±38	303
0 2 3		
2 2 1		
2 1 3	441±28	416
3 0 1		
1 3 1		
2 2 2	131±23	153
1 1 4		
3 1 0	42±19	47
3 1 1		

(continued next page)

Table B-3 (continued)

h k l	I _{obs}	I _{calc}
2 0 4	183±28	234
3 1 2		
2 2 3		
2 3 0		
3 1 3	137±47	101
3 2 2		
0 4 1		
1 0 5	99±25	129
1 3 3		
3 0 3		

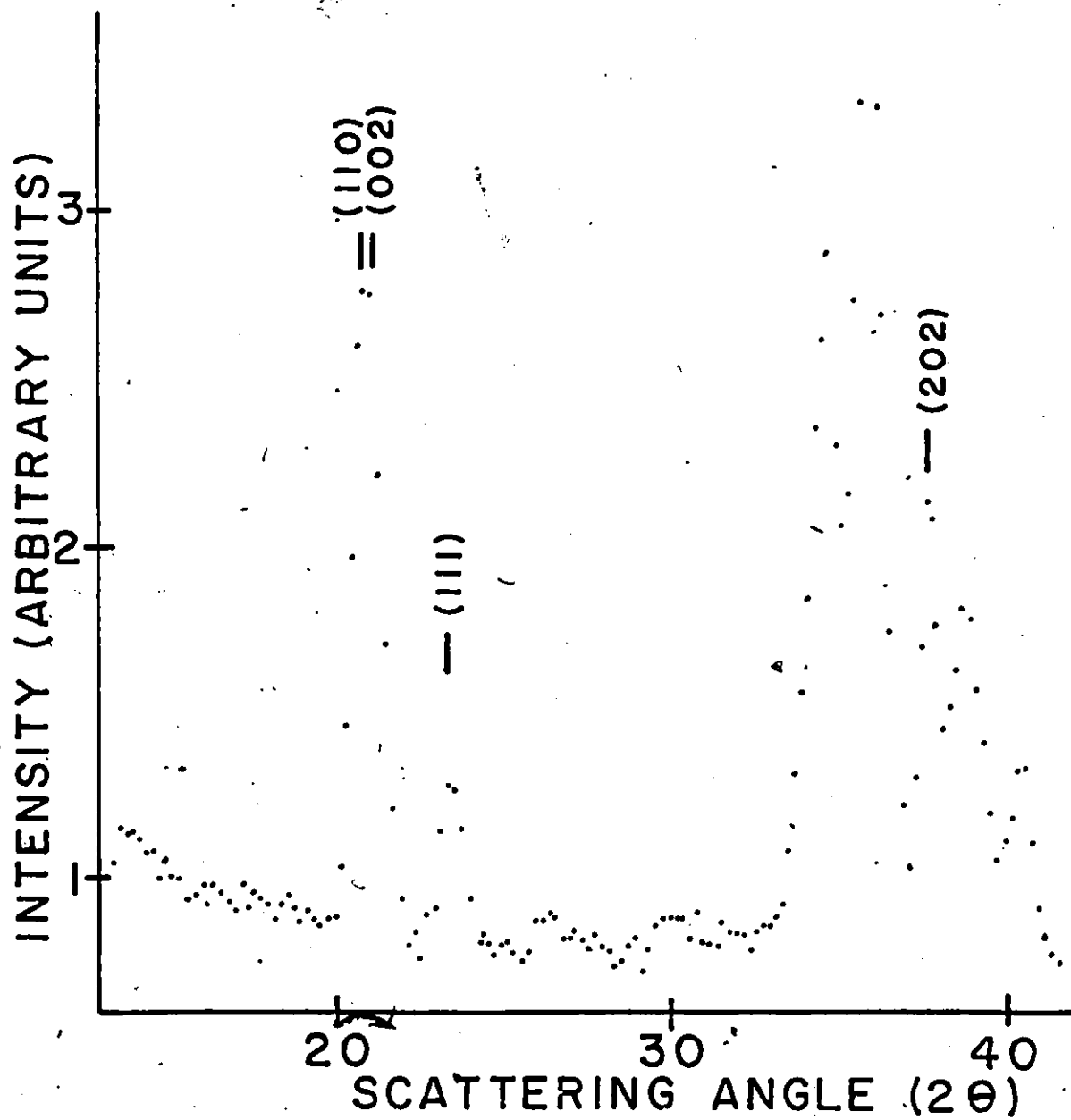


Fig. B-4 Angular dependence of the neutron scattering intensity for YbTiO_3 at 10 K.

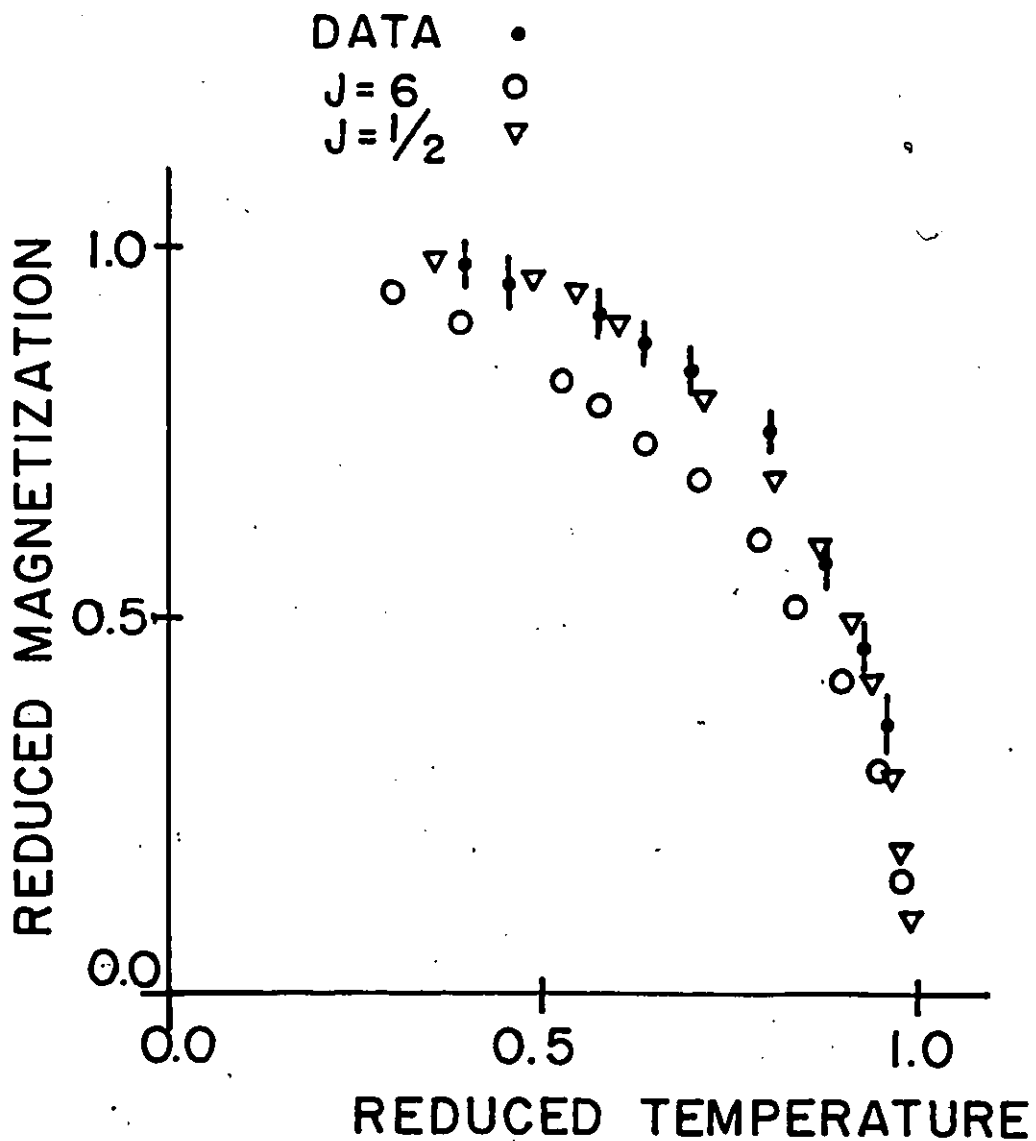


Fig. C-1 Reduced magnetization versus reduced temperature for the (110) ferrimagnetic reflection of TmTiO_3 .

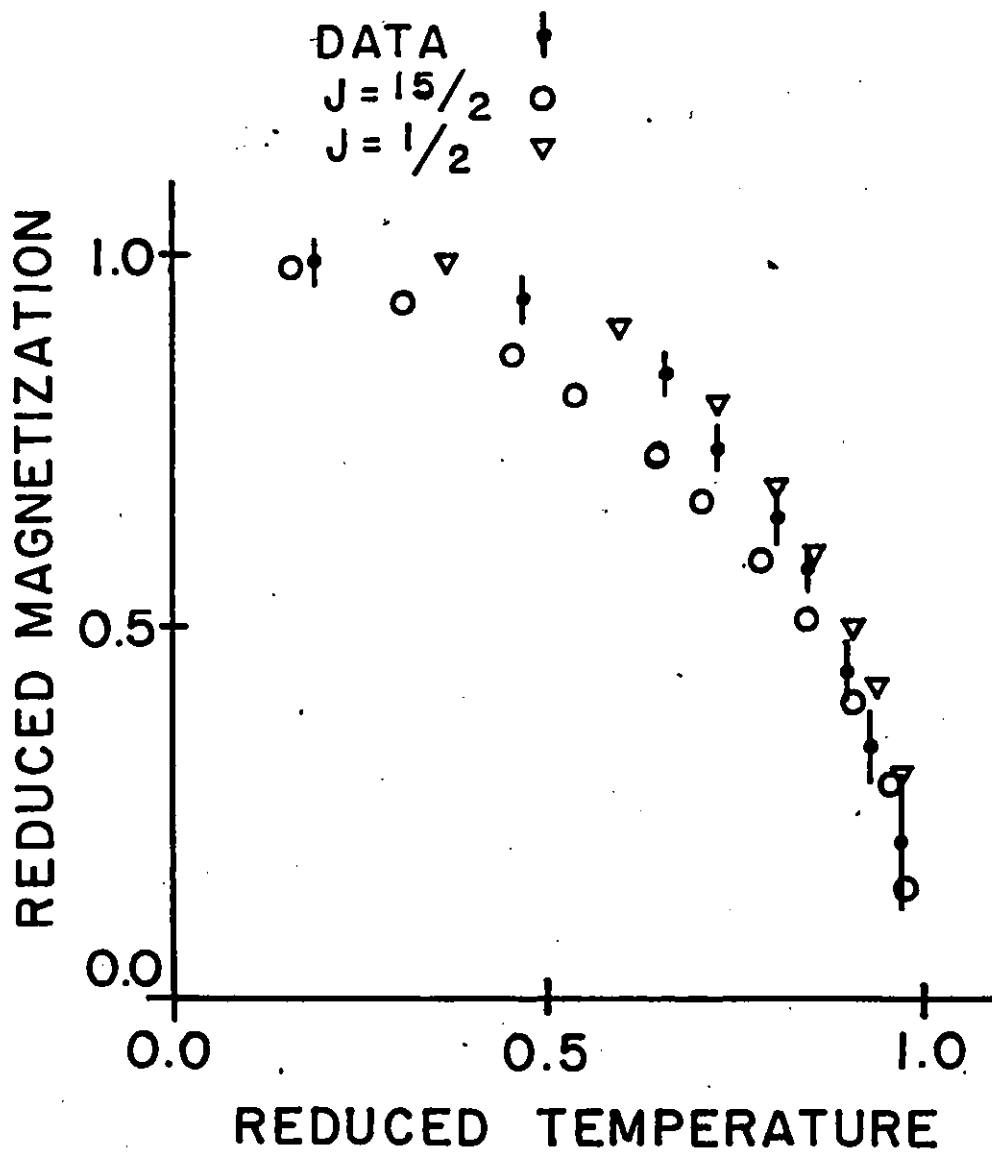


Fig. C-2 a) Reduced magnetization versus reduced temperature for the (112), (200), (021) ferrimagnetic reflection of DyTiO_3 .

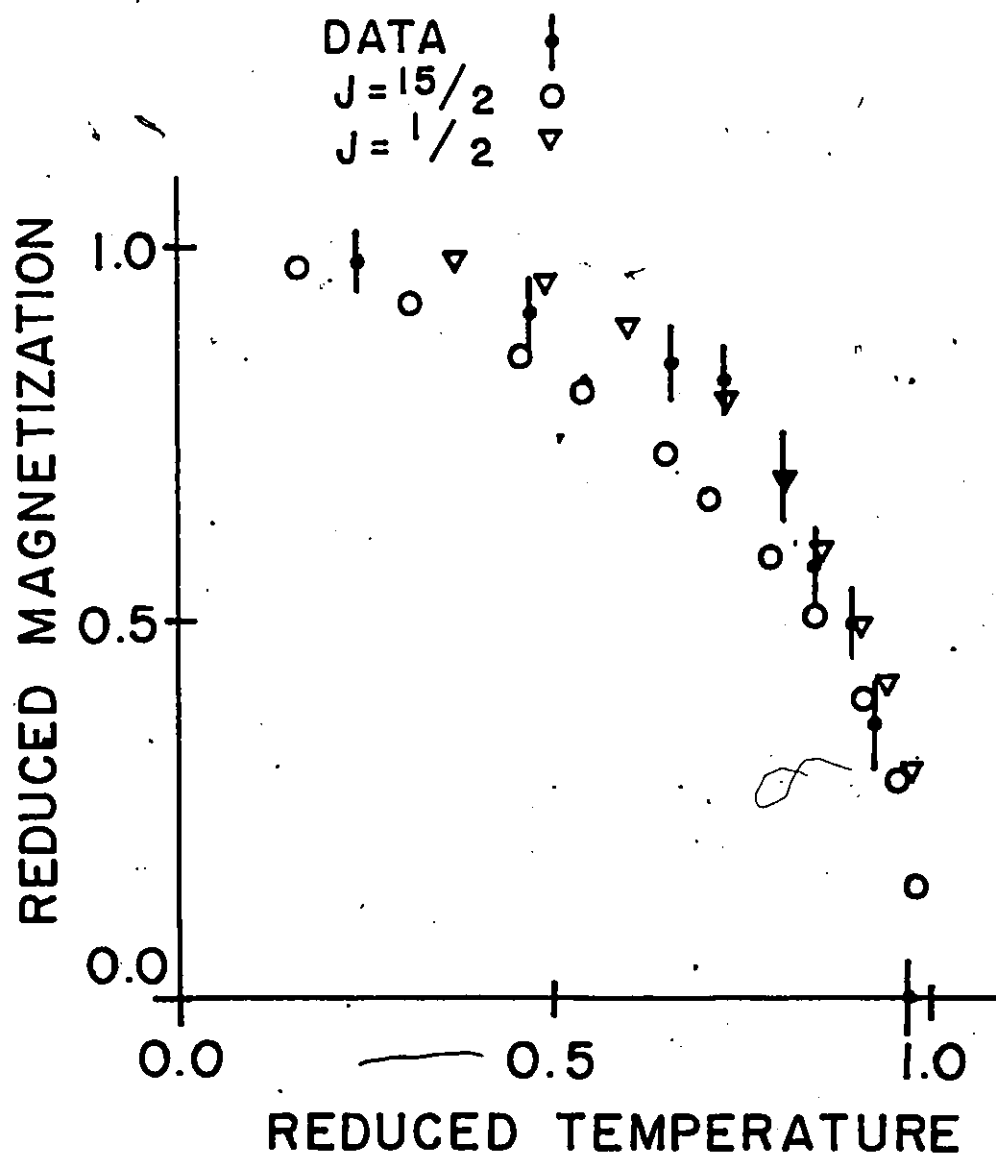


Fig. C-2 b) Reduced magnetization versus reduced temperature for the (012), (102) anti-ferromagnetic reflection of DyTiO_3 .

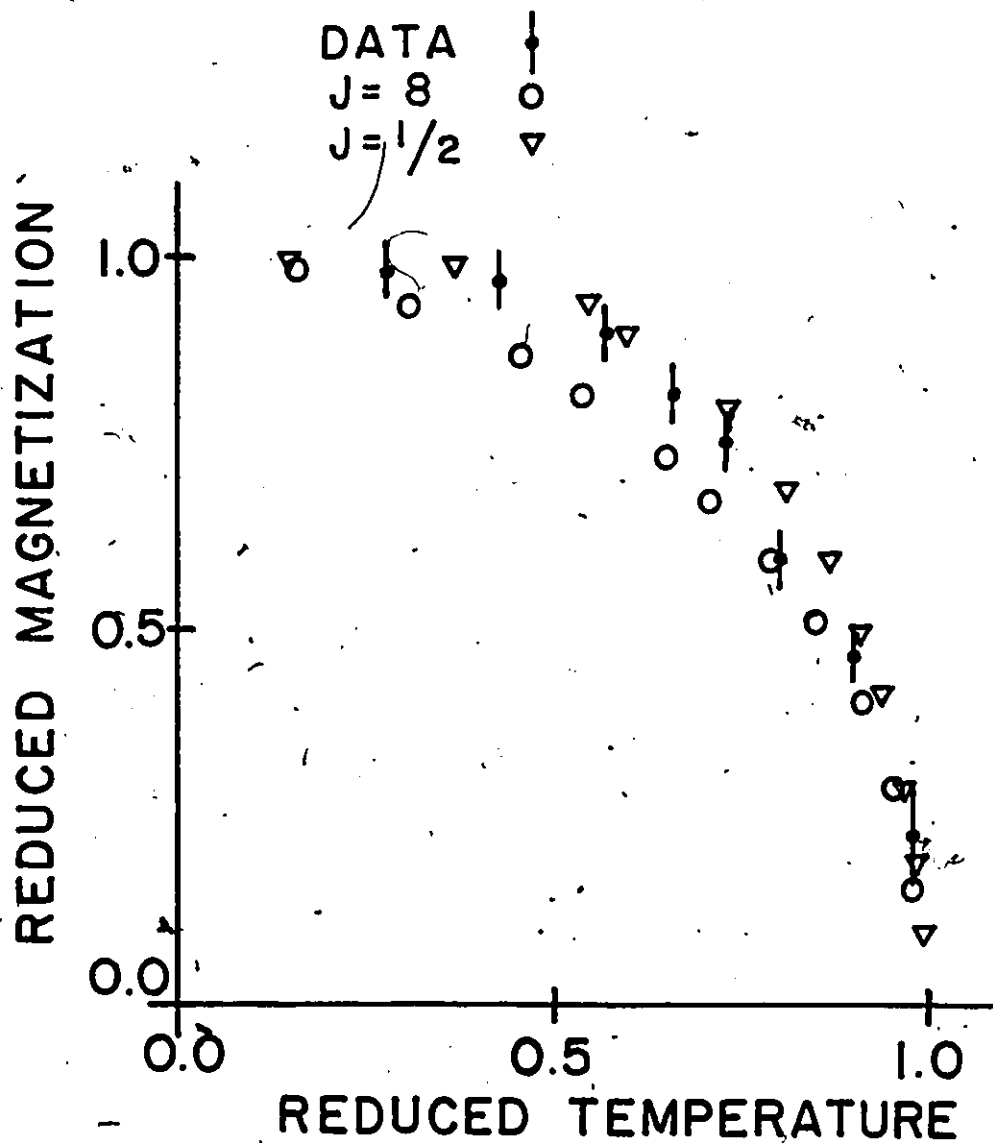


Fig. 3-ca Reduced magnetization versus reduced temperature for the (110), (002) ferrimagnetic reflection for HoTiO_3 .

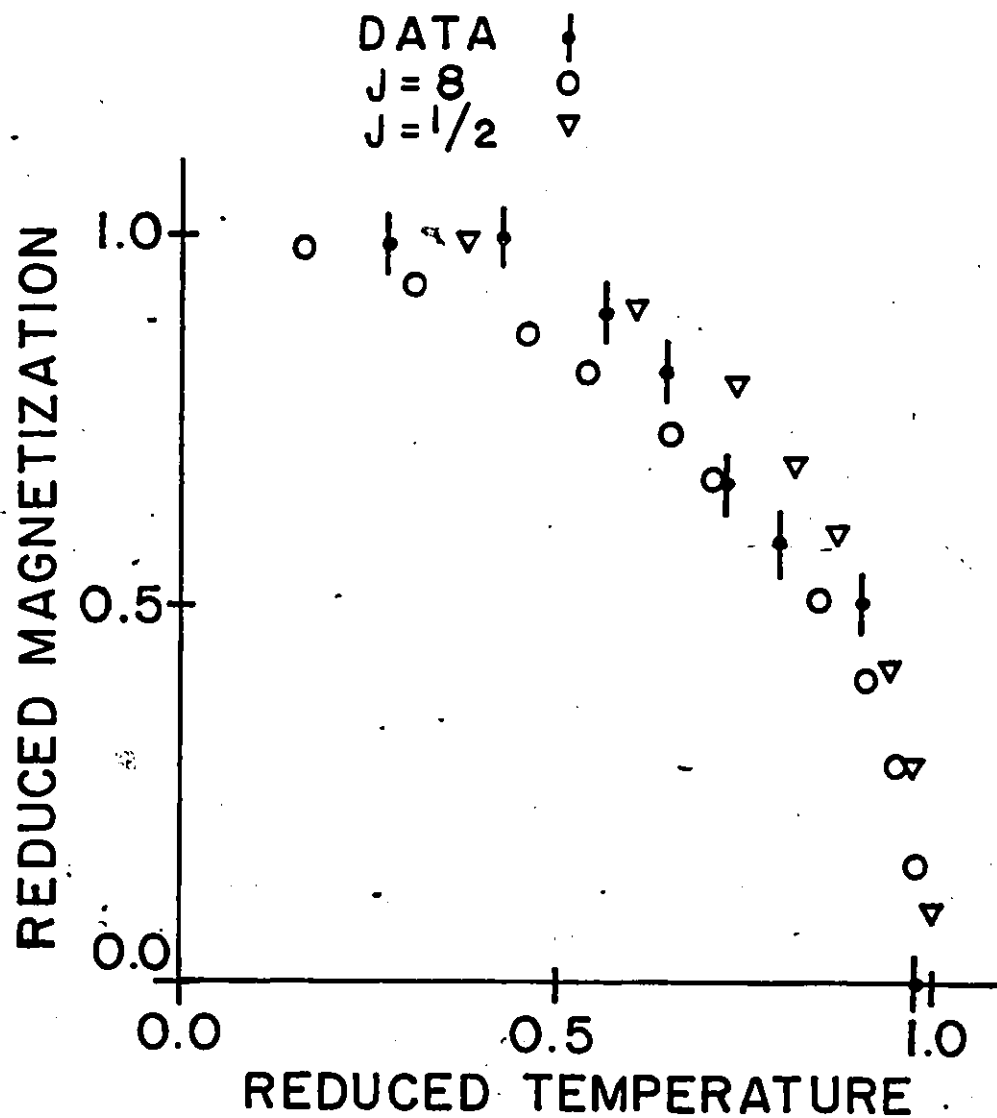


Fig. C-3 b) Reduced magnetization versus reduced temperature for the (010) antiferromagnetic reflection of HoTiO_3 .

Table D-1
Magnetization-temperature data for $R\text{TiO}_3$, Rb = Tb-Lu

TbTiO_3		DyTiO_3		HoTiO_3		ErTiO_3		TmTiO_3		YbTiO_3		LuTiO_3	
T(K)	σ_g^*	T(K)	σ_g^*	T(K)	σ_g^*	T(K)	σ_g^*	T(K)	σ_g^*	T(K)	σ_g^*	T(K)	σ_g^*
50	.2680	65	.2120	57	.1814	41	.2129	58	.1490	40	.2739	30	.2270
49	.3564	64	.2818	56	.2508	40	.5459	57	.2600	39	.3647	29	.3999
48	.4764	63	.3823	55	.4062	39	1.062	56	.3985	38	.4712	28	.5444
47	.6173	62	.4784	54	.6237	38	1.227	55	.5166	37	.5805	27	.6722
46	-	61	.5627	53	.8006	37	1.354	54	.6056	36	.6957	26	.7726
45	.7981	60	.6313	52	.8758	36	1.479	53	.6729	35	.8112	25	.8800
44	.9182	59	.6878	51	.9471	35	1.611	52	.7285	34	.9165	24	.9820
43	.9788	58	.7338	50	1.000	34	1.710	51	.7823	33	1.018	23	1.056
42	1.020	57	.7637	49	1.073	33	1.810	50	.8309	32	1.110	22	1.147
41	1.057	56	.7918	48	1.125	32	1.951	-	-	31	1.181	21	1.202

* σ_g (emu/g)

Table D-2

Inverse susceptibility (mole/cm³)-temperature (K)
data for RTiO₃, R = Tb-Tm

Temp.	TbTiO ₃		DyTiO ₃		HoTiO ₃		ErTiO ₃		TmTiO ₃	
	X _{calc} ⁻¹	X _{obs} ⁻¹	X _{calc} ⁻¹	X _{obs} ⁻¹	X _{calc} ⁻¹	X _{obs} ⁻¹	X _{calc} ⁻¹	X _{obs} ⁻¹	X _{calc} ⁻¹	X _{obs} ⁻¹
270	27.76	27.81	21.18	21.19	20.43	20.49				
265	27.24	27.74	20.76	20.83	20.06	20.18				
260	26.72	26.83	20.33	20.45	19.68	19.80				
255	26.20	26.30	19.91	20.13	19.30	19.42	43.13	42.87		
250	25.68	25.59	19.49	19.57	18.93	19.12	42.31	42.10	44.17	44.51
245	25.05	25.04	19.06	19.09	18.55	18.73	41.49	41.49	43.34	43.58
240	24.63	24.76	18.64	18.92	18.17	18.37	40.67	40.77	42.51	42.78
235	24.11	24.55	18.21	18.52	17.80	17.97	39.85	39.90	41.67	41.97
230	23.59	23.50	17.79	18.22	17.42	17.56	39.03	39.09	40.84	41.19
225	22.96	23.33	17.36	17.68	17.04	17.18	38.21	38.30	40.00	40.38
220	22.54	22.77	16.94	17.12	16.67	16.76	37.39	37.52	39.17	39.62
215	21.91	22.50	16.51	16.84	16.29	16.40	36.57	37.07	38.33	38.84
210	21.39	21.53	16.09	16.29	15.91	16.02	35.74	36.30	37.49	37.87
205	20.97	21.16	15.66	15.84	15.53	15.69	34.92	35.10	36.66	37.03
200	20.45	20.85	15.23	15.47	15.15	15.28	34.10	34.23	35.82	36.23
195	19.93	20.32	14.80	14.96	14.77	14.93	33.28	33.46	34.98	35.38
190	19.40	20.03	14.37	14.65	14.39	14.57	32.46	32.65	34.14	34.37
185	18.87	19.38	13.95	14.24	14.01	14.30	31.64	31.86	33.30	33.57
180	18.35	18.58	13.52	13.85	13.63	13.92	30.81	31.05	32.45	32.83
175	17.82	18.27	13.08	13.46	13.25	13.54	29.99	30.21	31.61	31.94
170	17.29	17.69	12.65	13.08	12.87	13.15	29.17	29.37	30.76	31.13
165	16.76	17.04	12.22	12.54	12.48	12.76	28.34	28.50	29.91	30.28
160	16.23	16.48	11.79	12.18	12.10	12.38	27.52	27.59	29.06	29.67
155	15.70	15.95	11.35	11.71	11.71	12.01	26.69	26.72	28.21	28.80
150	15.16	15.50	10.91	11.27	11.33	11.59	25.87	25.99	27.35	28.03
145	14.62	14.92	10.47	10.77	10.94	11.19	25.04	25.08	26.49	27.23
140	14.09	14.51	10.03	10.30	10.55	10.79	24.22	24.24	25.63	26.39

(continued next page)

Table D-2 (continued)

Temp.	TbTiO ₃		DyTiO ₃		HoTiO ₃		ErTiO ₃		TmTiO ₃	
	X ⁻¹ _{calc}	X ⁻¹ _{obs}	X ⁻¹ _{calc}	X ⁻¹ _{obs}	X ⁻¹ _{calc}	X ⁻¹ _{obs}	X ⁻¹ _{calc}	X ⁻¹ _{obs}	X ⁻¹ _{calc}	X ⁻¹ _{obs}
135	13.55	13.85	9.59	9.89	10.16	10.39	23.39	23.44	24.76	25.58
130	13.00	13.25	9.14	9.48	9.76	10.00	22.56	22.59	23.88	24.73
125	12.45	12.69	8.69	8.94	9.37	9.51	21.73	21.65	23.00	23.87
120	11.90	12.00	8.23	8.38	8.97	9.09	20.90	20.81	22.11	23.11
115	11.34	11.50	7.78	7.87	8.56	8.66	20.07	20.00	21.20	22.14
110	10.78	10.93	7.31	7.38	8.15	8.23	19.23	19.19	20.28	21.17
105	10.21	10.24	6.83	6.84	7.74	7.79	18.40	18.37	19.34	20.13
100	9.62	9.63	6.34	6.28	7.31	7.32	17.55	17.42	18.36	18.99
95	9.02	8.90	5.84	5.74	6.87	6.83	16.71	16.65	17.35	17.64
90	8.40	8.23	5.31	5.04	6.42	6.32	15.86	15.79	16.28	16.16
85	7.76	7.46	4.75	4.40	5.94	5.75	15.00	14.93	15.11	14.54
80	7.07	6.74	4.14	3.77	5.42	5.15	14.14	14.13	13.77	12.79
75	6.32	5.94	3.45	3.11	4.83	4.52	13.26	13.25	12.12	10.61
70	5.46	5.12	2.62	2.39	4.13	3.69	12.36	12.36	9.69	7.91
65	4.39	4.25			3.17	2.79	11.42	11.44	4.51	5.23
60	2.85	3.38			1.44	1.71	10.44	10.43		
55							9.34	9.26		
50							8.00	7.80		
45							5.74	5.81		

Table D-3

Inverse susceptibility-temperature data
along the b and c axes of ErTiO_3

Temp. (K)	χ_c^{-1} (mole/cm ³)	χ_b^{-1} (mole/cm ³)	Temp. (K)	χ_c^{-1} (mole/cm ³)	χ_b^{-1} (mole/cm ³)
260	21.74	28.86	155	11.87	18.90
255	21.29	28.30	150	11.45	18.37
250	20.83	28.00	145	10.98	17.74
245	20.28	27.52	140	10.52	17.18
240	19.86	27.13	135	10.05	16.81
235	19.45	26.80	130	9.59	16.32
230	18.96	26.57	125	9.12	15.93
225	18.49	25.60	120	8.70	15.52
220	17.98	24.96	115	8.21	15.09
215	17.41	24.44	110	7.73	14.54
210	17.02	23.82	105	7.28	14.15
205	16.46	23.20	100	6.83	13.70
200	16.12	22.96	95	6.36	13.16
195	15.49	22.58	90	5.89	12.49
190	15.04	22.15	85	5.39	12.14
185	14.40	21.66	80	4.89	11.58
180	13.86	21.36	75	4.36	11.18
175	13.57	20.83	70	3.77	10.68
170	13.21	20.42	65	3.12	10.15
165	12.71	19.92	60		9.65
160	12.24	19.39	55		8.98

Table D-4

Inverse susceptibility-temperature data
along the crystallographic axes of HoTiO_3

Temp. (K)	χ_a^{-1} (mole/cm ³)	χ_b^{-1} (mole/cm ³)	χ_c^{-1} (mole/cm ³)	χ_{ave}^{-1} (mole/cm ³)
270	23.08	17.76	23.97	21.22
265	22.62	17.35	23.57	20.79
260	22.21	16.95	23.11	20.37
255	21.81	16.62	22.76	19.90
250	21.48	16.22	22.34	19.61
245	21.19	15.92	21.95	19.28
240	21.21	15.51	21.56	18.99
235	21.01	15.09	21.21	18.63
230	20.66	14.58	20.81	18.18
225	20.29	14.21	20.44	17.80
220	19.81	13.81	20.15	17.39
215	19.43	13.31	19.73	16.92
210	19.06	12.99	19.36	16.57
205	18.60	12.61	18.99	16.15
200	18.26	12.21	18.62	15.76
195	17.85	11.82	18.23	15.35
190	17.52	11.41	17.83	14.94
185	17.14	11.00	17.46	14.53
180	16.80	10.61	17.11	14.14
175	16.46	10.24	16.74	13.75
170	16.02	9.80	16.34	13.29
165	15.69	9.40	15.96	12.89
160	15.26	9.00	15.57	12.45
155	14.90	8.61	15.17	12.04
150	14.51	8.19	14.85	11.81
145	14.17	7.78	14.41	11.17
140	13.81	7.39	14.04	10.75
135	13.42	7.00	13.56	10.31
130	13.02	6.58	13.14	9.84

(continued next page)

Table D-4 (continued)

Temp.	X_a^{-1} (mole/cm ³)	X_b^{-1} (mole/cm ³)	X_c^{-1} (mole/cm ³)	X^{-1} (mole/cm ³)
125	12.69	6.19	12.77	9.41
120	12.31	5.77	12.40	8.95
115	11.98	5.34	12.00	8.47
110	11.60	4.92	11.65	7.99
105	11.27	4.48	11.21	7.48
100	10.91	4.06	10.81	6.97
95	10.55	3.63	10.35	6.43
90	10.17	3.18	9.85	5.83
85	9.80	2.70	9.43	5.19
80	9.35	2.32	9.00	4.62
75	8.89	1.76	8.58	3.76
70	8.41	1.39	8.14	3.12
65	7.83	.88	7.63	2.15